MANIPULATING LIGHT WITH RING RESONATORS COUPLED TO ANTENNAS AND MECHANICAL MOTION

Freek Ruesink

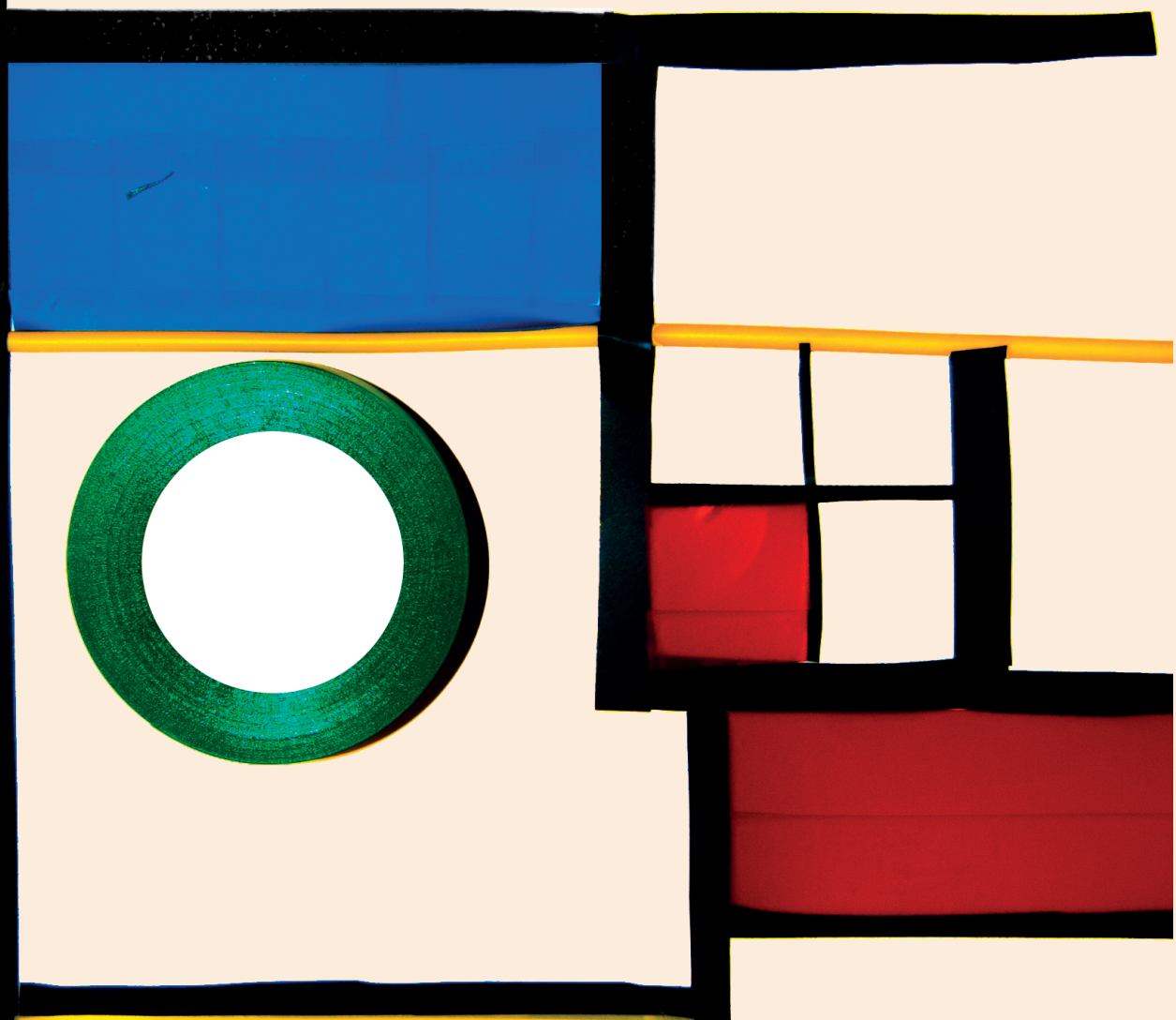

Manipulating light with ring resonators coupled to antennas and mechanical motion

Cover image: '*Optical fibre and sticky tape*', made by Freek Ruesink.
Inspired by an optical fibre setup and the work of Piet Mondriaan.

Ph.D. Thesis, Technical University Eindhoven, November 2017
Manipulating light with ring resonators coupled to antennas and mechanical motion
Freek Ruesink

ISBN: 978-94-92323-15-6

The work described in this thesis was performed at
AMOLF, Science Park 104, 1098 XG Amsterdam, The Netherlands.

This work is part of the Netherlands Organisation for Scientific Research (NWO).
It is also funded by the Office of Naval Research, grant No. N00014-16-1-246.

A digital version of this thesis can be downloaded from http://www.amolf.nl

Manipulating light with ring resonators coupled to antennas and mechanical motion

PROEFSCHRIFT

ter verkrijging van de graad van doctor aan de Technische Universiteit Eindhoven, op gezag van de rector magnificus prof.dr.ir. F.P.T. Baaijens, voor een commissie aangewezen door het College voor Promoties, in het openbaar te verdedigen op donderdag 23 november 2017 om 16:00 uur

door

Freek Ruesink

geboren te Amsterdam

Dit proefschrift is goedgekeurd door de promotoren en de samenstelling van de promotiecommissie is als volgt:

Voorzitter:	prof. dr. ir. H. J. M. Swagten	
1e promotor:	prof. dr. E. Verhagen	
2e promotor:	prof. dr. A. F. Koenderink	(Universiteit van Amsterdam)
leden:	prof. dr. L. Novotny	(ETH Zürich)
	prof. dr. A. P. Mosk	(Universiteit Utrecht)
	prof. dr. A. Fiore	
	dr. R. W. van der Heijden	
	dr. J. J. G. M. van der Tol	

Het onderzoek of ontwerp dat in dit proefschrift wordt beschreven is uitgevoerd in overeenstemming met de TU/e Gedragscode Wetenschapsbeoefening.

Contents

II Nonreciprocity in Optomechanics

Epilogue

Chapter 1

Introduction

Light and its interactions with matter are responsible for the colours we perceive and determine the functioning and well-being of our ecosystem. It is thus unsurprising that light serves, and has served, as a favourite topic of study and wonder for many. In addition to an increased knowledge of the impact and importance of light on biological systems (*e.g.* humans), the resulting fundamental understanding of light has enabled a plethora of light-based technologies that are omnipresent in today's society. A prominent example includes the transport of data via fibre-based optical communication networks [1, 2] that span almost the entire globe. Due to the high bandwidth at the employed *optical* frequencies, such optical fibre networks are pivotal for the existence of high-speed internet connections. Additionally, the fast-developing field of photovoltaics [3] concerns the conversion between sunlight and electrons and – together with other renewable energy sources – is expected to make a significant contribution to a fossil-fuel-free world.

On top of these more established technologies, numerous exciting fields that exploit the control over light given by structured matter have emerged in recent years. A major example is the field of 'silicon photonics' [4, 5], which studies the on-chip routing and manipulation of light employing materials and patterning techniques from the semiconductor industry. Combining the resulting optical components with standard electronic equipment on a single chip holds the promise of complementing ordinary electronic systems in the quest to further miniaturize computer components. Furthermore, and related to this, light is regarded as the prime candidate for the transport of sensitive (quantum) information stored in solid-state nodes and devices [6–8]. However, the successful implementation of these light-based technologies requires understanding on how to 1) actively control the emission rate of (single) photons by emitters, 2) route the flow of photons, and 3) protect the information encoded in photons against external (quantum) noise sources. Importantly, the wavelength at optical frequencies, together with a desire for small-footprint devices, sets the

natural length-scale for systems that can efficiently facilitate such functionality to nano- and microphotonic structures.

In this thesis, we explore resonant micro- and nanophotonic structures that have the potential to enhance light-matter interactions and control the flow of light. In particular, this work investigates the ability to tailor the optical response of a system using high quality-factor ring resonators. We do this by resonantly coupling the ring resonator's optical modes to either plasmonic nanoantennas, or to a *mechanical* mode of the structure itself. In both of these coupled systems, controlled interactions between resonant modes of different nature allows for an unusual optical response. As this thesis heavily relies on the understanding of resonantly coupled modes, this chapter starts with an introduction into the topic of (coupled) resonators, and their interactions with propagating fields. Afterwards, we discuss the optical properties of the high-Q whispering-gallery-mode resonators and plasmon antennas used in this work. Next, we introduce the field of cavity-optomechanics and subsequently finish with an outline of the work that is discussed later in this thesis.

1.1 Single resonators

A resonator is a system or structure that naturally oscillates at certain frequencies, called its resonant frequencies, with greater amplitude than at others. The most intuitive example of a (classical) resonator is provided by a simple mass m, connected to a rigid body by a spring characterized by spring constant k (see *e.g.* [9] for a more elaborate introduction). In the presence of a force F_0 driving the resonator, the amplitude (position) x of the mass is well described by the equation of motion

$$m\ddot{x}(t) + m\gamma\dot{x}(t) + kx(t) = F_0(t). \tag{1.1}$$

Here, we included velocity-dependent damping of the oscillatory motion by introducing the loss rate γ. Equation (1.1) is most easily solved in the Fourier domain*. After insertion of the natural frequency $\omega_0 = \sqrt{k/m}$, we obtain an expression for the amplitude $\tilde{x}$ that reads

$$\tilde{x}(\omega) = \tilde{F}_0(\omega)\chi(\omega) = \tilde{F}_0(\omega)\frac{1}{(\omega_0^2 - \omega^2) - \mathrm{i}\gamma\omega}, \tag{1.2}$$

where for simplicity $m = 1\,\mathrm{kg}$ is assumed. From this expression we identify the susceptibility $\chi(\omega) = [(\omega_0^2 - \omega^2) - \mathrm{i}\gamma\omega]^{-1}$ that describes the frequency-dependent response of the resonator towards an external force. Note that the loss term γ is contained in the imaginary part of χ, which is proportional to dissipation in the resonator and is closely related to fluctuations via the fluctuation-dissipation theorem [10, 11]. Controlling dissipation thus necessarily involves a

*Throughout this thesis we use the convention that the Fourier transform of $x(t)$ is given by $\tilde{x}(\omega) = \int x(t)\exp(\mathrm{i}\omega t)\,\mathrm{d}t$.

modification of Im[χ]. In section 1.3 we will discuss how an additional resonator can modify the damping rate.

To gain more insight in the concept of susceptibility, fig. 1.1 displays the absolute value of χ as a function of ω/ω_0 for varying quality factors Q. Here, $Q = \omega_0\tau$ where $\tau = \gamma^{-1}$ is the phonon (mechanical excitation) lifetime. From fig. 1.1a we observe that the susceptibility sharply peaks at the resonance frequency ω_0. The resonator is thus more prone so be set in motion at ω_0 than at any other frequency ω. Moreover, we observe that higher quality-factor resonators (which store their excitations for a longer time) exhibit more narrow resonances and higher peak susceptibilities. This difference is even better visualized when we plot the same result over a smaller frequency range, as is done in fig. 1.1b.

Equation (1.2) is quadratic in frequency, and for simplicity is often approximated to yield a linear relation for χ^{-1}. This approximation is known as the high-Q or Lorentzian approximation. To get the approximated formula, we write $(\omega_0^2 - \omega^2) = (\omega_0 - \omega)(\omega_0 + \omega)$, which yields $2\omega_0(\omega_0 - \omega)$ if $\omega_0 \approx \omega$. This approximation is strictly only valid close to ω_0, and for weakly damped resonators. The resulting approximated expression for χ reads

$$\chi \approx \chi_{\mathrm{L}} = \frac{1}{2\omega_0}\frac{\mathrm{i}}{(-\mathrm{i}\Delta_0 + \gamma/2)}, \tag{1.3}$$

with the detuning Δ_0 between Fourier frequency ω and resonance frequency ω_0 defined as $\Delta_0 \equiv \omega - \omega_0$. Figure 1.1b compares $|\chi_{\mathrm{L}}|$ as it is obtained from this approximated expression (dashed lines) with the lineshapes for $|\chi|$ resulting

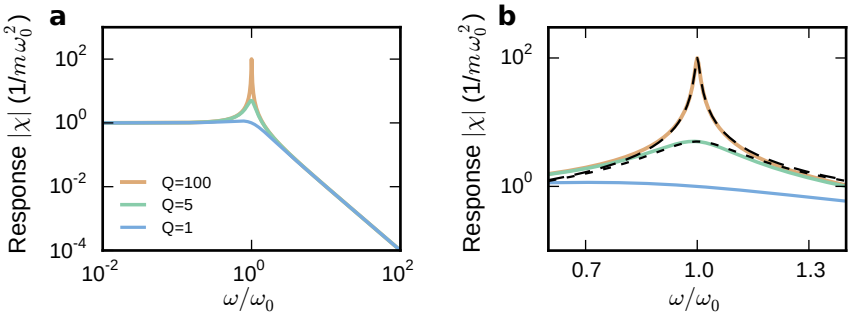

Figure 1.1: Frequency response of a harmonic oscillator. **a**, The susceptibility χ for a resonator exhibiting different quality factors. For a weakly damped resonator ($Q = 100$, solid orange line), the response sharply peaks at ω_0. This in strong contrast for a resonator with low $Q = 1$ (solid blue line). **b**, Similar to **a**, but now plotted over a smaller frequency range. In addition, the dashed black lines show the response as it is obtained from the Lorentzian approximation. We plot this Lorentzian approximated response for resonators with quality factors of 5 and 100. Already for $Q = 5$, the approximated lineshape shows good agreement with the full-solution.

from eq. (1.2) for $Q = 100$ (solid orange line) and $Q = 5$ (solid green line). We can observe that already for a moderate quality factor of five, the Lorentzian lineshape serves as a good approximation, and we will use it for most resonators that we will encounter in later chapters, which exhibit quality factors that range from $Q \approx 5$ to $Q \approx 10^7$.

1.2 Interfacing resonators to the outside world

The driving and damping introduced in the previous section are only possible if the resonator can interact with its environment. A framework known as input-output theory [12–14] describes this interaction in a useful formalism, and treats resonators (mechanical, optical, or other) as being coupled to various channels that can carry away propagating waves, describing energy exchange with a connecting bath. Via these channels a resonator can dissipate energy, but also receives, as dictated by the fluctuation-dissipation theorem [10, 11], quantum and thermal noise. Moreover, input-output theory can incorporate the presence of an incoming coherent (probe) field driving the resonator. It treats such an incoming probe field as an input into one of its (decay) channels. In this section we present well-known results from input-output theory that are used to describe the response of a single (optical) resonator. Using the underlying equations we will introduce terminology that is used throughout this thesis. Moreover, it provides a basis for the discussion on optomechanical systems in section 1.5. We note that in section 1.3, we will formally introduce the (classical) input-output formalism for two coupled oscillators and multiple ports.

Here we employ the notation as it is frequently used in cavity quantum electrodynamics (CQED, see *e.g.* [12–14]) and quantum optomechanics (section 1.5). We use the Heisenberg equations of motion to describe the time evolution of the optical field amplitude $\hat{a}$ in a (high-Q) resonant optical cavity, where $\hat{a}$ is the photon annihilation operator[†]. For a resonator with resonance frequency ω_1 that is coupled to two input/output channels the equation of motion reads

$$\dot{\hat{a}} = (-\mathrm{i}\omega_1 - \kappa/2)\hat{a}(t) + \sqrt{\kappa_{\mathrm{ex}}}\hat{s}^+(t) + \sqrt{\kappa_0}\hat{f}^+(t), \tag{1.4}$$

such that the resonator couples to the two channels at rates κ_{ex} and κ_0. Accordingly, the resonator's total loss rate κ is defined as $\kappa \equiv \kappa_{\mathrm{ex}} + \kappa_0$. For reasons that we introduce shortly hereafter, we will refer to κ_0 as intrinsic losses and to κ_{ex} as exchange losses. Moreover, we point out that fluctuations driving the resonator via these dissipation channels are contained in $\hat{f}^+(t)$ and $\hat{s}^+(t)$.

For classical fields, $\hat{a}$ can be replaced by a complex field amplitude a, normalized such that $|a|^2$ is the number of photons (or energy) in the resonator,

[†]The operator $\hat{a}$ for a harmonic oscillator is related to the observable $\hat{x}$, as used in section 1.1, via $\hat{x} = (\hat{a} + \hat{a}^\dagger)x_{\mathrm{zpf}}$, where x_{zpf} is the zero-point motion of the oscillator.

which is found by calculating the expectation value $\langle \hat{a} \rangle$ [15]. Similarly, if $\hat{s}^+$ resembles an incident classical coherent field, we replace $\hat{s}^+$ by s^+ and note that $|s^+|^2$ represents the incoming photon flux (or power) that is incident on the cavity at rate κ_{ex}. Hence, we write the classical analogue of eq. (1.4) as

$$(\omega - \omega_1 + \mathrm{i}\kappa/2)a(\omega) = \mathrm{i}\sqrt{\kappa_{\mathrm{ex}}}s^+(\omega), \tag{1.5}$$

where we neglected the noise entering the system via the intrinsic channel (at rate κ_0), which has an expectation value (average) that is zero. From eq. (1.5) we find the field $a(\omega)$ in the resonator due to the presence of the drive field as

$$a(\omega) = \frac{\mathrm{i}\sqrt{\kappa_{\mathrm{ex}}}}{\omega - \omega_1 + \mathrm{i}\kappa/2}\, s^+(\omega). \tag{1.6}$$

As derived in for example refs. [12, 13, 16], the input fields s^+ and output fields s^- that enter and exit the resonator via the exchange channel (at rate κ_{ex}) are related via the input-output relation

$$s^-(\omega) = s^+(\omega) - \sqrt{\kappa_{\mathrm{ex}}}a. \tag{1.7}$$

Combining this relation with eq. (1.6) gives an expression for the outgoing field s^- that reads

$$s^-(\omega) = s^+(\omega) - \frac{\mathrm{i}\kappa_{\mathrm{ex}}s^+}{\omega - \omega_1 + \mathrm{i}\kappa/2}. \tag{1.8}$$

Hence, the output fields are the (coherent) sum of two possible light-paths: 1) direct reflection and 2) light that has entered and exited the cavity. Moreover, we observe that if the incoming field is resonant with the cavity ($\omega = \omega_1$), and the exchange losses equal the intrinsic losses ($\kappa_{\mathrm{ex}} = \kappa_0 = \kappa/2$), there are no outgoing fields, *i.e.* $s^- = 0$. This important condition is referred to as critical coupling, and shows that light can be fully dissipated in the intrinsic loss channel when external and intrinsic losses are matched. We can interpret this as if the directly returning fields and fields exiting from the cavity destructively interfere. In this specific situation, all light (*i.e.* energy) is thus necessarily lost through the intrinsic loss channel. Moreover, we identify the regimes of 'undercoupling' (when $\kappa_{\mathrm{ex}} < \kappa_0$) and 'overcoupling' (when $\kappa_{\mathrm{ex}} > \kappa_0$), which is terminology that will be frequently used in this thesis.

1.3 Coupling resonators

In this section we provide a formal derivation of input-output theory in the classical domain. We do this using coupled-mode theory [16–18], which is well-known in the optics and engineering literature. We treat a system containing two passive and linearly coupled resonators as this provides an important starting point for describing the physical systems in this thesis, but the theory

can be readily expanded to any number of modes. The equations of motion of two lossless (thus undriven) coupled modes with complex mode amplitudes a_1 and a_2 and resonance frequencies ω_1 and ω_2 can be written (in the high-Q limit) in the Fourier domain as

$$\begin{pmatrix} \omega - \omega_1 & g_+ \\ g_- & \omega - \omega_2 \end{pmatrix} \begin{pmatrix} a_1 \\ a_2 \end{pmatrix} = \begin{pmatrix} 0 \\ 0 \end{pmatrix}. \tag{1.9}$$

The hermiticity of the problem dictates that the coupling rates g_- and g_+ are related through $g_- = g_+^*$. This can be directly observed when deriving the equations of motion from the Hamiltonian in the Heisenberg picture. In principle, the phase of g_+ can be chosen arbitrarily: one can always change the gauge of this coupling phase by appropriately redefining a_2, for example.

However, this choice of phase does have consequences when considering how the resonators are coupled to input/output ports carrying propagating waves, through which they can be driven and into which they can decay (fig. 1.2). Introducing energy loss rates κ_i and input fields s_j^+ (collected in a vector $\mathbf{s}^+$ with length equal to the number of ports), we can write the equations of motion as

$$\begin{pmatrix} \omega - \omega_1 + \mathrm{i}\kappa_1/2 & g_+ \\ g_- & \omega - \omega_2 + \mathrm{i}\kappa_2/2 \end{pmatrix} \begin{pmatrix} a_1 \\ a_2 \end{pmatrix} = \mathrm{i}K\mathbf{s}^+, \tag{1.10}$$

where K is a matrix with coefficients that describe coupling of the input fields to the resonators. In principle, the phase of these input fields can be varied arbitrarily by moving the reference plane at which the propagating fields are observed along a particular port ('waveguide'), if the corresponding column of the K matrix is changed accordingly. Likewise, redefinition of the phase of g_+ by altering either a_1 or a_2 can be absorbed in a modified phase of a *row* of K.

A number of conventions and physical laws (energy conservation, reciprocity) place constraints on the elements of K, which take away the gauge freedom of the phases of the elements of $\mathbf{a}$ and $\mathbf{s}^+$. The first convention we take is $K = D^{\mathrm{T}}$ (fig. 1.2), where D contains the coefficients d_{ji} that relate the mode amplitudes a_i to the *output* fields s_j^- evaluated in the same reference planes as the input fields s_j^+ [17, 18]. This convention essentially means that each mode by itself is reciprocal, in the sense that the mode plus its output fields are equal to the time-reversed mode plus input fields. The output fields are found from

$$\mathbf{s}^- = C\mathbf{s}^+ + D\mathbf{a}, \tag{1.11}$$

where C is a unitary and symmetric scattering matrix that describes the direct coupling of input and output waves. Obviously, choosing particular phases in C for a given system fixes all reference planes in the input/output ports, restricting the phase gauge freedom of $\mathbf{s}^+$ and $\mathbf{s}^-$. The full scattering matrix S, relating $\mathbf{s}^+$ to $\mathbf{s}^-$ through $\mathbf{s}^- = S\mathbf{s}^+$ is now given by

$$S = C + \mathrm{i}D(M + \omega I)^{-1}D^{\mathrm{T}}, \tag{1.12}$$

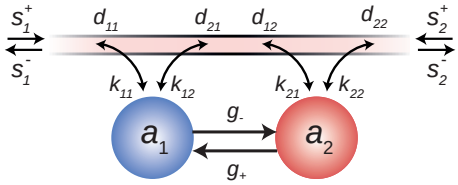

Figure 1.2: Two coupled resonators. The resonators a_1 and a_2 are coupled at coupling rates g_+ and g_- and connected to two input and output ports. The elements d_{ji} of matrix D relate the mode amplitudes a_i to the output fields s_j^-, whereas the elements k_{ij} relate the input waves s_j^+ to the mode amplitudes a_i. In the text we assume $K = D^{\mathrm{T}}$ ($k_{ij} = d_{ji}$) such that g_+ and g_- must be equal and real.

where

$$(M + \omega I) = \begin{pmatrix} \omega - \omega_1 + \mathrm{i}\kappa_1/2 & g_+ \\ g_- & \omega - \omega_2 + \mathrm{i}\kappa_2/2 \end{pmatrix} \tag{1.13}$$

and I the 2×2 identity matrix.

The question is whether in this context the phase of g_+ can be arbitrary, and can still be modified at will by proper adjustment of the D matrix. Since S needs to satisfy the principle of reciprocity, it must be a symmetric matrix. As C is symmetric, S is only symmetric if the matrix $B \equiv D(M + \omega I)^{-1} D^{\mathrm{T}}$ is symmetric. Since $B^{\mathrm{T}} = D((M + \omega I)^{-1})^{\mathrm{T}} D^{\mathrm{T}}$, and the inverse of a symmetric matrix is also symmetric, $B = B^{\mathrm{T}}$ only if $(M + \omega I) = (M + \omega I)^{\mathrm{T}}$. Together with the fact that $g_- = g_+^*$, this proves that with our convention of $K = D^{\mathrm{T}}$, the coupling rates g_+ and g_- *must be equal and real.*

Unusual responses can occur in systems where these coupling rates are either not equal or not real. To realize such non-trivial interactions, the aforementioned assumptions need to be violated. On the one hand, retardation, associated with radiative losses, can be introduced to yield a system with equal but complex coupling rates. The imaginary part of the coupling rate (the off-diagonal elements of matrix M) is then associated with interference of radiation of the two resonators in a common output port. For example, the relative phase with which the resonators radiate strongly affects the eigenmodes of the coupled system. Such a scenario is considered in chapter 2, where we investigate the (modified) eigenmode of a radiating high-Q ring resonator that is coupled to nanoantennas. On the other hand, breaking time-reversal symmetry in the coupling process can result in an asymmetric M matrix, and yield an asymmetric electromagnetic response of the coupled system. In part II of this thesis we use parametric optomechanical interactions to create such an asymmetry in M. This leads to a system that can exhibit nonreciprocal light transmission, which strongly relies on a direction dependent phase shift. Interestingly, this phase shift is reminiscent of the phase shift acquired by charged particles propgating around loops in the presence of a magnetic field,

known as the Aharonov-Bohm effect [19]. As photons have zero charge, a magnetic field does not provide such an asymmetry for light. It was first proposed by Yu & Fan [20] that coupled *optical* resonators can provide a similar nonreciprocal phase for photons, mimicking the non-trivial phase pickup experienced by electrons in the presence of a magnetic field.

The fact that the 'evolution matrix' M, which contains the dynamics of the eigenmodes, must be symmetric in the convention $K = D^{\mathrm{T}}$ is general for any reciprocal system of coupled modes. The principles of time-reversal symmetry and energy conservation also further constrain the elements of D. As shown by the group of Shanhui Fan [17, 18], one can derive the relationships

$$D^{\dagger}D = \Gamma_{\mathrm{ex}} \tag{1.14}$$

and

$$CD^{*} = -D \tag{1.15}$$

from energy conservation and time-reversal symmetry, respectively. The matrix Γ_{ex} contains the energy decay rates of the modes into the ports $\mathbf{s}^{-}$. If those ports together describe all energy decay in the system, $\Gamma_{\mathrm{ex}} = 2\mathrm{Im}[M]$. If there is intrinsic loss (*e.g.,* absorption) at rates $\kappa_{i,0}$ contributing to κ_i, Γ_{ex} can be corrected by subtracting the intrinsic loss rates from the diagonal elements of Γ_{ex}:

$$\Gamma_{\mathrm{ex}} = 2\mathrm{Im}[M] - \mathrm{diag}(\kappa_{i,0}, \kappa_{i+1,0}, ...). \tag{1.16}$$

Using the expression for Γ_{ex}, which now contains the mode-to-port coupling rates $\kappa_{i,\mathrm{ex}}$, together with eq. (1.14) results in the $\sqrt{\kappa_{\mathrm{ex}}}$ mode-to-port coupling factor that we introduced in section 1.2.

Equations (1.14) and (1.15) determine to a large degree the coupling coefficients in D. Remaining ambiguities can generally be solved by considering the symmetry of the modes with respect to the output ports, where one has to carefully take into account the reference planes in the ports to be consistent with the phases of C. Connecting back to the input-output discussion in section 1.2, we note that in the description as generally used in CQED (eq. (1.8)), the input and output fields are by convention related via the identity operator if the cavity is absent. This results from a specific choice of phase for the ingoing and outgoing fields which is not commensurate with the convention $K = D^{\mathrm{T}}$. In appendix B we discuss this in more detail, and show how one can transform between the CQED input-output formalism and coupled-mode theory discussed here.

1.3.1 Coupled resonator response

Here we discuss the response of resonator a_1 when it is coupled to resonator a_2 (fig. 1.3a). The main purpose of this section is to get familiar with modifications of a resonator's susceptibility due to the presence of another (more narrow) resonator (see also [21]), which is a situation we will frequently encounter later

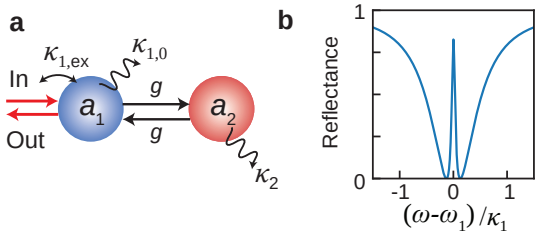

Figure 1.3: Response measurement on two coupled resonators. **a**, The response (susceptibility) of resonator a_1 is modified due to its coupling at rate g to resonator a_2. **b**, The reflectance $|r|^2$ for this system as a function of normalized detuning. When the input field is critically coupled to resonator a_1 ($\kappa_{1,\mathrm{ex}} = \kappa_{1,0}$) the reflectance exhibits a broad resonant dip. In a narrow spectral window, when the frequency of the incoming light matches the resonance frequency of both resonators, resonator a_1 is rendered transparent, yielding a so-called induced transparency peak. This figure is made using a cooperativity $\mathcal{C} = 10$.

in this thesis. We start from the coupled equations listed in eq. (1.13) and choose a_2 to be a spectrally more narrow resonator (such that $\kappa_2 \ll \kappa_1$). In our response measurement we only interrogate resonator a_1 directly such that $\mathbf{s}^+ = s_1^+$, and we assume the absence of far-field interference. The latter ensures that we can set the coupling rates between both resonators equivalent to $g_- = g_+ = g \in \mathbb{R}$. Solving eq. (1.13) for a_1 and using the input-output relation contained in eq. (1.7) we obtain the outward going field s_1^-. Suppose that we perform a reflection measurement, such that the reflection coefficient $r = s_1^-/s_1^+$, the reflectance is obtained as

$$|r|^2 = \left| 1 - \frac{2\eta}{2(\omega-\omega_1)/\mathrm{i}\kappa_1 + 1 + \frac{\mathcal{C}}{2(\omega-\omega_2)/\mathrm{i}\kappa_2 + 1}} \right|^2, \tag{1.17}$$

where we parametrized the coupling between the resonators using the dimensionless cooperativity $\mathcal{C}$ via $\mathcal{C} = 4g^2/(\kappa_1\kappa_2)$, and inserted the coupling efficiency η defined as $\eta \equiv \kappa_{1,\mathrm{ex}}/\kappa_1$. In fig. 1.3b we plot $|r|^2$ for $\omega_1 = \omega_2$, assuming the critical coupling condition ($\eta = 0.5$), as a function of normalized detuning ($[\omega - \omega_1]/\kappa_1$). Enforcing critical coupling ensures that the broadband dip in reflectance, which relates to the response of resonator a_1, goes down to $|r|^2 \approx 0$. The most striking feature is the observation that the second narrow resonator can alter the susceptibility of the broad resonator over a small spectral bandwidth that is centred at ω_2. This reflectance peak results from a reduced susceptibility of resonator a_1, effectively rendering it transparent to the incoming drive field. For atoms this effect is known as electromagnetically induced transparency (EIT) and was first observed by Boller *et al.* [22]. In the following chapters we will frequently encounter this effect. First, in chapter 3 we use a high-Q optical resonator to create an optical transparency window in the response of plasmon particles. Afterwards, in part II of this thesis, the

optical modes of the high-Q resonator are coupled to a more narrow *mechanical* resonance. This leads to an optomechanically induced transparency (OMIT) effect, discussed in section 1.5.3, that we will use to break Lorentz reciprocity for light.

1.4 Optical resonators: rings and antennas

Important and frequently-studied on-chip optical resonators include photonic-crystal cavities [23], whispering-gallery-mode ring resonators [24] and plasmonic resonators (nano-antennas) [25, 26]. These types of systems find widespread application in the enhancement of light-matter interactions, *i.e.* in converting energy that is stored in matter into radiation to interact with the outside world. Moreover, tailored and unusual optical responses can be obtained by coupling multiple resonators. For example, coupled plasmonic resonators can be used to create 'EIT-like' phenomena: the so-called plasmonic analogue of electromagnetically induced transparency [27, 28]. In these systems, the interference between broad- and narrow-linewidth plasmon modes gives rise to the characteristic Fano-lineshape [29] often observed in EIT, effectively rendering the broad plasmon resonance transparent to an incoming field. Interestingly, recent predictions [30, 31] suggest that broadband ($Q \sim 5$) plasmon antennas can also exhibit transparency-like features when they are coupled to a narrowband ring resonator cavity. In part I of this thesis we study such a combined cavity-antenna system (fig. 1.4). Below we introduce ring resonators and nanoantennas, and comment on some of their properties that are useful for the understanding of techniques and methods presented in later chapters.

1.4.1 Ring resonators

Whispering-gallery-mode resonators [24] confine propagating waves in ring-like systems. Due to the refractive index contrast between the resonator's medium and the environment (usually air), light is trapped inside the ring: The propagating waves experience total-internal reflection at the cavity boundaries, thus preventing light to escape. Due to this light-confinement, ring resonators can exhibit very high quality factors ($> 10^5$) and thus extremely narrow linewidths. As a result of the high Qs, ring resonators can be used as very sensitive detectors, which has, for example, enabled the detection of single particles [32, 33].

The first microscale high-Q ring resonators were simple spherical glass resonators fabricated from bare optical fibre [34]. Nowadays, various structures and implementations exist, which are primarily discriminated based on the type of material that is used (and related to this, the size of the ring) and the exact shape. Next to spherical glass resonators, common ring resonator structures include microdisks and bottle- and microtoroid resonators (see [24]

and references therein). As ring resonators are fabricated from high-index materials, simple free-space excitation is impossible. Instead, one often employs so-called tapered optical fibres [35]. The evanescent field of the propagating wave in the fibre extends outside the fibre boundaries and allows the efficient in- and out-coupling of light into the resonator when the local wavevectors of light in the ring and in the fibre are matched. In this thesis we use microtoroid resonators (fig. 1.4a) and rely on tapered fibres to interrogate our system. Tapered fibres are often made from standard optical fibres by a 'melting and pulling' procedure. An excellent description of a fibre-pulling setup is provided in [36], and we will not further discuss the required setup and fabrication procedure in this thesis.

Due to the topology of rings, ideal ring resonators support two degenerate optical modes, which are usually referred to as the clockwise (CW) and counterclockwise (CCW) propagating modes. In practical systems, especially when considering high-Q (meaning narrow linewidth) resonances, so-called mode coupling can be observed experimentally [37]. Intuitively this can be explained as resulting from scattering by inhomogeneities on the resonators' surface. As a result, both the CW and CCW modes in the ring are populated. The scatterer thus couples both propagating modes, which results in two standing wave modes (an even and odd mode) inside the ring [38, 39]. We note, however, that also in the absence of mode coupling one can use the even and odd mode basis. In the absence of mode coupling, the coherent sum of these standing wave modes is exactly equal to one of the two propagating modes (which one depends on the phase with which these standing waves are excited, as discussed in chapter 5). Importantly, however, the even and odd standing wave modes are inherently reciprocal (having contributions from both the CCW and CW propagating modes), in contrast to the CW and CCW mode themselves which do not satisfy the convention $K = D^{\mathrm{T}}$. As a result, the standing-wave mode basis provides a convenient description that can be directly used together with

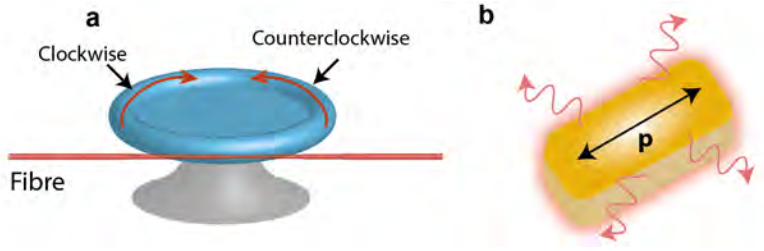

Figure 1.4: Cartoons of optical resonators used in this work. **a**, A microtoroid ring resonator supports two optical modes. It is possible to couple to these modes using a tapered optical fibre. In this thesis we use microtoroids with typical diameters of ∼40 µm. **b**, An optical nanoantenna (typical length ∼400 nm) with dipole moment **p** scatters light.

the coupled-mode theory discussed in section 1.3.

1.4.2 Nanoantennas

Plasmonic nanoantennas [26, 40] are strongly scattering systems that can be used to convert localized energy, for example that of an excited emitter, into far-field radiation (light). When an antenna is small with respect to the wavelength of incoming light, it can be treated as a point dipole which significantly simplifies theoretical descriptions [41, 42]. The induced dipole moment at the antenna position is related to an incoming field via the relation $\mathbf{p} = \overleftrightarrow{\alpha}\,\mathbf{E}$, with $\mathbf{E}$ an incoming drive field. Here we identify the *polarizability* tensor $\overleftrightarrow{\alpha}$, which can be viewed as the linear response function of an antenna. It is the polarizability that describes how strong, and at what frequency, antennas can scatter. If $\overleftrightarrow{\alpha}$ is diagonal and we denote the magnitude of the polarizability in the direction of the incident field by α, the polarizability for metal nanoantennas resembles a Fröhlich mode and takes the spectral shape $\alpha(\omega) \propto [\omega_\mathrm{a}^2 - \omega^2 - \mathrm{i}\gamma\omega]^{-1}$, where ω_a and γ are the antennas resonance frequency and linewidth, respectively, and ω the frequency of the incident field $\mathbf{E}$ [43, 44]. Hence, α has a similar mathematical form as the susceptibility χ of a damped harmonic oscillator that we discussed in section 1.1. Interestingly, the antenna's polarizability, and thus its susceptibility towards an incoming field, needs to be corrected for fields that are scattered by the antenna itself [44]. This effect is known as backaction, and will be more intensively discussed in chapter 3. Using the similarity between χ (section 1.1) and the polarizability, we note that the imaginary part of α can be associated with the total dissipation rate of an antenna. Analogously, this means that the extinction of light from an incoming field due to the antenna, parametrized via the extinction cross-section, also depends on the imaginary part of the polarizability [45]. A measurement probing the (changing) antenna extinction thus allows one to say if the imaginary part of the polarizability has changed.

1.5 Cavity optomechanical mode coupling

The first experiments confirming that light carries momentum, and can thus exert a force, were performed at the start of the twentieth century [46, 47]. Since these initial demonstrations of 'radiation pressure', optical forces have been used to, for example, trap beads in 'optical tweezers' [48] and to cool atoms and ions [49, 50]. The field of cavity optomechanics [15] takes these efforts a step further and studies the coupling between an optical cavity and a macroscopic mechanical resonator. In contrast to light that simply bounces off a surface or atom, light that is squeezed into an optical cavity is stored in time and confined in space, which strongly enhances the optomechanical interaction. In the recent past, this coupling between light and motion has

been used to, for example, sideband-cool a mechanical resonator into its mechanical ground state [51, 52], generate squeezed light [53, 54] and to detect gravitational waves [55]. Of particular importance for this thesis is that cavity optomechanical systems have also shown the capacity to transfer optical (or microwave) signals from one optical mode to another when both optical modes are coupled to a shared mechanical resonator [56–58]. In part II of this thesis we show that under suitable conditions this mechanically-mediated mode-transfer process can imprint a nonreciprocal phase on optical photons. This is experimentally investigated in chapter 5 and chapter 6, where we use this effect to build an optomechanical isolator and circulator, respectively. As we will show, nonreciprocal light transmission in certain situations critically depends on a so-called optomechanically induced transparency (OMIT) window [59, 60]. Section 1.5.3 provides a short introduction into the basics of this effect.

Although there exist a variety of optomechanical implementations (see ref. [15] for a recent overview), most systems can be described by the model system shown in fig. 1.5a. This typical optomechanical system consists of two partially transparent mirrors, thus forming a Fabry-Pérot cavity, where one of the mirrors can vibrate. In contrast, the optomechanical cavities explored in this thesis are microtoroid ring resonators (fig. 1.5b/c). In these systems it is the mechanical radial-breathing mode that modifies the circumference of the ring resonator [61], thus coupling the optical and mechanical degrees of freedom (fig. 1.5c). Importantly, the typical optical linewidth κ of these microtoroids is smaller than their mechanical resonance frequency Ω_m. This condition allows one to make the so-called sideband-resolved approximation, which significantly simplifies the theoretical discussion presented in section 1.5.3.

1.5.1 Optomechanical Hamiltonian: parametric mode coupling

Here we provide the theoretical formalism [15, 62] that is used to describe most optomechanical systems, including the optomechanical resonators depicted in fig. 1.5. The displacement x of a mechanical resonator that vibrates at frequency Ω_m changes the length of the optical cavity. As a result of this displacement, the optical resonance frequency ω_c is modulated. The Hamiltonian for the parametrically coupled optomechanical systems reads

$$\hat{H} = \hbar\omega_\mathrm{c}(\hat{x})[\hat{a}^\dagger\hat{a} + 1/2] + \hbar\Omega_\mathrm{m}[\hat{b}^\dagger\hat{b} + 1/2], \tag{1.18}$$

where $\hat{a}$ and $\hat{b}$ denote the photon and phonon annihilation operators[‡]. Assuming that the displacement x is small, we expand the cavity frequency around its equilibrium $\bar{\omega}_\mathrm{c}$ as $\omega_\mathrm{c}(\hat{x}) = \bar{\omega}_\mathrm{c} - G\hat{x} = \bar{\omega}_\mathrm{c} - Gx_\mathrm{zpf}(\hat{b} + \hat{b}^\dagger)$, with

[‡]For the ring resonator geometry in fig. 1.5b, depending on the mode basis, the photon operator product $\hat{a}^\dagger\hat{a}$ corresponds to the photon number in a single propagating or standing wave mode.

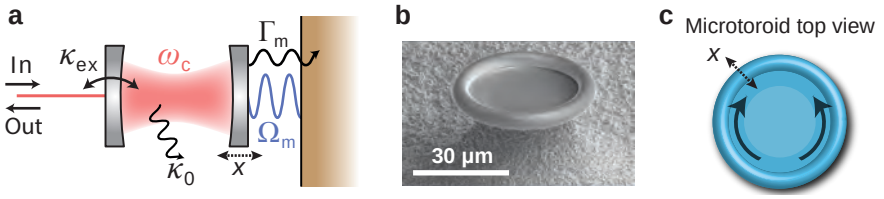

Figure 1.5: Optomechanical interaction. **a**, The typical optomechanical model system consists of two mirrors that form a Fabry-Pérot cavity that supports an optical resonance with frequency ω_c. One of the mirrors is connected, with a spring, to a rigid wall and oscillates at mechanical resonance frequency Ω_m. Via this spring, the mechanical resonator is connected to a reservoir to which it leaks energy (phonons) at rate Γ_m. The optical mode, on the other hand, is connected to two baths at rate κ_{ex} and κ_0, such that the total decay rate of the cavity is $\kappa \equiv \kappa_{ex} + \kappa_0$. Typically the optical cavity is interrogated via the bath (a single-mode waveguide, for example) that is coupled to the cavity at rate κ_{ex}. **b** Scanning electron microscope image of a microtoroid resonator. **c**, Top view of a microtoroid ring resonator. The solid arrows indicate the propagating whispering-gallery modes. Due to the displacement x the circumference of the toroid is modulated in length, which changes the optical resonance frequency of the cavity and couples the mechanical and optical resonance.

x_{zpf} the mechanical zero-point motion, and G the optical frequency shift per unit displacement reading $G = -\partial\omega_c/\partial x$. Inserting this explicit expression for $\omega_c(\hat{x})$ into eq. (1.18) yields

$$\hat{H} = \hbar\bar{\omega}_c\hat{a}^\dagger\hat{a} + \hbar\Omega_m\hat{b}^\dagger\hat{b} - \hbar g_0\hat{a}^\dagger\hat{a}(\hat{b} + \hat{b}^\dagger), \tag{1.19}$$

where the single-photon phonon coupling-rate $g_0 \equiv Gx_{zpf}$ is introduced and the zero-point energy (that only provides an energy offset) is omitted for ease of notation. The final term in eq. (1.19) describes the interaction between the optical and mechanical resonator and is conveniently known as the interaction Hamiltonian $\hat{H}_{int}$. To open this up to now closed system to its environment, for example to an external laser field (oscillating at ω_l), we add an additional drive term

$$\hat{H}_{drive} = i\hbar\sqrt{\kappa_{ex}}\,\hat{s}_{in}\hat{a}^\dagger \exp(-i\omega_l t) + \text{h.c.} \tag{1.20}$$

to the Hamiltonian of the system [12–14]. Here we introduced the rate κ_{ex}, which is the rate at which the incoming drive field is coupled to the optical resonator, and $\hat{s}_{in}$, which is the annihilation operator of the incoming optical drive field. From eq. (1.20) one can read off a 'swapping behaviour', where the destruction of a drive photon from the coherent reservoir is accompanied by the creation of a cavity photon. The Hermitian conjugate (h.c.) signals that the reverse process is also possible, *i.e.* the annihilation of a cavity photon to produce a photon in the bath. Changing into a frame rotating at the laser frequency [15], defining the detuning between laser and cavity as $\Delta \equiv \omega_l - \omega_c$,

we obtain the full optomechanical Hamiltonian

$$\hat{H} = -\hbar\Delta\hat{a}^\dagger\hat{a} + \hbar\Omega_\mathrm{m}\hat{b}^\dagger\hat{b} - \hbar g_0\hat{a}^\dagger\hat{a}(\hat{b}+\hat{b}^\dagger) + [\mathrm{i}\hbar\sqrt{\kappa_\mathrm{ex}}\,\hat{s}_\mathrm{in}\hat{a}^\dagger + \mathrm{h.c.}]. \tag{1.21}$$

1.5.2 Linearized Hamiltonian

The interaction part of the Hamiltonian (the latter term in eq. (1.19)) contains the product of three operators. In the resulting equations of motion these give rise to two-operator products. To remove this non-linearity, the intracavity field can be approximated as fluctuations ($\delta\hat{a}$) that reside on top of a (strong) average coherent field $\bar{\alpha}$, such that $\hat{a} = \bar{\alpha} + \delta\hat{a}$. Hence, $\hat{H}_\mathrm{int}$ is rewritten as

$$\hat{H}_\mathrm{int} = -\hbar g_0|\bar{\alpha}|^2(\hat{b}+\hat{b}^\dagger) - \hbar(g^*\delta\hat{a} + g\delta\hat{a}^\dagger)(\hat{b}+\hat{b}^\dagger), \tag{1.22}$$

where the enhanced optomechanical coupling rate $g \equiv g_0\bar{\alpha}$ is introduced, and the $\delta\hat{a}^\dagger\delta\hat{a}$ term neglected as being smaller by a factor $|\bar{\alpha}|$. Importantly, note that in eq. (1.22) the phase of the coherent drive field is imprinted on the enhanced optomechanical coupling rate g. In principle, the phases of these coupling rates can be used to build systems exhibiting a nonreciprocal phase response. In part II of this thesis, we show that it is the phase in g, as displayed in eq. (1.22), that is of critical importance in the context of a nonreciprocal phase pick-up as observed in an optomechanical mode-conversion process.

Rewriting the term that scales with $|\bar{\alpha}|^2$ as $-\hbar G\hat{x}|\bar{\alpha}|^2$ directly signals the presence of an average radiation-pressure force ($\bar{F} = \hbar G|\bar{\alpha}|^2$), that displaces the mechanical resonator from its original equilibrium position by $\bar{x} = \bar{F}/m_\mathrm{eff}\Omega_\mathrm{m}^2$. This average displacement is taken into account by defining a modified detuning $\bar{\Delta} = \omega_\mathrm{l} - (\bar{\omega}_\mathrm{c} - G\bar{x})$, to yield the linearized Hamiltonian

$$\begin{aligned}\hat{H}_\mathrm{L} = &-\hbar\bar{\Delta}\delta\hat{a}^\dagger\delta\hat{a} + \hbar\Omega_\mathrm{m}\hat{b}^\dagger\hat{b} \\ &- \hbar(\hat{b}+\hat{b}^\dagger)(g^*\delta\hat{a} + g\delta\hat{a}^\dagger) + [\mathrm{i}\hbar\sqrt{\kappa_\mathrm{ex}}\,\delta\hat{s}_\mathrm{in}\delta\hat{a}^\dagger + \mathrm{h.c.}].\end{aligned} \tag{1.23}$$

Note that in this expression all $\hat{a}$'s are replaced by $\delta\hat{a}$, also in the terms that do not involve optomechanical interactions. We do this because our interest is solely with the fluctuations, and not the average, in intracavity field. From $\hat{H}_\mathrm{L}$, the equations of motion for the optical and mechanical resonator are obtained as

$$\delta\dot{\hat{a}} = (\mathrm{i}\bar{\Delta} - \kappa/2)\delta\hat{a} + \mathrm{i}g(\hat{b}+\hat{b}^\dagger) + \sqrt{\kappa_\mathrm{ex}}\delta\hat{s}_\mathrm{in} + \sqrt{\kappa_0}\hat{f}_\mathrm{in}, \tag{1.24}$$

$$\dot{\hat{b}} = (-\mathrm{i}\Omega_\mathrm{m} - \Gamma_\mathrm{m}/2)\hat{b} + \mathrm{i}(g^*\delta\hat{a} + g\delta\hat{a}^\dagger) + \sqrt{\Gamma_\mathrm{m}}\hat{b}_\mathrm{in}, \tag{1.25}$$

where dissipation to the undetected optical bath (at rate κ_0, such that the total optical loss rate $\kappa \equiv \kappa_0 + \kappa_\mathrm{ex}$) and mechanical bath (at rate Γ_m) have been added (see *e.g.* [13]). As a result from this coupling, $\hat{f}_\mathrm{in}$ and $\hat{b}_\mathrm{in}$ contain fluctuations entering from the optical or mechanical bath. Whereas thermal noise at optical frequencies is negligible, the creation of noise phonons that subsequently enter

the optical detection channel (via Stokes or anti-Stokes scattering with the strong drive laser) is undesirable from an information processing perspective. In section 5.4.2 and section 6.4.3 we discuss the effect of thermal noise on our experiment in more detail, but neglect them for now in the remainder of this section.

We note that eq. (1.24) is essentially the same as eq. (1.4), except that the former contains the additional optomechanical coupling term $\mathrm{i}g(\hat{b}+\hat{b}^\dagger)$ and is displayed in the rotating frame. The intracavity field is thus altered due to the coupling to mechanical motion. Conversely, the optical field modifies the equation of motion for the mechanical resonator (eq. (1.25)) via a coupling term that reads $\mathrm{i}(g^*\delta\hat{a}+g\delta\hat{a}^\dagger)$. The coupled eqs. (1.24) and (1.25) are solved in the Fourier domain [15] to give an expression for the small-amplitude optical field $\delta\hat{a}[\omega]$ that reads

$$\delta\hat{a}[\omega]=\frac{-g(\hat{b}[\omega]+\hat{b}^\dagger[\omega])+\mathrm{i}\sqrt{\kappa_{\mathrm{ex}}}\delta\hat{s}_{\mathrm{in}}[\omega]}{\omega+\bar{\Delta}+\mathrm{i}\kappa/2}, \tag{1.26}$$

where $\hat{b}[\omega]$ is the Fourier transform of $\hat{b}$. In the next section we elaborate on the consequence of the optomechanical coupling. For now, we stress that ω is the offset with respect to the oscillating frequency ω_{l} of an applied coherent drive field. Thus for $\omega=0$ we simply look at the response of the cavity at a frequency ω_{l}, and for completeness point out that in the absence of optomechanical interactions ($g=0$) eq. (1.26) is then equivalent to eq. (1.6). To gain more insight in eq. (1.26) we explicitly write $\hat{b}[\omega]+\hat{b}^\dagger[\omega]$ as

$$\hat{b}[\omega]+\hat{b}^\dagger[\omega]=\left(\frac{1}{\omega+\Omega_{\mathrm{m}}+\mathrm{i}\Gamma_{\mathrm{m}}/2}-\frac{1}{\omega-\Omega_{\mathrm{m}}+\mathrm{i}\Gamma_{\mathrm{m}}/2}\right)(g^*\delta\hat{a}[\omega]+g\delta\hat{a}^\dagger[\omega]). \tag{1.27}$$

From this expression we observe that the presence of mechanical motion can lead to optical fields at a frequency ω, captured in the term $\delta\hat{a}[\omega]$, but also at frequency $-\omega$, as contained in $\delta\hat{a}^\dagger[\omega]$[§]. We use this information to explain the concept of optomechanically induced transparency (OMIT).

1.5.3 Optomechanically Induced Transparency

Consider the scenario where we position our strong coherent drive laser, the control laser, at a frequency that is red detuned with respect to the cavity frequency (fig. 1.6a, red arrow). More specifically, we choose this detuning condition such that $\bar{\Delta}=-\Omega_{\mathrm{m}}$. Next, we introduce a second light source, a probe laser, that is coherent with the control laser and offset in frequency by ω. For the red detuning condition, this probe laser is resonant with the optical cavity when $\omega\approx\Omega_{\mathrm{m}}$. As a result of these frequency-detuned (by $\approx\Omega_{\mathrm{m}}$) optical fields that enter the optical cavity, the mechanical resonator experiences

[§]Note that $\delta\hat{a}^\dagger[\omega]=(\delta\hat{a}[-\omega])^\dagger$ [15].

a time-varying radiation pressure force that coherently drives the mechanical motion. In turn, the mechanical motion creates coherent field contributions at positive and negative ω. These contributions, resulting from a modulation by the mechanical resonator, can be viewed as sidebands (Stokes and anti-Stokes scattered fields) that are generated from the control laser. In the resolved-sideband regime, which applies when the mechanical resonance frequency is larger than the optical linewidth ($\Omega_\mathrm{m} > \kappa$), one of the sidebands (the negative frequency component $\delta\hat{a}^\dagger[\omega]$) is far off-resonant with the cavity and as a result can be neglected.

To find the complex mode amplitude (switching to the classical field notation) of the cavity for this two-colour driven system, we combine eqs. (1.26) and (1.27) to obtain

$$\delta a = \frac{\mathrm{i}\sqrt{\kappa_\mathrm{ex}}\delta s_\mathrm{in}}{\omega + \bar{\Delta} + \mathrm{i}\kappa/2 + (1/\Sigma^+ - 1/\Sigma^-)\,|g|^2}, \tag{1.28}$$

where the inverse mechanical susceptibilities $\Sigma^\mp = [\omega \mp \Omega_\mathrm{m} + \mathrm{i}\Gamma_\mathrm{m}/2]$ have been introduced. Together with the input-output relation listed in eq. (1.7), eq. (1.28) allows to calculate the response of our two-color experiment. Figure 1.6b shows the response $|r|^2$, with r defined as $r \equiv \delta s_\mathrm{out}/\delta s_\mathrm{in}$, for a red-detuned control laser ($\bar{\Delta} = -\Omega_\mathrm{m}$) while sweeping the probe-control detuning

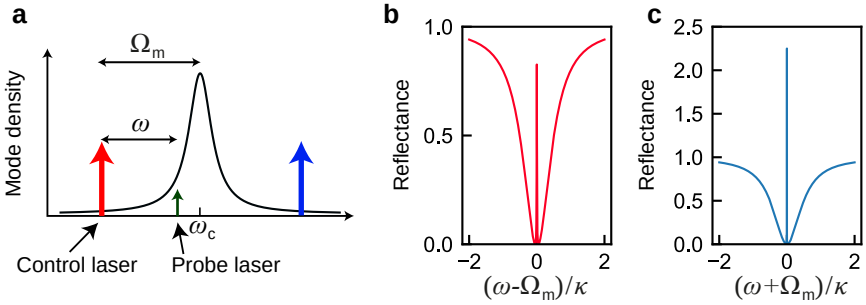

Figure 1.6: Optomechanically induced transparency. **a**, The creation of an optomechanically induced transparency window requires two coherent sources, 1) a strong control field that is either red- or blue-detuned (signalled by the red and blue arrows, respectively) with respect to the cavity mode, and 2) a small probe field (green arrow) that is offset by a frequency ω with respect to the control frequency. We stress that in the red(blue)-detuned scenario the offset frequency ω is positive(negative). **b**/**c**, Reflectance as a function of normalized probe-control detuning with the control frequency tuned to the red (**b**) and blue (**c**) sideband. For the red-detuned case, the OMIT peak results from destructive interference in the cavity, meaning that the induced transparency peak can not reach values higher than unity. In contrast, with the control field tuned to the blue-sideband, the control laser provides gain to the optical probe field and the mechanical resonator (the Stokes interaction creates a photon and a phonon), thus allowing a reflectance signal higher than unity.

ω. For the critical coupling condition considered here, the response exhibits a broadband dip with a width equal to the cavity linewidth κ. The most striking feature in this spectrum is the narrow feature exactly at zero detuning, where the *optical* resonator is effectively rendered 'transparent' to the incoming probe field due to its coupling with the mechanical resonator. This optomechanically induced transparency window results from destructive intracavity interference of 1) the incident probe field, and 2) the anti-Stokes sideband of the control laser generated by the optically driven mechanical resonator. In fact, for the red-detuned scenario this is equivalent to electromagnetically induced transparency observed for cold atoms [22]. In optomechanical systems, OMIT was first demonstrated in microtoroid ring resonators [59] and, shortly thereafter, also in optomechanical crystals [60]. Similar to the discussion provided in section 1.3, the height of the OMIT peak depends on the coupling strength between optical and mechanical resonator, and is parametrized via the cooperativity $\mathcal{C}$, here defined as $\mathcal{C} = 4|g|^2/\kappa\Gamma_\mathrm{m}$. In fig. 1.6b we use a cooperativity of $\mathcal{C} = 10$. Finally, we note that a red-detuned control laser *cools* the mechanical resonator, *i.e.* reduces the number of phonons, via a process that is known as sideband cooling [63, 64]. This is a direct result of the cavity-enhanced anti-Stokes scattering process that generates the sideband at the probe frequency. As the control laser lacks the energy to generate a probe photon by itself, energy conservation dictates the 'consumption' of a mechanical excitation, *i.e.* phonon. A useful side-effect of this cooling mechanism is that the mechanical resonator exhibits an *effective* bandwidth Γ_eff that is increased from its original value Γ_m via the relation $\Gamma_\mathrm{eff} = \Gamma_\mathrm{m}(1 + \mathcal{C})$ [63, 64]. We stress that the optomechanically induced transparency peak as a result of this cooling effect also widens.

We conclude this section by noting that it is also possible to create a transparency effect with the control laser tuned to the blue sideband ($\bar{\Delta} = +\Omega_\mathrm{m}$) of the cavity mode. In this scenario, the control laser has an excess in energy with respect to the cavity mode. As a result, the optomechanical cavity 'selects' the Stokes scattering process, thereby dumping energy from the control laser into the optical mode (at the probe frequency) and mechanical mode simultaneously. As we show in fig. 1.6c, this scenario effectively provides gain (amplification), such that the total reflectance at the probe frequency can exceed unity. In terms of interference, this process can be seen as the opposite of the red-detuned scenario: the incident probe field and Stokes sideband of the control laser *constructively* interfere inside the cavity.

1.6 Outline of this thesis

This thesis investigates the ability to tailor the optical response of coupled resonator systems. In particular, we study high quality-factor toroidal ring resonators by resonantly coupling them to either plasmonic nanoantennas or to mechanical modes of the structure. The coupled systems exhibit a non-trivial

response due to retardation and the breaking of time-reversal symmetry.

Part I: Cavity-Antenna Hybrid Systems

In the first part of this thesis, we study the interaction between ring resonators and plasmonic nanoantennas. Both are known to significantly enhance light-matter interactions, but do so in different ways; ring resonators employ their high quality factor (high-Q) modes, while plasmonic antennas take advantage of low mode volumes V. Limitations of their applicability include a spectrally narrow enhancement window (for the ring resonator) and large absorption losses (for the plasmon antenna). A resonantly coupled combination of the two, creating a hybrid cavity-antenna system, could alleviate some of these constraints and allow optimized light-matter interactions in tailored systems. Here, the optical response of such a hybrid cavity-antenna system is experimentally investigated.

In **chapter two**, we study how the resonant mode of a microtoroid ring resonator changes when it is subject to a perturbation by an array of nanoantennas placed in its near field. In contrast to the widely accepted notion that the mode perturbation, in terms of a cavity frequency shift, can be directly related to the resonant polarizability of the introduced perturbation, we show that when radiation losses emerging from both the cavity and antenna can interfere, the resultant frequency shifts are pronouncedly altered. As we discuss, this interference is a form of radiative mode coupling that results in cavity frequency shifts that are opposite to what would be expected based on the antenna polarizability alone. We present an analytical model explaining the effect.

In **chapter three**, this experimental system is interrogated by observing the linear response of the nanoantenna array. We study how the polarizability of the nanoantennas changes due to the presence of a high-Q cavity. It was theoretically predicted before that such an interaction could lead to a modification of the antenna polarizability. This is a result of interfering fields at the position of the antenna array and is known as backaction. In this chapter we measure a modification of the polarizability of the array due to cavity-mediated backaction. Moreover, we show that it is possible to control the backaction strength by modifying the incident wavevector.

Part II: Nonreciprocity in Optomechanics

The interaction between an optical and a mechanical mode through radiation pressure is at the core of the field of cavity-optomechanics. Toroidal ring resonators form optomechanical systems whose optical loss rate is generally smaller than the mechanical frequency of the ring's mechanical radial breathing mode. This places this system in the so-called resolved sideband limit, allowing optical cooling of motion and the creation of an optomechanically induced

transparency window. In chapters 4-6 we discuss and demonstrate how such a system can be used to break Lorentz reciprocity for light.

The discussion on nonreciprocal light transmission is started in **chapter four**, with theoretical investigations on an optomechanical system that involves two optical modes coupled to a joint mechanical degree of freedom. A suitable laser drive biases the optomechanical couplings, resulting in nonreciprocal mode transfer in the system, and thus acts as an effective magnetic field for light. Two distinct implementations are discussed, which employ either the optical or mechanical bath to remove light in the unwanted propagation direction, with different implications on bandwidth and power of operation.

In **chapter five**, we put the theory developed in chapter four to test in an experimental system that revolves around an optomechanical toroidal ring resonator. We show that under the appropriate conditions it is possible to achieve nonreciprocal amplitude and phase transmission in this system. Both isolation (10 dB) and unidirectional amplification are demonstrated. In addition, we present results that show the persistence of the nonreciprocal effect for nondegenerate optical modes.

In **chapter six**, we employ the aforementioned optomechanical interaction to demonstrate an on-chip four-port circulator, extending the geometry that is studied in chapter five with two additional input and output ports. This technically challenging system is realized by simultaneously coupling two tapered optical fibres to a single toroidal ring resonator. Using a suitably tailored measurement scheme, we are able to do measurements on all 16 scattering parameters that describe the four-port circulator. Experimentally we obtain approximately 10 dB of isolation in all circulator channels at a minimum of insertion loss.

References

[1] K. Kao, and G. Hockham, *Dielectric-fibre surface waveguides for optical frequencies*, Proc. Inst. Electr. Eng. **113**, 1151 (1966).

[2] J. Hecht, *City of light: The story of fiber optics* (Oxford University Press, 1999), 2nd ed.

[3] A. Polman, M. Knight, E. C. Garnett, B. Ehrler, and W. C. Sinke, *Photovoltaic materials: Present efficiencies and future challenges*, Science **352**, aad4424 (2016).

[4] *Simply silicon: focus issue*, Nat. Photonics **4**, 491 (2010).

[5] D. Thomson, et al., *Roadmap on silicon photonics*, J. Opt. **18**, 073003 (2016).

[6] H. J. Kimble, *The quantum internet*, Nature **453**, 1023 (2008).

[7] J. L. O'Brien, A. Furusawa, and J. Vučković, *Photonic quantum technologies*, Nat. Photonics **3**, 687 (2009).

[8] P. Lodahl, S. Mahmoodian, and S. Stobbe, *Interfacing single photons and single quantum dots with photonic nanostructures*, Rev. Mod. Phys. **87**, 347 (2015).

[9] H. Goldstein, C. P. Poole, and J. L. Safko, *Classical mechanics* (Addison-Wesley, 2001), 3rd ed.

[10] H. B. Callen, and T. A. Welton, *Irreversibility and generalized noise*, Phys. Rev. **83**, 34 (1951).

[11] R. Kubo, *The fluctuation-dissipation theorem*, Reports Prog. Phys. **29**, 255 (1966).

[12] M. J. Collett, and C. W. Gardiner, *Squeezing of intracavity and traveling-wave light fields produced in parametric amplification*, Phys. Rev. A **30**, 1386 (1984).

[13] C. Gardiner, and P. Zoller, *Quantum noise: a handbook of Markovian and non-Markovian quantum stochastic methods with applications to quantum optics* (Springer Science & Business Media, 2004), 3rd ed.

[14] D. F. Walls, and G. J. Milburn, *Quantum Optics* (Springer Berlin Heidelberg, Berlin, Heidelberg, 2008), 2nd ed.

[15] M. Aspelmeyer, T. J. Kippenberg, and F. Marquardt, *Cavity optomechanics*, Rev. Mod. Phys. **86**, 1391 (2014).

[16] H. A. Haus, *Waves and fields in optoelectronics* (Prentice-Hall, 1984).

[17] S. Fan, W. Suh, and J. D. Joannopoulos, *Temporal coupled-mode theory for the Fano resonance in optical resonators.*, J. Opt. Soc. Am. A **20**, 569 (2003).

[18] W. Suh, Z. Wang, and S. Fan, *Temporal coupled-mode theory and the presence of non-orthogonal modes in lossless multimode cavities*, IEEE J. Quantum Electron. **40**, 1511 (2004).

[19] Y. Aharonov, and D. Bohm, *Significance of electromagnetic potentials in the quantum theory*, Phys. Rev. **115**, 485 (1959).

[20] Z. Yu, and S. Fan, *Complete optical isolation created by indirect interband photonic transitions*, Nat. Photonics **3**, 91 (2009).

[21] C. L. Garrido Alzar, M. A. G. Martinez, and P. Nussenzveig, *Classical analog of electromagnetically induced transparency*, Am. J. Phys. **37**, 6 (2001).

[22] K. Boller, A. Imamoğlu, and S. E. Harris, *Observation of electromagnetically induced transparency*, Phys. Rev. Lett. **66**, 2593 (1991).

[23] J. D. Joannopoulos, P. R. Villeneuve, and S. Fan, *Photonic crystals: putting a new twist on light*, Nature **386**, 143 (1997).

[24] K. J. Vahala, *Optical microcavities*, Nature **424**, 839 (2003).

[25] L. Novotny, and N. van Hulst, *Antennas for light*, Nat. Photonics **5**, 83 (2011).

[26] M. Agio, and A. Alù, *Optical antennas* (Cambridge University Press, 2013).

[27] S. Zhang, D. A. Genov, Y. Wang, M. Liu, and X. Zhang, *Plasmon-induced transparency in metamaterials*, Phys. Rev. Lett. **101**, 047401 (2008).

[28] N. Liu, et al., *Plasmonic analogue of electromagnetically induced transparency at the Drude damping limit.*, Nat. Mater. **8**, 758 (2009).

[29] U. Fano, *Effects of configuration interaction on intensities and phase shifts*, Phys. Rev. **124**, 1866 (1961).

[30] M. Frimmer, and A. F. Koenderink, *Spontaneous emission control in a tunable hybrid photonic system*, Phys. Rev. Lett. **110**, 217405 (2013).

[31] H. M. Doeleman, E. Verhagen, and A. F. Koenderink, *Antenna–cavity hybrids: matching polar opposites for purcell enhancements at any linewidth*, ACS Photonics **3**, 1943 (2016).

[32] F. Vollmer, and S. Arnold, *Whispering-gallery-mode biosensing: label-free detection down to single molecules*, Nat. Methods **5**, 591 (2008).

[33] F. Vollmer, and L. Yang, *Label-free detection with high-Q microcavities: a review of biosensing mechanisms for integrated devices*, Nanophotonics **1**, 267 (2012).

[34] V. Braginsky, M. Gorodetsky, and V. Ilchenko, *Quality-factor and nonlinear properties of optical whispering-gallery modes*, Phys. Lett. A **137**, 393 (1989).

[35] M. Cai, O. Painter, and K. J. Vahala, *Observation of critical coupling in a fiber taper to a silica-microsphere whispering-gallery mode system*, Phys. Rev. Lett. **85**, 74 (2000).

[36] B. D. Hauer, et al., *On-chip cavity optomechanical coupling*, EPJ Tech. Instrum. **1**, 4 (2014).

[37] T. J. Kippenberg, S. M. Spillane, and K. J. Vahala, *Modal coupling in traveling-wave resonators*, Opt. Lett. **27**, 1669 (2002).

[38] A. Mazzei, et al., *Controlled coupling of counterpropagating whispering-gallery modes by a single Rayleigh scatterer: A classical problem in a quantum optical light*, Phys. Rev. Lett. **99**, 173603 (2007).

[39] K. Srinivasan, and O. Painter, *Mode coupling and cavity–quantum-dot interactions in a fiber-coupled microdisk cavity*, Phys. Rev. A **75**, 023814 (2007).

[40] A. F. Koenderink, *Single-Photon Nanoantennas*, ACS Photonics **4**, 710 (2017).

[41] L. Novotny, and B. Hecht, *Principles of nano-optics* (Cambridge University Press, Cambridge, 2012), 2nd ed.

[42] M. Frimmer, *Spontaneous emission near resonant optical antennas*, Ph.D. thesis, University of Amsterdam (2012).

[43] A. Lagendijk, and B. A. van Tiggelen, *Resonant multiple scattering of light*, Phys. Rep. **270**, 143 (1996).

[44] P. de Vries, D. V. van Coevorden, and A. Lagendijk, *Point scatterers for classical waves*, Rev. Mod. Phys. **70**, 447 (1998).

[45] C. F. Bohren, and D. R. Huffman, *Absorption and scattering of light by small particles* (John Wiley and Sons, 1983).

[46] P. Lebedew, *Untersuchungen über die Druckkräfte des Lichtes*, Ann. Phys. **311**, 433 (1901).

[47] E. F. Nichols, and G. F. Hull, *A preliminary communication on the pressure of heat and light radiation*, Phys. Rev. (Series I) **13**, 307 (1901).

[48] A. Ashkin, *Acceleration and trapping of particles by radiation pressure*, Phys. Rev. Lett. **24**, 156 (1970).

[49] D. J. Wineland, R. E. Drullinger, and F. L. Walls, *Radiation-pressure cooling of bound resonant absorbers*, Phys. Rev. Lett. **40**, 1639 (1978).

[50] S. Stenholm, *The semiclassical theory of laser cooling*, Rev. Mod. Phys. **58**, 699 (1986).

[51] J. Chan, et al., *Laser cooling of a nanomechanical oscillator into its quantum ground state*, Nature **478**, 89 (2011).

[52] J. D. Teufel, et al., *Sideband cooling of micromechanical motion to the quantum ground state.*, Nature **475**, 359 (2011).

[53] A. H. Safavi-Naeini, et al., *Squeezed light from a silicon micromechanical resonator.*, Nature **500**, 185 (2013).

[54] T. P. Purdy, P.-L. Yu, R. W. Peterson, N. S. Kampel, and C. A. Regal, *Strong optomechanical squeezing of light*, Phys. Rev. X **3**, 031012 (2013).

[55] B. P. Abbott, et al., *Observation of gravitational waves from a binary black hole merger*, Phys. Rev. Lett. **116**, 061102 (2016).

[56] J. T. Hill, A. H. Safavi-Naeini, J. Chan, and O. Painter, *Coherent optical wavelength conversion via cavity optomechanics*, Nat. Commun. **3**, 1196 (2012).

[57] R. W. Andrews, et al., *Bidirectional and efficient conversion between microwave and optical light*, Nat. Phys. **10**, 321 (2014).

[58] F. Lecocq, J. B. Clark, R. W. Simmonds, J. Aumentado, and J. D. Teufel, *Mechanically mediated microwave frequency conversion in the quantum regime*, Phys. Rev. Lett. **116**, 043601 (2016).

[59] S. Weis, et al., *Optomechanically induced transparency*, Science **330**, 1520 (2010).

[60] A. H. Safavi-Naeini, et al., *Electromagnetically induced transparency and slow light with optomechanics*, Nature **472**, 69 (2011).

[61] T. J. Kippenberg, H. Rokhsari, T. Carmon, A. Scherer, and K. J. Vahala, *Analysis of radiation-pressure induced mechanical oscillation of an optical microcavity*, Phys. Rev. Lett. **95**, 033901 (2005).

[62] C. K. Law, *Interaction between a moving mirror and radiation pressure: A Hamiltonian formulation*, Phys. Rev. A **51**, 2537 (1995).

[63] F. Marquardt, J. P. Chen, A. A. Clerk, and S. M. Girvin, *Quantum theory of cavity-assisted sideband cooling of mechanical motion*, Phys. Rev. Lett. **99**, 093902 (2007).

[64] I. Wilson-Rae, N. Nooshi, W. Zwerger, and T. J. Kippenberg, *Theory of ground state cooling of a mechanical oscillator using dynamical backaction*, Phys. Rev. Lett. **99**, 093901 (2007).

Part I

Optical Interactions in Cavity-Antenna Hybrid Systems

Chapter 2

Resonance Frequency Shifts in a Radiating Cavity Perturbed by Antennas

The influence of a small perturbation on a cavity mode plays an important role in fields like optical sensing, cavity quantum electrodynamics and cavity optomechanics. Typically, the resulting cavity frequency shift directly relates to the polarizability of the perturbation. Here we demonstrate that particles perturbing a radiating cavity can induce strong frequency shifts that are opposite to, and even exceed, the effects based on the particles' polarizability. A full electrodynamic theory reveals that these anomalous results rely on a non-trivial phase relation between cavity and nanoparticle radiation, allowing backaction via the radiation continuum. In addition, an intuitive model based on coupled mode theory is presented that relates the phenomenon to retardation. Because of the ubiquity of dissipation, we expect these findings to benefit the understanding and engineering of a wide class of systems.

2.1 Introduction

The fact that a small perturbation of a potential can influence the distribution of a system's energy levels is a well-known principle permeating various branches of physics. In quantum mechanics, for example, the effect of a perturbing potential H' on an eigenstate $|\psi_0\rangle$ is that it modifies its unperturbed energy U_0 by an amount $\delta U = \langle\psi_0|H'|\psi\rangle$, where $|\psi\rangle$ is the new eigenstate and we assume $\langle\psi_0|\psi\rangle \approx 1$. In electrodynamics, a local change of potential (*i.e.* permittivity) can impact the frequency of a resonant cavity. This is at the basis of many applications that use the influence of a perturbing atom, molecule, or dielectric body to establish an interaction that can be exploited for optical sensing or control [1–8]. The shift of a mode's complex eigenfrequency $\omega = \omega_c - i\kappa/2$, with cavity resonance frequency ω_c and linewidth κ, due to a local permittivity perturbation $\Delta\epsilon$ contained in a volume ΔV is given by

$$\delta\omega/\omega = -\int_{\Delta V} dV \left[\epsilon_0 \Delta\epsilon \mathbf{E}_0^* \cdot \mathbf{E}_p\right] / 4U_0. \tag{2.1}$$

Here $\mathbf{E}_0$ and U_0 represent the field and total energy of the unperturbed cavity mode, respectively, and $\mathbf{E}_p$ is the perturbed field [9, 10]. In close analogy to quantum mechanics, where one performs an integral over a perturbed potential H', eq. (2.1) requires an integral over the perturbed permittivity $\Delta\epsilon$. Similarly, $\mathbf{E}_0$ and $\mathbf{E}_p$ represent the electromagnetic equivalent of the unperturbed (ψ_0) and perturbed (ψ) quantum mechanical wave function, respectively. In particular, if ΔV is small enough such that the perturbing particle can be described in the dipole approximation, the complex frequency shift is directly related to the particle *polarizability* α, reading $\delta\omega/\omega = -\alpha|\mathbf{E}_0|^2/4U_0$ [9]. However,

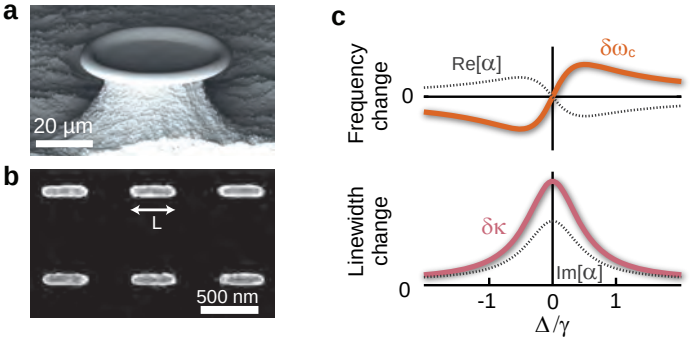

Figure 2.1: Introducing the hybrid cavity-nanoantenna system. **a**, Scanning electron microscopy (SEM) image of a high-Q silica microtoroid at the edge of a chip. **b**, SEM image of gold nanoantennas on a glass substrate. **c**, Cavity frequency and linewidth change due to perturbation by a small resonator, considering only the resonator polarizability. Dashed lines indicate the real (top) and imaginary (bottom) part of the polarizability as a function of Δ/γ.

this widely employed result of Bethe-Schwinger perturbation theory [10] is strictly only valid when radiation to the far field is negligible. In several recent developments, radiation loss proved decisive in determining a system's eigenmode, *e.g.* for so-called 'bound states in the continuum' [11–16] and in describing complex plasmonic resonators [17, 18]. In that context, the question arises to what extent the conventional paradigm to determine perturbed cavity frequencies holds in practical, open, systems.

In this chapter, we study the eigenfrequencies of a radiating optical whispering-gallery-mode cavity (fig. 2.1a) as it is perturbed by carefully designed resonant plasmonic nanoparticles (fig. 2.1b). For a resonant perturbation with center frequency ω_a and linewidth γ, the value of α strongly depends on the detuning $\Delta = \omega_c - \omega_a$. In absence of radiation, the cavity mode redshifts(blueshifts) at negative(positive) values of Δ and the linewidth broadens near $\Delta = 0$, in direct response to $\mathrm{Re}[\alpha]$ and $\mathrm{Im}[\alpha]$, respectively (fig. 2.1c). Tuning ω_a by varying the length of the (plasmonic) resonators allows to systematically study the induced cavity response as a function of detuning. Importantly, our experiment is designed such that radiation losses from the cavity mode and plasmonic resonators overlap. This, as we will show, leads to a strong additional contribution to $\delta\omega$ which is not captured by α. We study this 'radiation interaction', as we will call the effect, in detail and show that it can induce strong eigenfrequency shifts that are opposite to, and even exceed, the effects based on the particles' polarizability.

2.2 Experimental procedure

A cartoon of the hybrid cavity-antenna system studied here is shown in fig. 2.2a. The experiments are performed using a fundamental cavity mode (194.4 THz, $Q \sim 6.5 \times 10^6$ and TE polarized) of a toroidal silica microcavity [19, 20] that is fabricated on the edge of a silicon chip and has a diameter of approximately 36 µm (fig. 2.1a). The cavity is perturbed by gold nanoantennas on a glass substrate, which are controllably placed in the evanescent field of the cavity. Details about the fabrication of the cavity and nanoantennas, and about the optical setup, are given in appendix 2.A.2. The antennas (nanorods of length L, width 120 nm and thickness 40 nm) are aligned with their (long) principal dipole axis to the polarization of the cavity mode. A frequency-swept narrow-band laser source ($\sim$0.7 µW) is coupled into a tapered fibre that is brought close to the cavity. As fig. 2.2b illustrates, the transmission spectrum through the fibre shows a Lorentzian dip around the cavity resonance frequency, from which we determine the (perturbed) resonance frequency ω_c and linewidth κ of the cavity mode. Independent normal-incidence transmission measurements on the fabricated antenna arrays in absence of the cavity, as shown in fig. 2.2c, yield the normalized cavity-antenna detuning Δ/γ. Notably, the presence of the glass substrate allows the cavity mode to radiate into the glass at a well

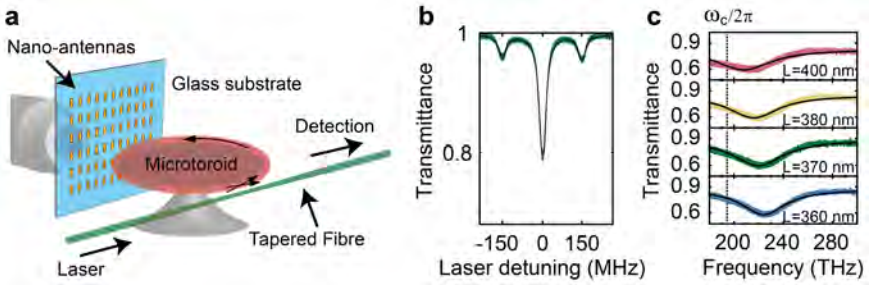

Figure 2.2: Cartoon of the experiment and spectroscopic results. **a**, An array of perturbing gold nanoantennas is placed in the near field of a toroidal microcavity. Light transmittance through the tapered fibre is detected to determine the cavity eigenfrequency shift. **b**, Transmittance through the tapered fibre around a cavity mode resonance. A Lorentzian fit (black solid line) is used to determine the optical linewidth (≈30 MHz) and frequency of the cavity. The sidebands result from a 150-MHz phase modulation used to calibrate the frequency axis. **c**, Normal-incidence transmittance spectra of gold nanoantenna (design length L) arrays. Lorentzian fits (sold lines) give the antenna resonance frequency and linewidth. The dashed line indicates the cavity frequency.

defined angle just beyond the critical angle and, similarly, allows scattering of antenna radiation into the substrate [21]. As the antennas are coherently excited by the cavity field, from which also the cavity radiation originates, the zeroth-order diffraction by the array is expected to partially overlap and interfere with the cavity radiation.

To measure the change of the complex cavity resonance frequency due to the nanoantennas, we compare the frequency and linewidth of the cavity mode with and without the antenna array placed in the near-field of the cavity. Figures 2.3a and b illustrate the experimental procedure. The data is obtained by stepwise scanning the microcavity, which is placed together with the tapered fibre on a piezo-electric stage, sideways along an antenna array and a stretch of bare substrate at a separation distance z≈1.1 µm (based on simulations). During each scan, the cavity-sample distance is kept constant, which is checked before and after each experiment when the cavity is positioned at opposite positions adjacent to the antenna array. This check is performed by monitoring the cavity linewidth (broadened by the presence of the substrate), which depends strongly on the distance to the substrate. Each scan consists of 80-120 steps and multiple scans (2-5) are performed on each array. The change in resonance frequency ($\delta\omega_c$) and linewidth ($\delta\kappa$) due to the antennas is obtained by subtracting the cavity resonance frequency $\omega_{c,ref}$ and linewidth κ_{ref} without the array placed in the near-field of the cavity, from the cavity resonance frequency and linewidth with the antenna array placed in the evanescent field of the cavity mode. Example data for the change in linewidth is shown in fig. 2.3c. To correct for any remaining sample tilt and/or slow drift, reference

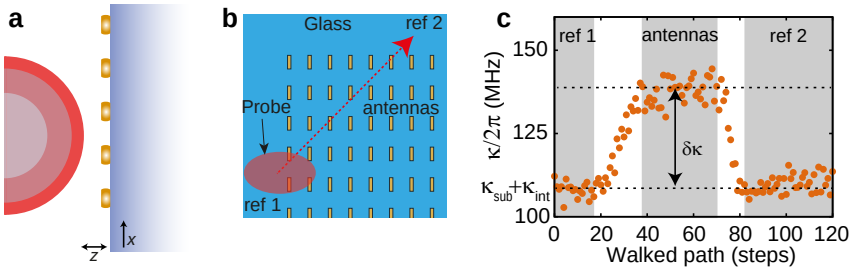

Figure 2.3: Scanning along an array. **a**, The cavity and array geometry. At a fixed distance of $z \approx 1.1\,\mu$m we scan the cavity sideways along the antenna array. **b**, Careful alignment allows us to scan over the antennas by moving our microcavity between two predefined points (ref 1 and ref 2), which serve as our reference measurements on glass. Between those points we measure the effect of the antennas on the cavity mode. **c**, Evolution of the cavity linewidth during a scan along the antenna array, where each point is retrieved from a fit with a Lorentzian lineshape. When scanning along the antennas, we make sure that we see a *plateau* of data points. In our analysis, we only include the data points indicated by the grey regions, thus excluding the data taken during transit between reference and antennas. For the calculation of $\delta\kappa$, we average all the points clearly on the *plateau* and subtract the average reference value on glass ($\kappa_{\mathrm{ref}} = \kappa_{\mathrm{sub}} + \kappa_{\mathrm{int}}$).

measurements on glass taken at the start and end of a scan are averaged. The values of $\delta\omega_{\mathrm{c}}$ and $\delta\kappa$ are calculated excluding data points taken during the transition from glass to array.

Even though we check that all measurements are performed at similar cavity-sample distance, we would like to eliminate any errors due to small variations of that distance. To this end, we retrieve parameters that are robust towards small distance changes by considering the relative change in linewidth and resonance frequency due to the antennas: $\delta\kappa/\kappa_{\mathrm{sub}}$ and $\delta\omega_{\mathrm{c}}/\kappa_{\mathrm{sub}}$, respectively, where κ_{sub} is the broadening the cavity mode experiences due to the glass substrate ($\kappa_{\mathrm{sub}} = \kappa_{\mathrm{ref}} - \kappa_{\mathrm{int}}$, with κ_{int} the decay rate of the bare cavity). Figure 2.4 shows that this method results in a relative change of the resonance frequency ω_{c} and linewidth κ that is independent of the distance to the substrate. It is obvious that this quantity now allows straightforward averaging over multiple scans on the same array and comparison between different antenna arrays. Error bars are obtained by calculating the 'error on the mean' for $\delta\omega_{\mathrm{c}}$ and $\delta\kappa$, while the error (one standard deviation) on ω_{a}, and thus the detuning, is retrieved from a Gaussian fit to the sum of squared residuals, obtained by displacing the fit result with respect to the normal-incidence transmission spectra of the antenna arrays.

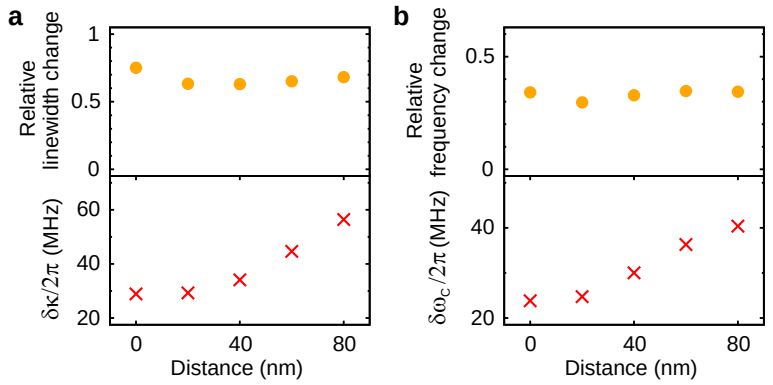

Figure 2.4: Validation of dimensionless parameter. The measured effect on the cavity linewidth (**a**, bottom) and resonance frequency (**b**, bottom) due to the antennas is clearly increasing when the cavity travels a certain distance towards the antennas. Here, a larger distance corresponds to a smaller cavity-antenna separation z. As shown in the top panel of **a** and **b**, our analysis results in a constant dimensionless quantity for the change in linewidth and frequency which does not depend on the distance to the antenna array.

2.3 Experimental results

Figure 2.5a shows the results for two different arrays of nanoantennas: In the top figure, an antenna array ($L = 360$, pitch 800(900) nm along the long(short) axes of the antennas) is seen to induce a broadening of the cavity linewidth, together with a *blueshift* of the frequency. The latter is clearly surprising, given the fact that $\Delta \approx -1.2\gamma$ for this sample (see appendix 2.A.3), where one expects a *redshift* if one only considers the resonant particle's polarizability (fig. 2.1c). The bottom panel in fig. 2.5a shows that for another array ($L = 400$, pitch 800(1100) nm) with slightly positive detuning ($\Delta \approx 0.8\gamma$) again a blueshift is observed, but this time accompanied by *narrowing* of the cavity mode. Such a reduction of damping can obviously not be ascribed to the particle's polarizability alone, as its imaginary part is necessarily positive (fig. 2.1c).

To systematically study these effects, we gradually tune the resonance frequency ω_a by varying the length of the antennas (fig. 2.2c). The array pitch is kept fixed at 800(1500) nm along the long(short) antenna axes, chosen such that inter-antenna coupling is small. Moreover, in all examples we show, Bragg-scattering between clockwise and counter-clockwise modes [22] is small enough such that mode splitting induced by the nanoantennas is smaller than the cavity linewidth. Figure 2.5b shows the resulting cavity frequency and linewidth changes, normalized to the cavity linewidth on glass to allow averaging multiple scans, as a function of Δ/γ. For these negative detunings, a consistent increase of the resonance frequency (*i.e.* blueshift) is observed that slightly rises as the

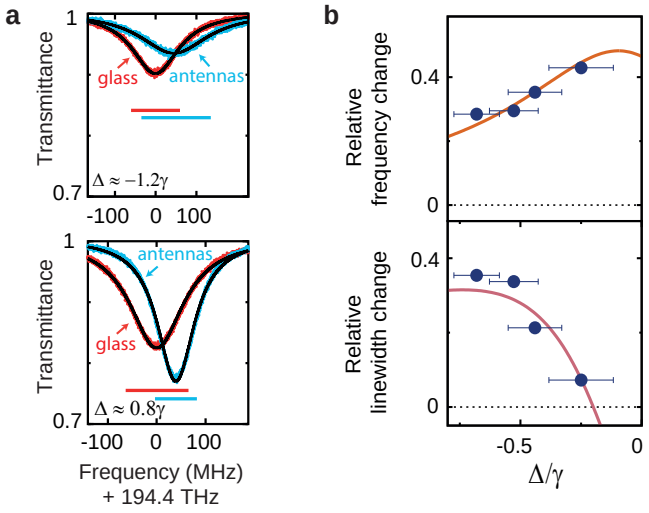

Figure 2.5: Measuring cavity-perturbation. **a**, Depending on the detuning Δ between cavity and antenna resonance frequency, antenna arrays induce linewidth broadening (top) and narrowing (bottom), while simultaneously inducing the cavity resonance frequency to blueshift. The blue and red horizontal bars represent the linewidths of fitted Lorentzian lineshapes (black lines). **b**, Shift in resonance frequency and linewidth of the cavity mode, normalized to its linewidth in absence of the antennas, due to perturbation by antenna arrays with a constant pitch size and varying antenna length. Top: For all detunings a blueshift of cavity resonance frequency is observed. Bottom: Approaching $\Delta = 0$ induces linewidth narrowing. Both the blueshift and linewidth narrowing are contrary to the expectation based on the particles' polarizability (fig. 2.1c). Error bars depict standard deviation, vertical error bars fall within the plot markers. The solid lines represent a fit using the model derived with coupled mode theory (see section 2.6).

antenna frequency approaches that of the cavity. As such, both the sign and the trend of $\delta\omega_c$ are incongruous with the expectation based on the polarizability depicted in fig. 2.1c. Moreover, the broadening of the cavity, observed for a detuning of $\Delta \approx -0.6\gamma$, quickly reduces as the – strongly scattering – antennas are tuned closer to the cavity resonance. We note that these trends are consistently observed also at other periodicities (see appendix 2.A.3) and that the shifts cannot be explained by thermal heating, which is negligible at the employed powers.

2.4 Bethe-Schwinger cavity perturbation with radiation

To explore the origin of these surprising results, it is necessary to consider the complete Bethe-Schwinger cavity perturbation formula [10], derived without

neglecting radiation. We use an approach analogous to [9, 10], and consider the modes of an open cavity described by a spatial distribution of permittivity $\epsilon_0\epsilon(\mathbf{r})$ and permeability $\mu_0\mu(\mathbf{r})$ (in the following, the spatial dependence of both is implicitly assumed). The eigenmodes of the system are found by solving Maxwell's equations in all of space in the absence of external drives. This yields solutions of the form

$$\mathbf{E}(\mathbf{r},t) = \mathbf{E}_0(\mathbf{r})e^{-\mathrm{i}\omega t}, \tag{2.2}$$
$$\mathbf{H}(\mathbf{r},t) = \mathbf{H}_0(\mathbf{r})e^{-\mathrm{i}\omega t}, \tag{2.3}$$

which satisfy Maxwell's equations for some complex frequency

$$\omega = \omega_\mathrm{c} - \mathrm{i}\frac{\kappa}{2}, \tag{2.4}$$

where ω_c and κ denote the (real) resonance frequency and energy decay rate, respectively. Important relationships between $\mathbf{E}_0$ and $\mathbf{H}_0$ now include

$$\nabla\times\mathbf{E}_0 = \mathrm{i}\omega\mu_0\mu\mathbf{H}_0 \qquad \nabla\times\mathbf{E}_0^* = -\mathrm{i}\omega^*\mu_0\mu^*\mathbf{H}_0^*, \tag{2.5}$$
$$\nabla\times\mathbf{H}_0 = -\mathrm{i}\omega\epsilon_0\epsilon\mathbf{E}_0 \qquad \nabla\times\mathbf{H}_0^* = \mathrm{i}\omega^*\epsilon_0\epsilon^*\mathbf{E}_0^*. \tag{2.6}$$

2.4.1 Dielectric perturbation

Next, we consider that the cavity is perturbed, such that in a finite volume ΔV the relative permittivity and permeability are changed to new values

$$\epsilon_\mathrm{p} = \epsilon + \Delta\epsilon, \tag{2.7}$$
$$\mu_\mathrm{p} = \mu + \Delta\mu. \tag{2.8}$$

This perturbed system has different eigenmodes written as

$$\mathbf{E}(\mathbf{r},t) = \mathbf{E}_\mathrm{p}(\mathbf{r})e^{-\mathrm{i}\omega_\mathrm{p}t} = \left(\mathbf{E}_0(\mathbf{r}) + \delta\mathbf{E}(\mathbf{r})\right)e^{-\mathrm{i}(\omega+\delta\omega)t}, \tag{2.9}$$
$$\mathbf{H}(\mathbf{r},t) = \mathbf{H}_\mathrm{p}(\mathbf{r})e^{-\mathrm{i}\omega_\mathrm{p}t} = \left(\mathbf{H}_0(\mathbf{r}) + \delta\mathbf{H}(\mathbf{r})\right)e^{-\mathrm{i}(\omega+\delta\omega)t}, \tag{2.10}$$

where $\mathbf{E}_\mathrm{p}(\mathbf{r})$ and ω_p describe the spatial dependence and resonance frequency of the perturbed cavity mode. Defining $\delta\mathbf{E} \equiv \mathbf{E}_\mathrm{p} - \mathbf{E}_0$, $\delta\mathbf{H} \equiv \mathbf{H}_\mathrm{p} - \mathbf{H}_0$ and $\delta\omega \equiv \omega_\mathrm{p} - \omega$ yields

$$\nabla\times(\mathbf{E}_0 + \delta\mathbf{E}) = \mathrm{i}\left(\omega+\delta\omega\right)\mu_0\mu_\mathrm{p}\left(\mathbf{H}_0 + \delta\mathbf{H}\right), \tag{2.11}$$
$$\nabla\times(\mathbf{H}_0 + \delta\mathbf{H}) = -\mathrm{i}\left(\omega+\delta\omega\right)\epsilon_0\epsilon_\mathrm{p}\left(\mathbf{E}_0 + \delta\mathbf{E}\right). \tag{2.12}$$

Combining the above equations for the curl of the fields gives

$$\nabla\times\delta\mathbf{E} = \mathrm{i}\omega_\mathrm{p}\mu_0\mu_\mathrm{p}\mathbf{H}_\mathrm{p} - \mathrm{i}\omega\mu_0\mu\mathbf{H}_0, \tag{2.13}$$
$$\nabla\times\delta\mathbf{H} = -\mathrm{i}\omega_\mathrm{p}\epsilon_0\epsilon_\mathrm{p}\mathbf{E}_\mathrm{p} + \mathrm{i}\omega\epsilon_0\epsilon\mathbf{E}_0. \tag{2.14}$$

We next take the dot product of $\mathbf{H}_0^*$ and $\mathbf{E}_0^*$ with the curls of $\delta\mathbf{E}$ and $\delta\mathbf{H}$, respectively and rewrite both making use of the vector identity

$$\mathbf{a}\cdot(\nabla\times\mathbf{b}) = \mathbf{b}\cdot(\nabla\times\mathbf{a}) - \nabla\cdot(\mathbf{a}\times\mathbf{b})\,. \tag{2.15}$$

Subtracting the obtained expressions gives us*

$$\begin{aligned}\delta\omega\,(\epsilon_0\epsilon\mathbf{E}_0^*\cdot\mathbf{E}_\mathrm{p} + \mu_0\mu\mathbf{H}_0^*\cdot\mathbf{H}_\mathrm{p}) = \\ -(\omega+\delta\omega)\left(\epsilon_0\Delta\epsilon\mathbf{E}_0^*\cdot\mathbf{E}_\mathrm{p} + \mu_0\Delta\mu\mathbf{H}_0^*\cdot\mathbf{H}_\mathrm{p}\right) \\ -(\omega-\omega^*)\left(\mu_0\mu\mathbf{H}_0^*\cdot\delta\mathbf{H} + \epsilon\epsilon_0\mathbf{E}_0^*\cdot\delta\mathbf{E}\right) \\ -\mathrm{i}\,(\nabla\cdot(\delta\mathbf{E}\times\mathbf{H}_0^*) + \nabla\cdot(\mathbf{E}_0^*\times\delta\mathbf{H}))\,.\end{aligned} \tag{2.16}$$

Finally, we take the integral of both sides over a (very large) volume V, and apply Gauss's theorem to arrive at the *Bethe-Schwinger equation*†:

$$\begin{aligned}\delta\omega\int_V dV\left[\epsilon_0\epsilon\mathbf{E}_0^*\cdot\mathbf{E}_\mathrm{p} + \mu_0\mu\mathbf{H}_0^*\cdot\mathbf{H}_\mathrm{p}\right] = \\ -(\omega+\delta\omega)\int_{\Delta V} dV\left[\epsilon_0\Delta\epsilon\mathbf{E}_0^*\cdot\mathbf{E}_\mathrm{p} + \mu_0\Delta\mu\mathbf{H}_0^*\cdot\mathbf{H}_\mathrm{p}\right] \\ -(\omega-\omega^*)\int_{\Delta V} dV\left[\mu_0\mu\mathbf{H}_0^*\cdot\delta\mathbf{H} + \epsilon\epsilon_0\mathbf{E}_0^*\cdot\delta\mathbf{E}\right] \\ -\mathrm{i}\int_{\partial V} dA\left[(\delta\mathbf{E}\times\mathbf{H}_0^*)\cdot\hat{\mathbf{n}} + (\mathbf{E}_0^*\times\delta\mathbf{H})\cdot\hat{\mathbf{n}}\right],\end{aligned} \tag{2.17}$$

where ∂V denotes the boundary of V and $\hat{\mathbf{n}}$ the unit vector normal to that surface.

To simplify eq. (2.17), that looks like a rather daunting expression to evaluate, we assume a high-Q cavity such that $\omega \approx \omega^*$. This results in

$$\begin{aligned}\delta\omega\int_V dV\left[\epsilon_0\epsilon\mathbf{E}_0^*\cdot\mathbf{E}_\mathrm{p} + \mu_0\mu\mathbf{H}_0^*\cdot\mathbf{H}_\mathrm{p}\right] = \\ -(\omega+\delta\omega)\int_{\Delta V} dV\left[\epsilon_0\Delta\epsilon\mathbf{E}_0^*\cdot\mathbf{E}_\mathrm{p} + \mu_0\Delta\mu\mathbf{H}_0^*\cdot\mathbf{H}_\mathrm{p}\right] \\ -\mathrm{i}\int_{\partial V} dA\left[\left(\delta\mathbf{E}\times\mathbf{H}_0^*\right)\cdot\hat{\mathbf{n}} + (\mathbf{E}_0^*\times\delta\mathbf{H})\cdot\hat{\mathbf{n}}\right].\end{aligned} \tag{2.18}$$

It is shown in appendix 2.B that for the high-Q cavities considered here, this is indeed a very good assumption. The above eq. (2.18) yields an expression

*In writing the third line like this we assumed $\epsilon \approx \epsilon^*$ and $\mu \approx \mu^*$. In any case, as we show in appendix 2.B, our (calculation) results do not significantly depend on this term.

†Due to the different (engineering) convention used in COMSOL, implementation of this formula requires to switch the sign in front of the surface integral from (−) to (+).

for the (complex) cavity shift

$$\delta\omega = \delta\omega_{\mathrm{c}} - \mathrm{i}\frac{\delta\kappa}{2}. \tag{2.19}$$

We continue by making the following approximations: If the effect of the perturbation is small, then $\omega + \delta\omega \approx \omega$, and when the total volume is large compared to the volume of the perturbation, it will be allowed to omit the contribution of $\mathbf{E}_0^* \cdot \delta\mathbf{E}$ in the integral on the left side of eq. (2.18), which can now be written as

$$\begin{aligned}\delta\omega \int_V dV \left[\epsilon_0\epsilon \mathbf{E}_0^* \cdot \mathbf{E}_{\mathrm{p}} + \mu_0\mu \mathbf{H}_0^* \cdot \mathbf{H}_{\mathrm{p}}\right] \approx \\ \delta\omega \int_V dV \left[\epsilon_0\epsilon \left|\mathbf{E}_0\right|^2 + \mu_0\mu \left|\mathbf{H}_0\right|^2\right] = 4\delta\omega U_0,\end{aligned} \tag{2.20}$$

where U_0 denotes the energy stored in the unperturbed cavity. Now the Bethe-Schwinger equation becomes

$$\begin{aligned}\delta\omega = -\frac{\omega}{4U_0} \int_{\Delta V} dV \left[\epsilon_0 \Delta\epsilon \mathbf{E}_0^* \cdot \mathbf{E}_{\mathrm{p}} + \mu_0 \Delta\mu \mathbf{H}_0^* \cdot \mathbf{H}_{\mathrm{p}}\right] \\ - \frac{\mathrm{i}}{4U_0} \int_{\partial V} dA \left[(\delta\mathbf{E} \times \mathbf{H}_0^*) \cdot \hat{\mathbf{n}} + (\mathbf{E}_0^* \times \delta\mathbf{H}) \cdot \hat{\mathbf{n}}\right].\end{aligned} \tag{2.21}$$

If the perturbation is caused by a variation of the permittivity ($\Delta\mu = 0$) and if the dimensions of its volume ΔV are small compared to the scale over which the cavity field $\mathbf{E}_0$ varies, one can make a useful approximation by considering the perturbation as a polarizable (point) dipole. Its total dipole moment $\mathbf{p}$ is given by

$$\mathbf{p} = \int_{\Delta V} \mathrm{d}V \frac{\mathrm{d}\mathbf{p}}{\mathrm{d}V}, \tag{2.22}$$

where we introduced the dipole moment per unit volume, which we identify as

$$\frac{\mathrm{d}\mathbf{p}}{\mathrm{d}V}(\mathbf{r}) = \epsilon_0 \left(\epsilon_{\mathrm{p}} - \epsilon\right) \mathbf{E}_{\mathrm{p}}(\mathbf{r}) = \epsilon_0 \Delta\epsilon \mathbf{E}_{\mathrm{p}}(\mathbf{r}). \tag{2.23}$$

Taking into account that $\mathbf{E}_0$ can be considered constant over ΔV, we can now write the integral over ΔV in eq. (2.21) as

$$\mathbf{E}_0^* \cdot \epsilon_0 \int_{\Delta V} \mathrm{d}V \Delta\epsilon \mathbf{E}_{\mathrm{p}} = \mathbf{E}_0^* \cdot \mathbf{p} = \mathbf{E}_0^* \cdot \overleftrightarrow{\alpha}\, \mathbf{E}_0, \tag{2.24}$$

where we have introduced the polarizability $\overleftrightarrow{\alpha}$ defined in this case through

$$\mathbf{p} = \overleftrightarrow{\alpha}\, \mathbf{E}_0. \tag{2.25}$$

If $\overleftrightarrow{\alpha}$ is diagonal, and we denote the magnitude of the polarizability in the direction of the cavity field by the scalar α, the integral over ΔV reduces to

$\alpha |\mathbf{E}_0|^2$. In this approach, we arrive at a new version of the Bethe-Schwinger equation for the perturbation of the cavity frequency:

$$\delta\omega = -\omega\frac{\alpha |\mathbf{E}_0|^2}{4U_0} - \frac{\mathrm{i}}{4U_0}\int_{\partial V} dA\,[(\delta\mathbf{E}\times\mathbf{H}_0^*)\cdot\hat{\mathbf{n}} + (\mathbf{E}_0^*\times\delta\mathbf{H})\cdot\hat{\mathbf{n}}]\,. \qquad (2.26)$$

This full expression, which is valid in any open, non-Hermitian system, contains an additional integral term involving radiated fields at a surface ∂V (with normal unit vector $\hat{\mathbf{n}}$), enclosing the same volume that was used to evaluate the total energy U_0. Since $\delta\mathbf{E}$ and $\delta\mathbf{H}$ are the difference between the eigenfields in the presence ($\mathbf{E}_\mathrm{p}$, $\mathbf{H}_\mathrm{p}$) and absence ($\mathbf{E}_0$, $\mathbf{H}_0$) of the perturbation, they can be associated with the field scattered by the perturbation. Thus, the cavity eigenfrequency is additionally modified by an energy flux that is evaluated by *combining* the fields of the perturbed and unperturbed eigenmodes; *i.e.*, an overlap of scattering by the perturbation and direct cavity radiation. The integral is independent of the distance at which δV is chosen, consistent with the fact that it can be associated with radiation of the system. Equation (2.26) shows how the real part of the particle's polarizability contributes to a frequency shift of the cavity, but so does the imaginary part of the surface integral. Likewise, the change of the cavity linewidth is related to the imaginary part of α and the real part of the integral over ∂V. To date, this far-field contribution has been omitted in practically all analyses of cavity perturbation. In a select number of experiments, a reduction of cavity linewidth was observed [23–26] and tentatively attributed to interference of radiation of the cavity and scattering by the perturbation. Importantly, the integral suggests that in principle also the resonance frequency (*i.e.*, the real part of $\delta\omega$) can be affected by the same mechanism, if the phase difference between cavity and scattered radiation in the far field (captured in $\mathbf{E}_0$ and $\delta\mathbf{E}$, respectively) differs from 0 or π. So far, the frequency has been expected to rely only on the local variation of the applied potential [3, 21, 25, 27–29] as it is contained in the first term of eq. (2.26).

2.5 Finite-element simulations

To verify the importance of radiation in a complete description of the induced cavity response, we perform finite-element method eigenfrequency studies (see appendix 2.B for details) with and without antenna in a two-dimensional system, displayed in fig. 2.6a, from which we extract the fields $\mathbf{E}_0$, $\mathbf{H}_0$, $\delta\mathbf{E}$ and $\delta\mathbf{H}$. This allows the calculation of the individual contributions to eq. (2.26), displayed as a function of detuning in fig. 2.6b (antenna on glass) and fig. 2.6c (antenna in air).[‡] As a benchmark, we first consider the situation with an

[‡]We note that in the simulations we evaluate the high-Q expression as shown in eq. (2.18). For simplicity, the text refers to the first and second term in eq. (2.26) as the 'resonant' and 'radiative' part.

antenna placed in air (fig. 2.6c). Here, the change in $\delta\omega$ is completely independent of the radiative contribution (green stars, second term in eq. (2.26)), such that total shift (blue circles) is entirely explained by the resonant contribution (black crosses, first term in eq. (2.26)), commensurate with the predicted shifts due to a resonant perturbation sketched in fig. 2.1c.

Considering the situation with glass substrate (fig. 2.6b), the first term in eq. (2.26) (black crosses, 'A') again contributes to $\delta\omega$ according to the expected behaviour for a perturbing resonator (fig. 2.1c): it produces a dispersive detuning dependence of $\delta\omega_c$ and a dissipative trend for $\delta\kappa$. However, this immediately disqualifies this term as an explanation for the experimentally measured changes in cavity resonance and linewidth. The second term, *i.e.* the contribution to the change in eigenfrequency related to the radiation interaction (green stars, 'B'), shows a dramatically different behavior: it causes distinct blueshifts and linewidth narrowing around $\Delta/\gamma = 0$. Surprisingly, the magnitude of the blueshifts induced by this term can even exceed the contribution due to α. This is a key point of our observation, stressing the importance of this new contribution in a model system. The sum of both terms (blue circles, A+B) yields the complete eigenfrequency shift of the perturbed cavity, which

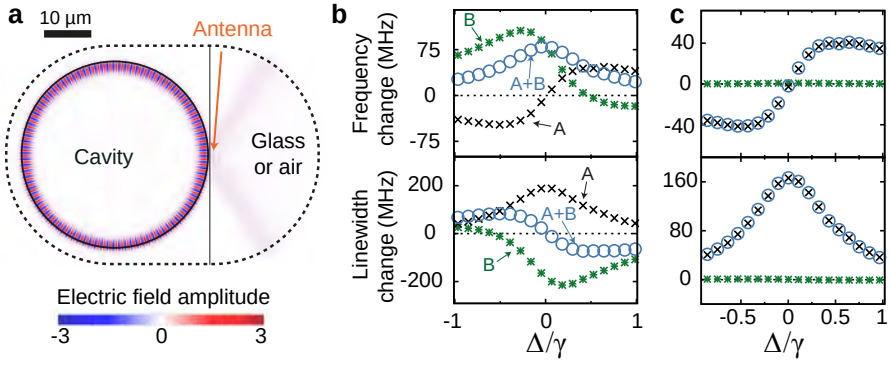

Figure 2.6: Finite-element simulations. **a**, Electric field profile as obtained from an eigenfrequency simulation containing cavity, antenna and substrate. Both antenna and cavity radiate into the glass under approximately the same angle, resulting in a radiation interaction. The contribution of this interaction is calculated on the dashed black line (integral of eq. (2.26)). The arrow points to the position of the antenna. **b**/**c**, Top(bottom): the change in resonance frequency(linewidth) calculated using eq. (2.26). Black crosses ('A') show the contribution of the polarizability to the eigenfrequency shift $\delta\omega$, which resembles the lineshape as we expect it from a resonant particle (fig. 2.1c). **b**, The radiative contribution (green stars, 'B') shows distinct blueshifts and linewidth narrowing near $\Delta/\gamma = 0$ when the antenna is placed on a glass substrate. Adding both terms (blue circles, 'A+B') yields the complete cavity eigenfrequency shift, which matches the observed experimental trends. **c**, In stark contrast, replacing the substrate with air results in a negligible radiative contribution, such that complex eigenfrequency shift is completely governed by the resonant contribution (black crosses).

now qualitatively matches our experimental results; blueshifts and linewidth narrowing around $\Delta/\gamma = 0$. Concluding, the calculations presented in this section thus confirm that radiation interactions in open systems can lead to both cavity blueshifts and linewidth narrowing and importantly, that this effect can even *dominate the total change in eigenfrequency* of a cavity mode.

2.6 Coupled-mode theory and the role of radiation

It is essential to realize that a modification of the cavity resonance frequency (in contrast to the alteration of the linewidth) due to backaction via the radiation continuum only occurs when the phase $\delta\phi$ between cavity and antenna radiation is different from 0 or π. The exact strength of this backaction, and as such the sum of direct (*i.e.* due to α) and indirect (*i.e.* via the radiation continuum) coupling between cavity and antenna, will depend on the overlap between their radiation profiles and on the value of $\delta\phi$ (fig. 2.7a). This phase difference and its physical connection to backaction can be captured in a simple model (fig. 2.7b) based on temporal coupled-mode theory [30, 31], essentially modelling the system as coupled harmonic oscillators with a Lorentzian response. While it is possible to treat the antenna as a harmonic oscillator without making the Lorentzian approximation, all essential physics is captured in the simpler Lorentzian model.

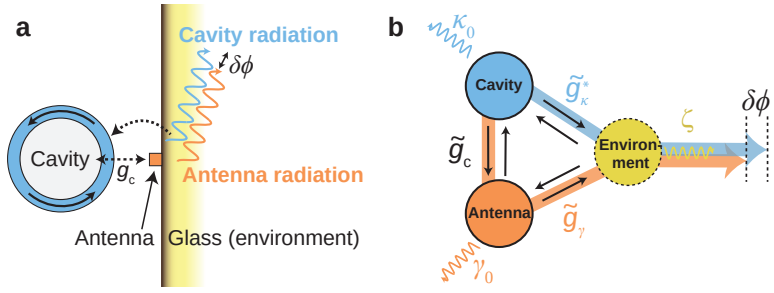

Figure 2.7: Coupling rates and relevant phases in the system. a, The cavity and antenna are coupled with rate g_c, which is the near-field interaction scaling with the polarizability of the antenna, and can radiate into the continuum with a certain delay ($\delta\phi$) with respect to each other. The interference between both radiation profiles and the overlap with the cavity mode results in a backaction effect (single-headed dashed arrow) on the cavity mode. **b**, Coupled-mode theory. The cavity and antenna are coupled with rate $\tilde{g}_c$ and couple to the continuum with complex rates $\tilde{g}_\kappa = g_\kappa\, e^{i\phi_\kappa}$ and $\tilde{g}_\gamma = g_\gamma\, e^{i\phi_\gamma}$ respectively. The difference between ϕ_κ and ϕ_γ, summed with the phase response of the antenna, is now equal to the phase difference $\delta\phi$. κ_0 and γ_0 are the losses of cavity and antenna into non-coupled channels. The environment is modeled as an oscillator with decay rate ζ.

We treat the decay in a common (overlapping) radiation continuum, and its possible backaction on both antenna and cavity, by considering the 'environment' as a third mode coupled to both antenna and cavity as well as to an independent decay port. The complex mode amplitudes of cavity (a), antenna (b) and environment (c) are normalized such that their magnitude squared equals the energy in each degree of freedom. They are collected in vector $\mathbf{a} = (a, b, c)^{\mathrm{T}}$. In absence of driving fields, the three-resonator coupled system is described in the Fourier domain (section 1.3) by

$$(M + \omega I)\mathbf{a} = \begin{pmatrix} \omega - \omega_{\mathrm{c}} + \mathrm{i}\kappa_0/2 & \tilde{g}_{\mathrm{c}}^* & \tilde{g}_\kappa \\ \tilde{g}_{\mathrm{c}} & \omega - \omega_0 + \mathrm{i}\gamma_0/2 & \tilde{g}_\gamma^* \\ \tilde{g}_\kappa^* & \tilde{g}_\gamma & \omega - \omega_{\mathrm{e}} + \mathrm{i}\zeta/2 \end{pmatrix} \mathbf{a} = \mathbf{0}. \tag{2.27}$$

The off-diagonal coupling rates can in general be complex[§], and we will write them later as $\tilde{g}_j = g_j e^{\mathrm{i}\phi_j}$ with real g_j and ϕ_j. The diagonal contains damping rates κ_0, γ_0 and ζ that are associated with decay into different independent output channels. As such, the output fields $\mathbf{s} = (s_{\mathrm{a}}, s_{\mathrm{b}}, s_{\mathrm{c}})^{\mathrm{T}}$ in these ports can be written as $\mathbf{s} = D\mathbf{a}$, where

$$D = \begin{pmatrix} \sqrt{\kappa_0} & 0 & 0 \\ 0 & \sqrt{\gamma_0} & 0 \\ 0 & 0 & \sqrt{\zeta} \end{pmatrix}. \tag{2.28}$$

We now introduce the detunings $\Delta_{\mathrm{c}} = \omega - \omega_{\mathrm{c}}$, $\Delta = \omega_{\mathrm{c}} - \omega_0$ and $\Delta_{\mathrm{e}} = \omega_{\mathrm{c}} - \omega_{\mathrm{e}}$, such that

$$(M + \omega I) = \begin{pmatrix} \Delta_{\mathrm{c}} + \mathrm{i}\kappa_0/2 & \tilde{g}_{\mathrm{c}}^* & \tilde{g}_\kappa \\ \tilde{g}_{\mathrm{c}} & \Delta_{\mathrm{c}} + \Delta + \mathrm{i}\gamma_0/2 & \tilde{g}_\gamma^* \\ \tilde{g}_\kappa^* & \tilde{g}_\gamma & \Delta_{\mathrm{c}} + \Delta_{\mathrm{e}} + \mathrm{i}\zeta/2 \end{pmatrix}. \tag{2.29}$$

The eigenmodes can be found by solving the system $(M + \omega I)\mathbf{a} = \mathbf{0}$. Since we assume the cavity and antenna are weakly coupled and we are only interested in the perturbed cavity mode, we can neglect Δ_{c} in the second and third row of eq. (2.29). The solution is

$$\Delta_{\mathrm{c}} = \frac{g_\kappa^2 \left(\Delta + \mathrm{i}\frac{\gamma_0}{2}\right) + g_{\mathrm{c}}^2 \left(\Delta_{\mathrm{e}} + \mathrm{i}\frac{\zeta}{2}\right) - 2 g_{\mathrm{c}} g_\kappa g_\gamma \cos\Phi}{\left(\Delta + \mathrm{i}\frac{\gamma_0}{2}\right)\left(\Delta_{\mathrm{e}} + \mathrm{i}\frac{\zeta}{2}\right) - g_\gamma^2} - \mathrm{i}\kappa_0, \tag{2.30}$$

where we have introduced $\Phi = \phi_{\mathrm{c}} + \phi_\kappa + \phi_\gamma$.

It is instructive to consider the case where the cavity mode is absent ($a = 0, g_{\mathrm{c}} = g_\kappa = 0$). In that case, the power radiated via the environment into port s_{c} is equal to $\zeta g_\gamma^2 |b|^2 / (\Delta_{\mathrm{e}}^2 + \zeta^2/4)$. We therefore define the rate

$$\gamma_1 \equiv \frac{\zeta g_\gamma^2}{\Delta_{\mathrm{e}}^2 + \zeta^2/4}, \tag{2.31}$$

[§]Note that we have not enforced the relation $K = D^{\mathrm{T}}$ (section 1.3), such that there still exists a gauge freedom in choosing the phase of the coupling rates and $\mathbf{a}$.

which is the rate at which the antenna decays into the common radiation continuum if the cavity were not there. Likewise, we consider the case without the antenna ($b = 0, g_c = g_\gamma = 0$), and define

$$\kappa_1 \equiv \frac{\zeta g_\kappa^2}{\Delta_e^2 + \zeta^2/4}, \tag{2.32}$$

which is the rate at which the cavity would decay into this channel in absence of the antenna. In the latter case, the eigenmode would have detuning

$$\Delta_c^{(b=0)} = \frac{\Delta_e}{\zeta}\kappa_1 - i\frac{\kappa}{2}, \tag{2.33}$$

where $\kappa = \kappa_0 + \kappa_1$ is the *total* decay rate of the cavity without the antenna. We now specifically write the general solution as $\Delta_c = \Delta_c^{(b=0)} + \delta\Delta_c$, such that $\delta\Delta_c$ is the *change* of the eigenmode frequency due to the presence of the antenna and $\delta\Delta_c = \delta\omega_c - i\delta\kappa/2$. Taking the limit of ζ to infinity, which effectively amounts to setting $\Delta_e = 0$, it reads

$$\delta\omega_c - i\delta\kappa/2 = \frac{g_c^2 - \kappa_1\gamma_1/4 + ig_c\sqrt{\kappa_1\gamma_1}\cos\Phi}{\Delta + i\gamma/2}, \tag{2.34}$$

which depends on the radiation overlap $\kappa_1\gamma_1$, (constant) phase Φ and the coupling rate g_c. Because the overlap and phase Φ cannot be independently chosen, it is impossible to directly fit eq. (2.34) to the experimental data in fig. 2.5. Instead, we will retrieve the phase $\delta\phi$ as it appears in the Bethe-Schwinger equation from the finite element simulation, and subsequently obtain Φ using a relation that connects $\delta\phi$ and Φ.

To obtain such a connection, we start by expressing the field in the environment c relative to the field in the cavity a. Its full expression (still taking $\Delta_e = 0$) is

$$\frac{c}{a} = \frac{2ie^{-i\phi_\kappa}}{\zeta}\frac{g_\kappa\left(\Delta + i\frac{\gamma_0}{2}\right) - g_c g_\gamma e^{i\Phi}}{\Delta + i\frac{\gamma}{2}}. \tag{2.35}$$

The phase difference $\delta\phi$ between cavity radiation (blue path, fig. 2.7b) and antenna scattering (orange path, fig. 2.7b) in this model is obtained by calculating the phase of eq. (2.35) in absence of the particle ($g_c = g_\gamma = 0$), and its phase in absence of direct coupling between cavity and environment ($g_\kappa = 0$). The resulting phase difference is equivalent to $\delta\phi$ and reads

$$\delta\phi = \pi + \Phi - \arg\left(\Delta + i\frac{\gamma}{2}\right), \tag{2.36}$$

showing that the phase difference of the two decay paths is directly related to the (relative) phases of the coupling rates via Φ and the phase response of the antenna. Note that the more common scenario where the two paths interfere destructively on resonance ($\Delta = 0$), occurs for $\Phi = \pi/2$, such that $\delta\phi = \pi$.

Importantly however, from the finite-element simulations we obtain $\Phi = 3.76 \times 10^{-4}\pi$. Using eq. (2.36), this value of Φ directly yields $\delta\phi \approx \pi/2$ at $\Delta = 0$, completely opposite to the conventionally assumed case where destructive interference ($\delta\phi = \pi$) only contributes to the linewidth of the cavity mode. Fixing Φ at this value and constraining the experimentally found values of κ, Δ and γ (retrieved from independent spectroscopic measurements, fig. 2.2), a fit of eq. (2.34) yields excellent correspondence to our data in fig. 2.5b (solid lines), with fitted values of $\kappa_1\gamma_1/\kappa\gamma = 0.68$ and coupling rate $g_c/2\pi = 21.6$ GHz.

To conclude this section, we note that it is straightforward to eliminate the environment mode c from the model to construct an equivalent system of equations $M'(a, b)^{\mathrm{T}} = \mathbf{0}$. In that case the total damping rates κ and γ of the uncoupled cavity and antenna appear on the diagonal:

$$M' = \begin{pmatrix} \Delta_c + \mathrm{i}\frac{\kappa}{2} & e^{-\mathrm{i}\phi_c}\left(g_c + \frac{\mathrm{i}}{2}\sqrt{\kappa_1\gamma_1}e^{\mathrm{i}\Phi}\right) \\ e^{\mathrm{i}\phi_c}\left(g_c + \frac{\mathrm{i}}{2}\sqrt{\kappa_1\gamma_1}e^{-\mathrm{i}\Phi}\right) & \Delta + \mathrm{i}\frac{\gamma}{2} \end{pmatrix}. \tag{2.37}$$

We can choose the phase $\phi_c = 0$ without loss of generality, such that

$$M' = \begin{pmatrix} \Delta_c + \mathrm{i}\frac{\kappa}{2} & g_c + \frac{\mathrm{i}}{2}\sqrt{\kappa_1\gamma_1}e^{\mathrm{i}\Phi} \\ g_c + \frac{\mathrm{i}}{2}\sqrt{\kappa_1\gamma_1}e^{-\mathrm{i}\Phi} & \Delta + \mathrm{i}\frac{\gamma}{2} \end{pmatrix}. \tag{2.38}$$

Note that the off-diagonal matrix elements of M', representing coupling between cavity and antenna, are now no longer each others conjugate, such that M' is non-Hermitian even in its off-diagonal elements.

2.7 Conclusion

Concluding, we have shown how coupling through the radiation continuum leads to cavity blueshifts and linewidth narrowing in a coupled cavity-antenna system. Surprisingly, the non-local, radiative effect on the cavity is larger than the induced cavity response due to local perturbations, and is not just an artefact of large radiation losses but can even manifest itself in a high-Q cavity such as studied here. Therefore, similar effects are expected in many other systems where cavity and perturbation can radiate into the same channels, such as photonic crystals [23–25, 32] and Fabry-Pérot etalons [33–35]. In addition, it was shown that there is a direct link between the phase $\delta\phi$ in the Bethe-Schwinger equation and the contributions to backaction in a coupled-mode model.

Interestingly, these results could also shed new light on radiative interactions in strongly radiating systems such as metamaterials and complex plasmonic resonators. In [17], it was postulated that radiation can be included in the coupling between two resonators by using a complex coupling rate, while in [36], a complex coupling rate was argued to originate from a complex-valued extinction

cross-section. In fact, such a complex coupling rate between two resonators was derived from the coupled-mode model presented in this work. Furthermore, it will be interesting to see how the concepts and theory established here relate to recently developed methods relying on the normalization of quasi-normal modes to describe the response of complex (radiating) photonic systems [37–40], where one relies on a renormalization of the complex eigenmodes. In a different context, recent advances in optomechanics using simultaneous dispersive and dissipative (*i.e.* radiative) coupling [41–43] have been reported to enable on-resonance cooling [41] and sensitive readout of nanomechanical motion [42]. As such, we expect our work to be directly important to the design of novel optical devices such as sensors, for example, and benefit the understanding of the physics of open systems in optics and beyond.

Appendices

2.A Experimental details

2.A.1 Sample fabrication

Gold nanoantennas are fabricated in arrays on a 170 µm thick glass coverslide. To start, a 130 nm layer of ZEP-520 resist is spin-coated on top of the coverslide. The nanoantennas are patterned into the resist using electron-beam lithography. After development, thermal evaporation of gold and a lift-off step yield the desired antennas. The antenna width and thickness were designed to be 120 and 40 nm and the length was varied between 400 and 360 nm. The pitch along the short axes of the antennas was varied between 750 and 1500 nm, and the pitch along the long axes was fixed at 800 nm. A high-Q silica microtoroid (diameter $\approx$ 36 µm) is fabricated on the edge of a silicon sample, largely following methods as previously reported [19, 20]. In this work, spin-coating (ma-N 2410) and subsequent cleaving of the sample enabled targeted e-beam lithography of the disks near the edge of the sample.

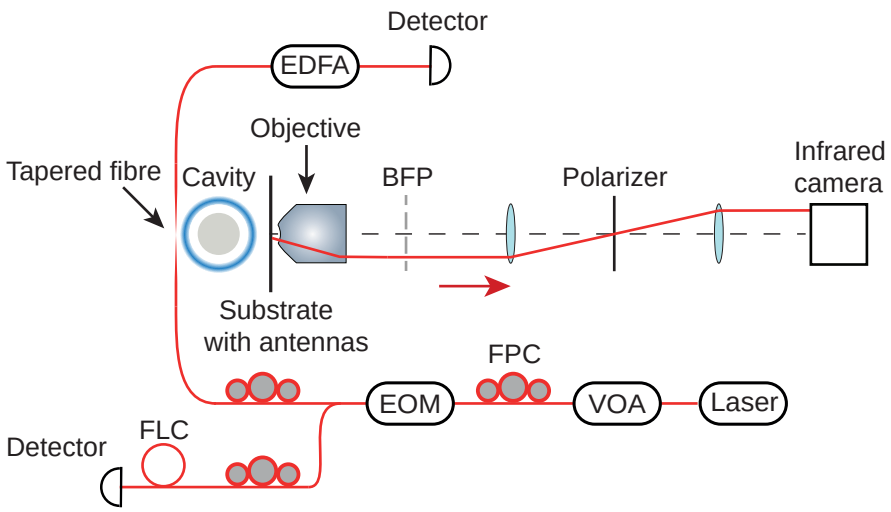

Figure 2.8: Experimental setup. Full details can be found in the text. Here we list the abbreviations. BFP: Back-Focal-Plane, EDFA: Erbium Doped Fibre Amplifier, FLC: Fibre Loop Cavity, EOM: Electro-Optic Modulator, FPC: Fibre Polarization Controller, VOA: Variable Optical Attenuator.

2.A.2 Experimental Setup

Figure 2.8 shows the experimental setup employed in this work. We use a tunable fibre-coupled external cavity diode laser (New Focus TLB-6728, <100 kHz linewidth) to probe the microcavity. The laser frequency is controlled by an external voltage from a function generator. Coupling of light into the cavity is achieved using a tapered optical fibre, of which the position is controlled using piezo positioners (not shown). The electro-optic modulator (EOM, EOspace) is used to generate sidebands of the cavity mode at known RF frequency, which allows for calibration of our optical frequency axis. Fibre polarization controllers (FPC) ensure effective coupling into the optical cavity mode of interest. Before detection, the light that is transmitted through the tapered fibre is amplified using an Erbium Doped Fibre Amplifier (EDFA). Radiation leakage from the microcavity is collected using an objective (Nikon, CFI Apo TIRF 100x) to obtain information regarding polarization and mode profile (through Fourier-space imaging and polarization analysis of the back focal plane (BFP) of the cavity mode. Using this method we identify a fundamental cavity mode, of which the polarization is aligned with the long axes of the antennas (for more details see fig. 3.4c-e). Due to limitations with regards to the numerical aperture (NA) of our objective (NA $\approx$ 1.33 at the operation wavelength), imaging of the complete cavity mode-profile is difficult. Considering this cut-off at NA=1.33 and the refractive index of silica (1.46), we estimate an effective mode index of around 1.35. We check the frequency stability of the laser itself using a fibre loop reference cavity (FLC).

2.A.3 Varying antenna pitch

Section 2.3 shows the results and analysis of antenna arrays with pitch 800(1500) nm along the long(short) axis of the antennas. More pitches are, however, experimentally investigated and fig. 2.9 shows the main results which we obtain when varying the pitch along the short axis (750-1500 nm) of the antennas, while the pitch along the antenna long axis is kept constant at 800 nm. In this figure, the points which are surrounded by a dashed circle correspond to the arrays used to generate fig. 2.5a. The main conclusion that can be drawn from fig. 2.9 is that, qualitatively, the different arrays behave the same: all arrays induce blueshifts of the cavity resonance frequency (top panel) and linewidth narrowing (bottom panel) of the cavity on approaching $\Delta/\gamma = 0$. With changing pitch, the value of Δ/γ where the 'relative linewidth change' equals 0, slightly varies. We attribute this effect to the influence of the array on the single-particle polarizability. Remarkably, for the largest possible detuning we measure linewidth narrowing up to 30% for a pitch of 1100 nm. The values of Δ/γ are retrieved from a fit of the normal-incidence transmission spectra using a Lorentzian lineshape.

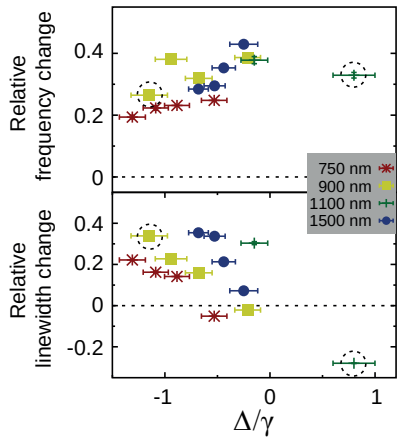

Figure 2.9: Varying the antenna array pitch. Changing the pitch along the antenna short axis (between 750 and 1500 nm) does not greatly affect the cavity eigenfrequency shift. For all arrays, we observe cavity blueshifts (top panel) and linewidth narrowing (bottom panel). Note that in the bottom panel, the different pitches cross the point of zero linewidth change at slightly different values of Δ/γ. Modification of the single particle polarizability due to the array is the most likely cause of this behaviour. The values on the vertical axis are corrected for the unit-cell area and the points which are surrounded by a dashed circle correspond to the arrays used to generate fig. 2.5a. Errors on the mean (vertical axis) fall mostly within the plot markers and the error on the horizontal axis is one standard deviation, retrieved from a Gaussian fit to the sum of squared residuals (obtained by displacing the fit result). Due to limited detector range, a reliable horizontal error for the data at P1100,$\Delta/\gamma \approx 0.8$ could not be obtained using this method. The error on this data point was thus set equal to the error for array P1100,$\Delta/\gamma \approx -0.15$.

2.A.4 Validation of detuning

We verify that the resonance frequency ω_c of the cavity is also red-detuned to the broadband antenna resonances for large incident wavevector, and not only for normal incidence. To this end, we perform total internal reflection measurements on the samples with a 1500 nm pitch using an incident wavevector that approximately matches that of the cavity mode. The resulting reflectance data (see fig. 3.2c for experimental details), which is normalized to the reflectance of glass for this particular incident wavevector, is displayed in fig. 2.10b. In this figure, the horizontal axis corresponds to the entire wavelength range of the tunable laser (1570-1520 nm), which in itself however maps only a small part of the broadband antenna resonances, which are displayed as cartoons in fig. 2.10a. The slopes of the plots in fig. 2.10b clearly indicate that for all four arrays, the cavity mode is red-detuned with respect to the broadband antenna resonance. We thus conclude that a strong antenna resonance shift is absent, and that the blueshifts and linewidth narrowing observed in the experiment (fig. 2.5b) do not result from an unexpected sign flip in the detuning Δ.

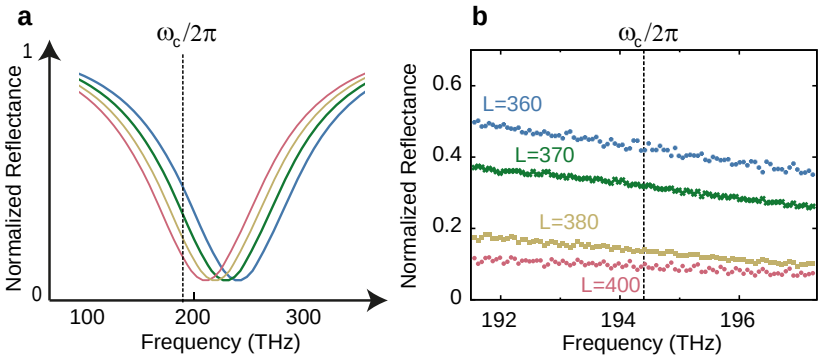

Figure 2.10: Antenna response with large angle of incidence. **a**, Schematic broadband response of four antenna arrays. The smallest antennas (blue sold line) exhibit the highest resonance frequency. The cavity resonance frequency is indicated by a dashed line. **b**, Measured reflectance for different antenna lengths. The shorter antennas exhibit a higher resonance frequency, which is reflected in a higher reflectance at ω_c. Based on the slopes we conclude that also for large incident wavevector the cavity mode is red-detuned with respect to the antenna resonances.

2.B Finite-element simulations: tricks of the trade

To gain more insight in our experimental results, and to calculate the different contributions to the complex frequency shift $\delta\omega$, we perform 2D eigenfrequency simulations using the COMSOL software package (v5.0). The cavity (diameter = 36 µm) has a refractive index of 1.35, comparable to the experimentally estimated effective index of our cavity mode and is placed 1.1 µm from the substrate, which has a refractive index of 1.5. The antenna is assigned a varying permittivity to mimic a change in detuning between cavity and antenna and for the surrounding we take a refractive index of 1. The simulation includes the use of a Perfectly Matched Layer (PML).

In our experiment, changing the length of the antennas results in a changing plasmon resonance, in turn causing a varying detuning between cavity and antenna resonance frequency. To mimic this in our simulation, we assign a tunable permitivitty, which has a Lorentzian lineshape, to the perturbing antenna(s):

$$\epsilon_p = 1 - \frac{S * \gamma_s/2}{\Delta_s - i\gamma_s/2} \tag{2.39}$$

Sweeping the variable Δ_s now allows to calculate the change in cavity eigenfrequency as a function of detuning. The parameter S can be used to control the scattering strength of the antenna, while the antenna linewidth is held fixed at $\gamma_s = 1$. To determine a sensible value of S, we analyze the eigenfrequency shift of the cavity when perturbed by 11 antennas (pitch 1500, fig. 2.11a) for different

values of S and choose a value ($S = 340$) which yields the best resemblance to our experiment (fig. 2.11b). The values for the relative change in linewidth and resonance frequency are obtained via similar analysis as performed in the experimental situation, thus involving separate simulations for the bare cavity, and cavity perturbed by just a glass substrate.

Note that the values Δ_s and γ_s are input parameters in the simulation, which do not include the effect of radiation losses on the antenna linewidth and resonance frequency [21]. To allow for a fair comparison with our experiment, we fit the results retrieved from the simulation with a Fano lineshape (black lines in fig. 2.11a), to obtain the radiation corrected values Δ and γ. Using these corrected values of Δ and γ, we rescale our horizontal axis and obtain fig. 2.11b. Note that this approach resembles the experimental situation, where the radiation corrected values of Δ and γ are retrieved from the normal-incidence transmission spectra. It can be observed from fig. 2.11b that the orange (resonance frequency) and pink (linewidth) circles are a good, but not perfect, match to the experimentally obtained cavity frequency and linewidth change (blue circles). We attribute the discrepancy to the intrinsic difference between a 2D simulation, where the cavity is modelled as an infinite cylinder, and the experimental situation, which employs a toroidal cavity. This will necessarily change the radiation profile determining overlap and phase. Nonetheless, the 2D simulation reproduces all the main features observed in the experiment.

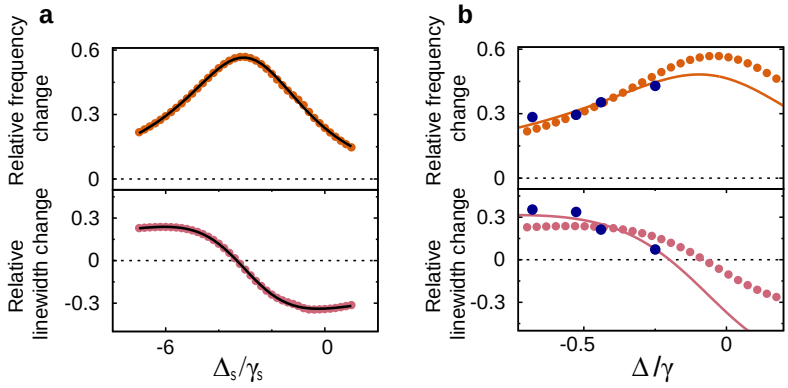

Figure 2.11: Using multiple scatterers to find the scattering strength S. **a**, Filled circles: change in resonance frequency (top) and linewidth (bottom) of the cavity when perturbed by 11 antennas. The values on the horizontal axis are the input parameters in the simulation, which do not include effects due to radiation losses. Using a fit (black line) with a Fano-lineshape gives access to rescaled values of Δ and γ, which are used in **b**. **b**, The blue circles and solid lines are experimental data points and a fit using the coupled-mode model, respectively. The orange (top) and pink (bottom) filled circles are the relative frequency and linewidth change that are obtained from a simulation with $S = 340$.

Cavity and perturbation without glass

When calculating the complete Bethe-Schwinger formula, it is useful to first consider the situation where a cavity is perturbed by a single perturbing particle, in the absence of a substrate, as this should not allow for radiation interaction taking place, and thus result in a perturbation of the cavity eigenfrequency which is solely governed by the polarizability of the perturbing particle. The results of this simulation are shown in fig. 2.12a. It is clear that the cavity indeed lacks radiation interaction (green stars) with the antenna and experiences linewidth and resonance frequency shifts that are solely related to the polarizability of the particle (black crosses), such that the total eigenfrequency change (open blue circles) is completely dominated by local effects. In addition, the black squares depict the contribution of the term that scales with $(\omega - \omega^*)$ in eq. (2.17). Judging from the negligible contribution of this term its omission, which allows us to simplify eq. (2.17) to eq. (2.18), seems valid. We remark that the Bethe-Schwinger cavity perturbation formula, which needs fields as it input, perfectly reproduces the cavity eigenfrequency shifts as predicted by the eigenvalues (orange(pink) filled circles) directly obtained from COMSOL.

Cavity and perturbation with glass

Introducing a glass substrate enables an extra coupling channel between antenna and cavity due to overlapping radiation profiles. Figure 2.12b shows results quantifying this effect for a cavity perturbed by a single antenna. Here the radiative interactions (green stars) are of importance when calculating the total (open blue circles) eigenfrequency shift of the cavity using the Bethe-Schwinger equation, dominating the effect of local perturbation (black crosses). Again we note the small contribution (black squares) of the term that scales with $(\omega - \omega^*)$ in eq. (2.17), validating its omission in the further theoretical approximations made in section 2.4.1. The calculation of complex $\delta\omega$ using the full Bethe-Schwinger equation yields almost exactly the same results when compared to the cavity eigenfrequency changes based on the eigenvalues calculated in the simulation (orange(frequency) and pink(linewidth) filled circles). We attribute the small difference that is observed mostly to the way joined data sets are handled in COMSOL. The use of joined datasets is necessary to obtain the fields $\delta\mathbf{E}$, but causes an error when integrating the closed-surface flux integrals (last terms of eq. (2.26)). The reason is that for joined datasets COMSOL projects full datasets on a less dense intermediate mesh[¶]. We performed mesh convergence studies to see if this effect would diminish with increasing mesh density (up to 60 elements/λ_0). Although we observe that the eigenvalues and fields of our solutions are converged, the small difference in the cavity eigenfrequency shift that we obtain does not disappear. Nonetheless, the discrepancy is small enough to reproduce all observed trends.

[¶]COMSOL personal communication

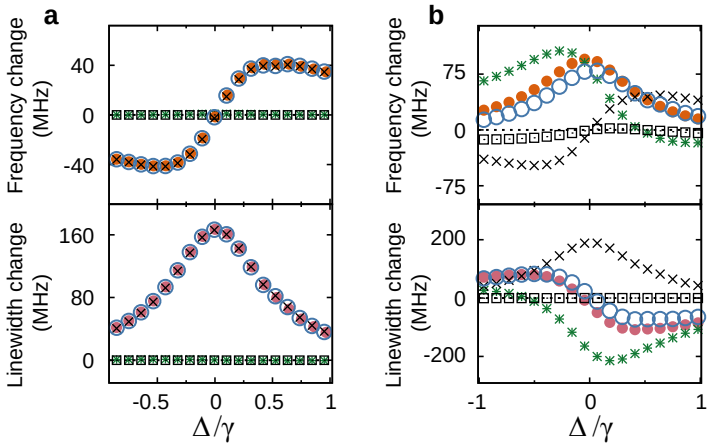

Figure 2.12: Benchmarking the calculation. **a**, In the absence of a substrate, the cavity experiences a change in resonance frequency (top) and linewidth (bottom) that is solely associated with the polarizability (black crosses) of the perturbing particle, such that that the total eigenfrequency change as calculated by the Bethe-Schwinger equation (open blue circles) is completely dominated by local effects, leaving the radiative interaction (green stars) to be negligible. As expected, the Bethe-Schwinger cavity perturbation formula is able to perfectly reproduce the cavity eigenfrequency shifts when compared to the shifts obtained using the eigenvalues (orange(pink) filled circles) calculated by COMSOL **b**, In the situation where the substrate is present, as discussed before, radiative interactions (green stars) are of importance when calculating the total (open blue circles) eigenfrequency shift of the cavity using the Bethe-Schwinger equation, dominating the local effect of the perturbation (black crosses). Note that the calculation of the full Bethe-Schwinger equation yields almost perfect overlap with the cavity eigenfrequency changes as calculated by COMSOL (orange and pink filled circles), which are based on the eigenvalues of the solutions. We attribute the small difference that is observed mostly to the way joined data sets are handled in COMSOL, which involves projection on an intermediate mesh. This is known to cause loss of information and introduces a small error when integrating radiation patterns. **a**/**b**, the black squares depict the negligible contribution of the term that scales with $(\omega - \omega^*)$ in eq. (2.17).

Subtracting fields

Figure 2.6a shows the field profile $\mathbf{E}_\mathrm{p}$ of a cavity perturbed by an antenna on a glass substrate. To increase the visibility of the radiation pattern, that figure and fig. 2.13 show the field amplitude for a cavity placed 0.3 µm from the substrate and antenna. To calculate the full cavity perturbation formula, it is necessary to find the unperturbed cavity field profile (fig. 2.13a, $\mathbf{E}_0$) and subtract this from $\mathbf{E}_\mathrm{p}$ in order to obtain the field $\delta\mathbf{E}$ (fig. 2.13b). The teal line surrounding the field profiles represents a perfectly matched layer (PML), which is used in all calculations discussed in this paper, while the dashed black line is the boundary which we used for the calculation of the surface integral of eq. (2.26).

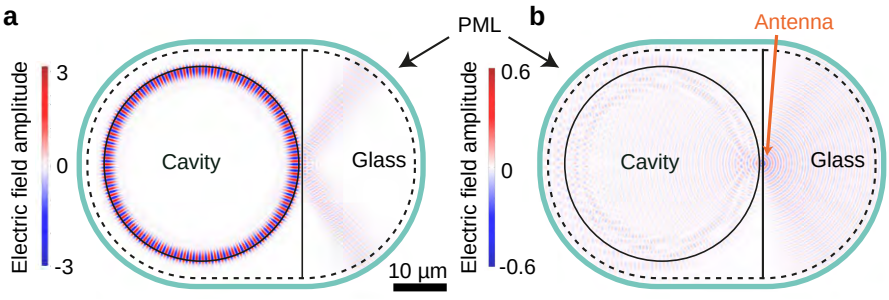

Figure 2.13: Simulated field profiles. **a**, The simulated field profile $\mathbf{E}_0$ for a cavity in the absence of perturbing particles. **b**, The field profile $\delta\mathbf{E}$ of the perturbing antenna. This profile is obtained by subtracting the fields in **a** from those shown in fig. 2.6a. In both **a** and **b**, the teal line surrounding the field profiles represents a perfectly matched layer (PML).

A pitfall in subtracting fields from different eigenfrequency simulations lies in the arbitrary choice of amplitude and phase of the solutions. To overcome this problem, we monitor the amplitude and phase in both simulations (with and without antenna) in a point where modification of the field profile due to the perturbing antenna is expected to be negligible. This can be, for example, a point in the field maximum of the cavity mode far away from the perturbation, thus allowing to correct for possible differences in amplitude and phase between the calculations. To obtain the data in fig. 2.6b/c, a single phase correction was performed, to match the phase at $\Delta_s = -3$ to the unperturbed phase, in a mode maximum at large distance from the perturbing particle.

References

[1] J. M. Raimond, M. Brune, and S. Haroche, *Manipulating quantum entanglement with atoms and photons in a cavity*, Rev. Mod. Phys. **73**, 565 (2001).

[2] P. Lodahl, S. Mahmoodian, and S. Stobbe, *Interfacing single photons and single quantum dots with photonic nanostructures*, Rev. Mod. Phys. **87**, 347 (2015).

[3] F. Vollmer, and S. Arnold, *Whispering-gallery-mode biosensing: label-free detection down to single molecules*, Nat. Methods **5**, 591 (2008).

[4] X. Fan, et al., *Sensitive optical biosensors for unlabeled targets: a review.*, Anal. Chim. Acta **620**, 8 (2008).

[5] M. Aspelmeyer, T. J. Kippenberg, and F. Marquardt, *Cavity optomechanics*, Rev. Mod. Phys. **86**, 1391 (2014).

[6] J. Zhu, et al., *Single nanoparticle detection by mode splitting in ultra-high-Q microtoroid*, Nat. Photonics **4**, 46 (2010).

[7] J. D. Thompson, et al., *Coupling a single trapped atom to a nanoscale optical cavity*, Science **340**, 1202 (2013).

[8] A. Goban, et al., *Atom-light interactions in photonic crystals*, Nat. Commun. **5**, 3808 (2014).

[9] R. A. Waldron, *Perturbation theory of resonant cavities*, Proc. IEE Part C Monogr. **107**, 272 (1960).

[10] H. A. Bethe, and J. Schwinger, *Perturbation theory for cavities* (Massachusetts Institute of Technology, Radiation Laboratory, Cambridge, 1943).

[11] H. Friedrich, and D. Wintgen, *Interfering resonances and bound states in the continuum*, Phys. Rev. A **32**, 3231 (1985).

[12] Y. Plotnik, et al., *Experimental observation of optical bound states in the continuum*, Phys. Rev. Lett. **107**, 183901 (2011).

[13] C. W. Hsu, et al., *Observation of trapped light within the radiation continuum*, Nature **499**, 188 (2013).

[14] F. Monticone, and A. Alù, *Embedded photonic eigenvalues in 3D nanostructures*, Phys. Rev. Lett. **112**, 213903 (2014).

[15] C. W. Hsu, B. Zhen, A. D. Stone, J. D. Joannopoulos, and M. Soljačić, *Bound states in the continuum*, Nat. Rev. Mater. **1**, 16048 (2016).

[16] A. Kodigala, et al., *Lasing action from photonic bound states in continuum*, Nature **541**, 196 (2017).

[17] R. Taubert, M. Hentschel, J. Kästel, and H. Giessen, *Classical analog of electromagnetically induced absorption in plasmonics*, Nano Lett. **12**, 1367 (2012).

[18] N. Liu, et al., *Plasmonic analogue of electromagnetically induced transparency at the Drude damping limit.*, Nat. Mater. **8**, 758 (2009).

[19] D. K. Armani, T. J. Kippenberg, S. M. Spillane, and K. J. Vahala, *Ultra-high-Q toroid microcavity on a chip*, Nature **421**, 925 (2003).

[20] G. Anetsberger, et al., *Near-field cavity optomechanics with nanomechanical oscillators*, Nat. Phys. **5**, 909 (2009).

[21] L. Novotny, and B. Hecht, *Principles of nano-optics* (Cambridge University Press, Cambridge, 2012), 2nd ed.

[22] A. Mazzei, et al., *Controlled coupling of counterpropagating whispering-gallery modes by a single Rayleigh scatterer: A classical problem in a quantum optical light*, Phys. Rev. Lett. **99**, 173603 (2007).

[23] A. F. Koenderink, M. Kafesaki, B. C. Buchler, and V. Sandoghdar, *Controlling the resonance of a photonic crystal microcavity by a near-field probe*, Phys. Rev. Lett. **95**, 153904 (2005).

[24] J. T. Robinson, and M. Lipson, *Far-field control of radiation from an individual optical nanocavity: Analogue to an optical dipole*, Phys. Rev. Lett. **100**, 043902 (2008).

[25] M. Burresi, et al., *Magnetic light-matter interactions in a photonic crystal nanocavity*, Phys. Rev. Lett. **105**, 123901 (2010).

[26] N. Le Thomas, and R. Houdré, *Inhibited emission of electromagnetic modes confined in subwavelength cavities*, Phys. Rev. B **84**, 035320 (2011).

[27] S. Vignolini, et al., *Magnetic imaging in photonic crystal microcavities*, Phys. Rev. Lett. **105**, 123902 (2010).

[28] L. Lalouat, et al., *Near-field interactions between a subwavelength tip and a small-volume photonic-crystal nanocavity*, Phys. Rev. B **76**, 041102 (2007).

[29] S. Arnold, M. Khoshsima, I. Teraoka, S. Holler, and F. Vollmer, *Shift of whispering-gallery modes in microspheres by protein adsorption.*, Opt. Lett. **28**, 272 (2003).

[30] H. A. Haus, *Waves and fields in optoelectronics* (Prentice-Hall, 1984).

[31] W. Suh, Z. Wang, and S. Fan, *Temporal coupled-mode theory and the presence of non-orthogonal modes in lossless multimode cavities*, IEEE J. Quantum Electron. **40**, 1511 (2004).

[32] M. Barth, et al., *Nanoassembled plasmonic-photonic hybrid cavity for tailored light-matter coupling*, Nano Lett. **10**, 891 (2010).

[33] A. Mitra, H. Harutyunyan, S. Palomba, and L. Novotny, *Tuning the cavity modes of a Fabry–Perot resonator using gold nanoparticles*, Opt. Lett. **35**, 953 (2010).

[34] D. Chanda, et al., *Coupling of plasmonic and optical cavity modes in quasi-three-dimensional plasmonic crystals.*, Nat. Commun. **2**, 479 (2011).

[35] R. Ameling, and H. Giessen, *Microcavity plasmonics: strong coupling of photonic cavities and plasmons*, Laser Photon. Rev. **7**, 141 (2013).

[36] S. Bakhti, N. Destouches, and A. V. Tishchenko, *Coupled mode modeling to interpret hybrid modes and Fano resonances in plasmonic systems*, ACS Photonics **2**, 246 (2015).

[37] C. Sauvan, J. P. Hugonin, I. S. Maksymov, and P. Lalanne, *Theory of the spontaneous optical emission of nanosize photonic and plasmon resonators*, Phys. Rev. Lett. **110**, 237401 (2013).

[38] J. Yang, H. Giessen, and P. Lalanne, *Simple analytical expression for the peak-frequency shifts of plasmonic resonances for sensing*, Nano Lett. **15**, 3439 (2015).

[39] P. T. Kristensen, R.-C. Ge, and S. Hughes, *Normalization of quasinormal modes in leaky optical cavities and plasmonic resonators*, Phys. Rev. A **92**, 053810 (2015).

[40] M. Kamandar Dezfouli, R. Gordon, and S. Hughes, *Modal theory of modified spontaneous emission of a quantum emitter in a hybrid plasmonic photonic-crystal cavity system*, Phys. Rev. A **95**, 013846 (2017).

[41] A. Sawadsky, et al., *Observation of generalized optomechanical coupling and cooling on cavity resonance*, Phys. Rev. Lett. **114**, 043601 (2015).

[42] A. C. Hryciw, M. Wu, B. Khanaliloo, and P. E. Barclay, *Tuning of nanocavity optomechanical coupling using a near-field fiber probe*, Optica **2**, 491 (2015).

[43] A. Xuereb, R. Schnabel, and K. Hammerer, *Dissipative optomechanics in a Michelson-Sagnac interferometer*, Phys. Rev. Lett. **107**, 213604 (2011).

Chapter 3

Observing Antenna Depolarization due to Cavity-Induced Backaction

In this chapter, we experimentally investigate how the polarizability of an array of gold nanorods changes due to the interaction with a high-Q microtoroid ring resonator. In particular, we demonstrate the effect of cavity-mediated backaction: The polarizability α is renormalized as fields scattered from – and returning to – the nanorods via the ring resonator depolarize the rods. Analogous to electromagnetically induced transparency, the backaction effect is most pronouncedly visible in the modification of the linear response of the rods, and is intuitively explained to result from destructive interference between incident and backaction fields at the array. The intricate interplay between the array and cavity mode allows us to *in situ* control the strength of the backaction. This is primarily achieved by phase-matching a diffraction order associated with the array to the fixed cavity mode-profile. We note that our experimental results are well-explained using a general coupled-oscillator model. In addition, we perform full coupled dipole-dipole lattice-sum calculations to support our conclusion that cavity-mediated backaction affects the polarizability.

3.1 Introduction

Descriptions of scattering by small particles generally attribute the scattering, absorption and extinction cross-section directly to the dielectric properties of the scatterer, *i.e.,* the scatterer's shape and its refractive index with respect to the host medium [1]. Central to this argument, in the limit of scatterers with a physical size much smaller the wavelength, is the so-called *polarizability*, which contains the frequency-dependent susceptibility that quantifies the strength of the dipole moment induced in the scatterer by an incident field. Rayleigh's seminal expression for the polarizability (α) of a sphere, for instance, exemplifies the notion that polarizability is directly determined by geometry and dielectric contrast [2]. A rather subtle notion is that in fact the polarizability also depends on the mode structure offered by the photonic environment. To understand this reasoning, consider that the imaginary part of the polarizability ($\mathrm{Im}[\alpha]$) is directly proportional to extinction, *i.e.* to the total power that a scatterer extracts from an incident beam [1]. This power is distributed over intrinsic dissipation (Ohmic heating) and scattering. The fact that scattering appears in $\mathrm{Im}[\alpha]$ highlights that it is a loss channel from the viewpoint of the induced dipole. The amount of light that a dipole with a given dipole moment radiates is proportional to the Local Density of Optical States (LDOS) [3]. As an example, in a photonic band gap a dipole cannot radiate, while in a cavity radiation loss is strongly enhanced. As a consequence, LDOS enters the polarizability. This is known as backaction. Even for a single scatterer placed in free-space, backaction leads to additional damping (depolarization) via the radiation continuum, and as such needs to be integrated in a self-consistent description of any system [4, 5]. The first experiment that controllably evidenced this backation effect on a plasmonic scatterer was reported in ref. [6]. Here, Buchler *et al.* used a mirror to shape the photonic background, and found a variation of the plasmon decay time related to the scatterer-mirror distance, in strong analogy to the seminal experiment by Drexhage that involved similar backaction effects on emitters [7]. It has recently been proposed [8, 9] that plasmonic antennas placed near a high-Q whispering-gallery-mode resonator can also exhibit backaction, resulting in a strong modification of the antenna's response and associated antenna properties in a narrow frequency band centred at the cavity's resonance frequency. The study of α in these systems is especially interesting, as cavity-antenna hybrids are an emerging platform providing enhanced light-matter interactions [10, 11], modifying the radiative dissipation rate of emitters placed in such complex system in non-trivial ways [8].

In this chapter, we investigate the modification of the polarizability of an array of gold nanorods interacting with a high-Q whispering-gallery-mode (WGM) of a microtoroid ring resonator. This involves probing the system discussed in chapter 2 from the 'opposite' (antenna) perspective. Here, we isolate and quantify cavity-induced backaction on the array of nanorods, defined

as the renormalization of the linear response of the nanorods due to fields scattered from – and returning to – the rods via a single mode of the ring resonator. Analogous to electromagnetically induced transparency (EIT), the backaction is most pronouncedly visible in the modification of $\mathrm{Im}[\alpha]$, *i.e.* the antenna's ability to dissipate power, and is intuitively explained to result from destructive interference between incident and backaction fields at the position of the array (fig. 3.1b). This destructive interference quenches the nanorods' susceptibility to an incoming field for the parameters studied here; the cavity thus effectively depolarizes the nanorods. Further investigations on the interplay between the nanorod array and cavity mode reveal that we are able to *in situ* control the strength of the backaction. This is achieved by phase-matching a diffraction order associated with the array to the fixed cavity mode profile, making it a more versatile system than systems containing a single antenna. The strength of the cavity-mediated backaction effect is parametrized using the (dimensionless) cooperativity $\mathcal{C}$. Using a coupled-oscillator model that we fit to our data, we retrieve a maximum value of $\mathcal{C} \approx 0.5$. Finally, we perform coupled dipole-dipole lattice-sum calculations, which support our conclusion that cavity-mediated backaction is responsible for the measured suppression of $\mathrm{Im}[\alpha]$.

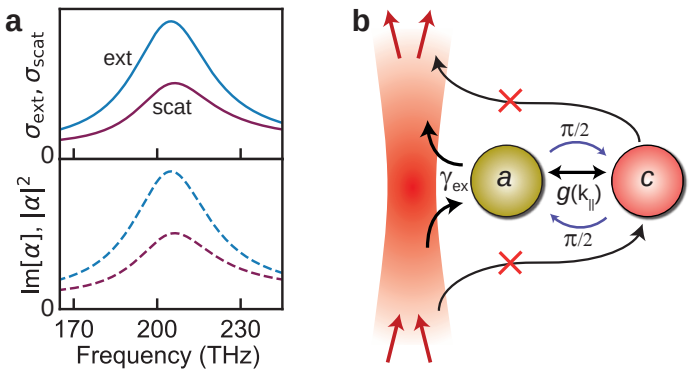

Figure 3.1: Polarizability and backaction. a, Top panel: The polarizability α of a particle dictates its scattering (σ_{scat}, purple line) and extinction (σ_{ext}, blue line) cross-section. Bottom panel: The shape of σ_{ext} is proportional to $\mathrm{Im}[\alpha]$ (dashed blue line), while σ_{scat} (dashed purple line) scales as $|\alpha|^2$. **b**, General scheme explaining how to measure backaction; the effect of the path 'a'→'c'→'a' on the polarizability α of 'a'. Critically, a measurement should avoid direct excitation or detection of resonator 'c', both conditions which are implemented in our experiment. For two resonators tuned to resonance, the backaction field is $2 \times \pi/2$ out of phase with respect to the incident drive field, resulting in destructive interference at resonator 'a' and quenching of $\mathrm{Im}[\alpha]$.

3.2 Backaction

In this section we briefly introduce the concept of 'backaction' on scatterers due to their interaction with their environment as it is known in literature (see *e.g.* [3, 12, 13]). For clarity, we first consider the example of a single scatterer. A more elaborate discussion, including lattice effects, will follow when discussing dipole-dipole lattice-sum calculations in section 3.5.

In general, the electric field $\mathbf{E}$ at observation position $\mathbf{r}$ generated by a source dipole $\mathbf{p}$ at position $\mathbf{r}'$ is given by $\mathbf{E}(\mathbf{r}) = \overleftrightarrow{G}_\mathrm{b}(\mathbf{r}, \mathbf{r}')\mathbf{p}$, with $\overleftrightarrow{G}_\mathrm{b}$ being the Green function of the embedding photonic background. For a single scatterer subject to an incoming drive field $\mathbf{E}_\mathrm{in}$, it is possible to write the induced electric dipole moment $\mathbf{p}$ as a function of its electrostatic polarizability $\overleftrightarrow{\alpha}_0$ and $\overleftrightarrow{G}_\mathrm{b}$ as [4]

$$\mathbf{p} = \overleftrightarrow{\alpha}_0 \mathbf{E}_\mathrm{tot}(\mathbf{r}_0) = \overleftrightarrow{\alpha}_0 [\mathbf{E}_\mathrm{in}(\mathbf{r}_0) + \overleftrightarrow{G}_\mathrm{b}(\mathbf{r}_0, \mathbf{r}_0)\mathbf{p}], \tag{3.1}$$

where $\mathbf{E}_\mathrm{tot}$ is the total field at the position of the scatterer ($\mathbf{r}_0$). From eq. (3.1) we immediately recognize that the resulting field $\mathbf{E}_\mathrm{tot}$ at the dipole position is not solely given by the drive field $\mathbf{E}_\mathrm{in}$, but instead also includes the field generated by the dipole acting on itself.* Alternatively, one can choose to incorporate the backaction by redefining the polarizability as the response to the incoming field $\mathbf{E}_\mathrm{in}$ via

$$\mathbf{p} = \overleftrightarrow{\alpha} \mathbf{E}_\mathrm{in}(\mathbf{r}_0), \tag{3.2}$$

where a renormalized polarizability $\overleftrightarrow{\alpha}$ is introduced,

$$\overleftrightarrow{\alpha} = \left[\overleftrightarrow{\alpha}_0^{-1} - \overleftrightarrow{G}_\mathrm{b}(\mathbf{r}_0, \mathbf{r}_0) \right]^{-1}, \tag{3.3}$$

that captures the influence of backaction via the photonic background on the original polarizability of the scatterer. Some authors name the right hand side of eq. (3.3) as the dynamic polarizability, and we briefly note that it is required to properly address $\mathrm{Re}[\overleftrightarrow{G}_\mathrm{b}]$ (which diverges at $\mathbf{r}_0$) via a procedure as detailed in [4]. For a dipole coupled to an arbitrary single cavity mode, we introduce the cavity's contribution and write

$$\overleftrightarrow{\alpha}_\mathrm{mod} = \left[\overleftrightarrow{\alpha}_\mathrm{dyn}^{-1} - \overleftrightarrow{G}_\mathrm{c}(\mathbf{r}_0, \mathbf{r}_0, \omega) \right]^{-1}, \tag{3.4}$$

where $\overleftrightarrow{G}_\mathrm{c}(\mathbf{r}_0, \mathbf{r}_0, \omega)$ is the Green function of the cavity mode associated with cavity-mediated backaction, and $\overleftrightarrow{\alpha}_\mathrm{dyn}$ is the dynamic polarizability corrected for a homogeneous background (that excludes the cavity contribution). Note the explicit dependence of $\overleftrightarrow{G}_\mathrm{c}$ on ω, introduced to signal the strong frequency dependent contribution of a narrow linewidth cavity mode.

*Note that $\overleftrightarrow{G}_\mathrm{b}$ is usually split in a homogeneous Green function $\overleftrightarrow{G}_\mathrm{hom}$ describing the embedding medium, and a Green function $\overleftrightarrow{G}_\mathrm{s}$ related to scattering.

3.2.1 Purcell factor

For the limiting case of a single scatterer, the (radiative) decay rate enhancement ($\mathrm{Im}[\overleftrightarrow{G}_\mathrm{c}]$, essentially the LDOS of the cavity [3]) offered by a single cavity mode should directly relate to the cavity's Purcell factor [14]. In this section we derive such a relation. The primary reason to do so, is to be able to recognize the connection between the Purcell factor and the more general concept of 'cooperativity' (describing the coupling strength between two general resonators, see also section 1.3.1) discussed later in this chapter.

The Purcell factor F is given by [14]

$$F = \frac{6\pi}{k^3}\frac{Q}{V_\mathrm{eff}}, \tag{3.5}$$

with $k = n\omega/c$ and n the refractive index of the medium embedding the scatterer, and the quality factor Q defined as the ratio between cavity frequency ω_c and linewidth κ as $Q \equiv \omega_\mathrm{c}/\kappa$. To find a relation between F and $\mathrm{Im}[\overleftrightarrow{G}_\mathrm{c}]$, we use the coupled equations of motion for an antenna (eq. (3.6)) with frequency(linewidth) $\omega_\mathrm{a}(\gamma)$, and single cavity mode (eq. (3.7)) as listed in ref. [9]. For simplicity the antenna is described as a point dipole with dipole moment $\mathbf{p} = p\hat{\mathbf{p}}$, where $\hat{\mathbf{p}}$ is the unit vector pointing along $\mathbf{p}$, and we assume that it is only polarizable along $\hat{\mathbf{p}}$. Similarly the fields $\{E_\mathrm{in}, E_\mathrm{c}\}$ are projections of the incident and cavity fields along $\hat{\mathbf{p}}$, respectively. In the Fourier-domain the resulting coupled equations read [9]

$$(\omega_\mathrm{a}^2 - \omega^2 - \mathrm{i}\omega\gamma)p - \beta E_\mathrm{c} = \beta E_\mathrm{in}, \tag{3.6}$$

$$-\frac{\omega^2}{\epsilon\epsilon_0 V_\mathrm{eff}}p + (\omega_\mathrm{c}^2 - \omega^2 - \mathrm{i}\omega\kappa)E_\mathrm{c} = 0, \tag{3.7}$$

where V_eff is the effective mode volume of the cavity as it is felt by the antenna at position $\mathbf{r}_0$ [9], $\epsilon = \epsilon(\mathbf{r}_0)$ and β is the antenna's oscillator strength. Note that we have not taken high-Q approximations here. From eq. (3.6) we recognize the antenna's response α_dyn as $\alpha_\mathrm{dyn} = \hat{\mathbf{p}}\cdot\overleftrightarrow{\alpha}_\mathrm{dyn}\cdot\hat{\mathbf{p}} = \beta/(\omega_\mathrm{a}^2 - \omega^2 - \mathrm{i}\omega\gamma)$, and similarly $G_\mathrm{c} = \hat{\mathbf{p}}\cdot\overleftrightarrow{G}_\mathrm{c}\cdot\hat{\mathbf{p}}$. The antenna loss rate γ can be written as the sum of nonradiative (γ_0) and radiative losses (γ_r), where the radiative losses are proportional to the LDOS. This will be especially useful when explicitly inserting the Purcell factor, as is done in the next paragraph.

Combining eqs. (3.6) and (3.7) yields an expression for α_mod, defined through $p = \alpha_\mathrm{mod}E_\mathrm{in}$, which reads

$$\alpha_\mathrm{mod} = \left[\alpha_\mathrm{dyn}^{-1} - \chi_\mathrm{c}\right]^{-1}. \tag{3.8}$$

Here we have defined the cavity's response function χ_c via

$$\chi_\mathrm{c} \equiv \frac{E_\mathrm{c}}{p} = \frac{1}{\epsilon\epsilon_0 V_\mathrm{eff}}\frac{\omega^2}{\omega_\mathrm{c}^2 - \omega^2 - \mathrm{i}\omega\kappa}. \tag{3.9}$$

Comparing with eq. (3.4), we recognize that $\chi_c = G_c$. The imaginary part of χ_c, *i.e.* the LDOS contribution of the cavity at the position of the scatterer, results in the modification of the scatterer's loss rate ($\mathrm{Im}[\alpha_{dyn}]$) due to added radiative losses provided by the cavity. To include backaction by the cavity we can thus write eq. (3.6) as

$$(\omega_a^2 - \omega^2 - i\omega\gamma_0 - i[\omega\gamma_r + \beta\,\mathrm{Im}[G_c]])p = \beta E_{in}, \tag{3.10}$$

where we split the scatterer's loss rate into a nonradiative (γ_0) and radiative (γ_r) contribution such that $\gamma = \gamma_0 + \gamma_r$. The reason to do so becomes clear when realizing that the radiative loss rate can be written as $\gamma_r = \rho\beta\pi/(6\epsilon_0\epsilon)$, where ρ is the partial LDOS related to the background medium. For vacuum the partial LDOS ρ_{vac} reads $\rho_{vac} = \omega^2/(\pi^2c^3)$ [3]. To make the connection to the Purcell factor, which is only properly defined on resonance, we rewrite $\mathrm{Im}[G_c]$ for $\omega = \omega_c$, giving

$$\mathrm{Im}[G_c] \overset{\omega=\omega_c}{=} \frac{1}{\epsilon_0\epsilon}\frac{Q}{V_{eff}} = \frac{k^3}{6\pi\epsilon_0\epsilon}F, \tag{3.11}$$

where we inserted the Purcell factor (eq. (3.5)). Inserting this, and explicit expressions for ρ_{vac} and γ_r, into eq. (3.10) gives the insightful relation

$$(\omega_a^2 - \omega^2 - i\omega\gamma_0 - i\omega\gamma_r[1+F])p = \beta E_{in}. \tag{3.12}$$

This important result confirms that a single scatterer coupled to a single mode cavity experiences an enhanced *radiative* loss rate that is directly given by the Purcell factor F (for $\omega = \omega_c$). Because we are primarily interested in the radiative losses, small resonance frequency shifts of the array due to $\mathrm{Re}[G_c]$ have not been discussed.

To end this section, we note that is possible to rewrite eq. (3.12) in terms of the Albedo A, defined as $A \equiv \gamma_r/\gamma$. Using the high-Q approximation, after insertion of the Albedo and detuning $\Delta = \omega - \omega_a$, eq. (3.12) gives

$$p = -\frac{\beta}{\omega}\frac{1}{2\Delta + i\gamma(1+AF)}E_{in}. \tag{3.13}$$

From this expression we thus find that the *total* loss rate γ is modified from its original value by the product of its Albedo and the Purcell factor of the cavity mode. In section 3.4 we will come back to this result, and discuss how the more general concept of cooperativity used to describe our experiments (where we do not measure a single scatterer) relates to this expression.

3.3 Measuring backaction

From a theoretical point of view, inspection of eqs. (3.4) and (3.8) reveals how to measure cavity-mediated backaction; simply detect the responses of the

scatterer in the presence and absence of the cavity and quantify their difference. In principle we can do this by looking at a change in either $\mathrm{Re}[\alpha]$ or $\mathrm{Im}[\alpha]$, which by itself is not a trivial task. Indeed, polarizability is not in itself a directly measurable quantity in optics. Instead one has to rely on far-field measurements of extinction and scattering, or on absorption, to infer the polarizability. In our experiment we seek to quantify the polarizability of scatterers by a far field scattering signature. It is well known that the extinction of a scatterer is a direct measurement of $\mathrm{Im}[\alpha]$. While our measurement is not a simple extinction measurement, we will argue that our measurement is primarily sensitive to $\mathrm{Im}[\alpha]$. A particular complication is that extinction, *i.e.,* removal of light in the forward beam, might be easy to measure for scatterers in absence of any other object. However, needing to bring the cavity close means that one runs the risk of not being able to purely probe the scatterers only. Practically, this means that direct excitation of the cavity mode should be prevented, as this results in a (coherent) field contribution at $\mathbf{r}_0$ that does not originate from the scatterer itself. Moreover, background radiation from the cavity directly into the detection channel, thereby spoiling the response measurement, should be prevented as well (fig. 3.1b). We approach these constraints by a combination of experimental techniques. First, we use a whispering-gallery-mode resonator, that only allows incoupling under select wavevector matching conditions. Second, we use an array of antennas as opposed to a single antenna, to obtain a strong extinction-like signal that can be probed in specular reflection with a nearly collimated plane wave. Implemented wavevector filtering of the reflected signal allows us to isolate the specular reflection and thus aids a pure response measurement of the antenna array.

3.3.1 Experimental description

In our experiment, we study the backaction imparted on gold antennas by a single cavity mode of a microtoroid ring resonator (fig. 3.2). The antennas are nanorods with length(width) of 400 nm(120 nm) and thickness of 20 nm (deposited on a glass substrate) placed in an array with 800(1500) nm pitch along the long(short) axis of the rods. We do spectroscopic response measurements on the array using a high-NA objective (NA ≈ 1.33, used with index-matching oil) which is operated in reflection. The incident drive field is polarized (s-polarization) along the principal dipole axis of the rods, which themselves are lined up to match a high-Q TE-polarized mode of the microtoroid. Focussing the incoming laser beam onto the back-focal-plane (BFP) of the objective allows us to control the angle of incidence of the drive field. As we will show, regulating this angle provides the opportunity to control the backaction, resulting from a phase-matching requirement between the cavity and the (-2) diffraction order associated with the array (fig. 3.2b). For scatterers arranged in a periodic array, scattering takes the form of diffraction into well-defined angles (wavevectors). Fourier-space filtering of the reflected light enables us to block the (-2) and

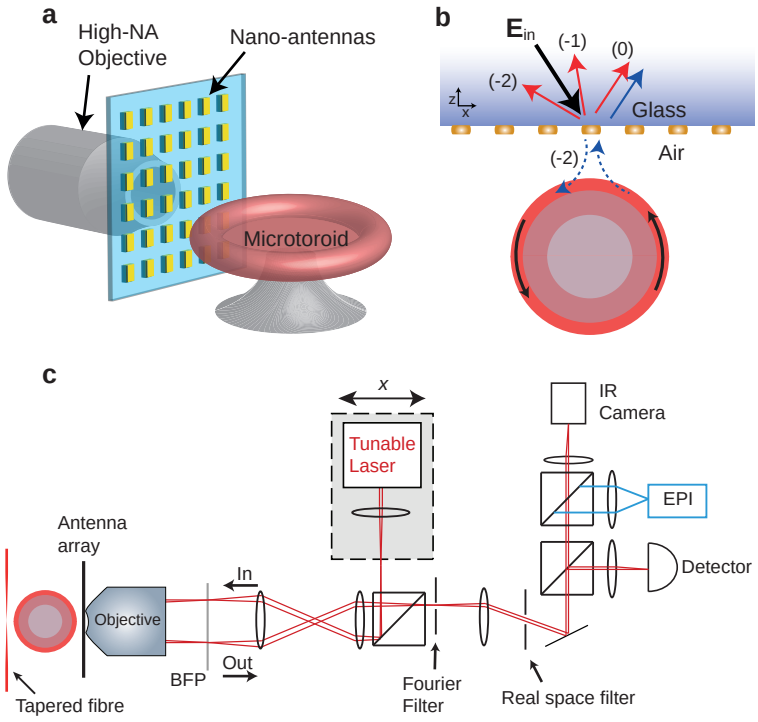

Figure 3.2: Experimental system. **a,** Sketch of the studied cavity-antenna system. **b,** Top view showing the incident drive field $\mathbf{E}_{\text{in}}$ and relevant diffraction orders in the $x-z$ plane. Solid(dashed) lines indicate propagating(evanescent) waves. For a particular parallel wavevector associated with $\mathbf{E}_{\text{in}}$, the (-2) diffraction order matches the cavity wavevector, allowing evanescent coupling to a whispering-gallery-mode in the microcavity. This antenna-induced field subsequently acts back on the antennas itself and reveals itself in the specular reflection spectrum. Importantly, the backaction effect is isolated by solely measuring the specular reflection, which is achieved by Fourier filtering of the reflected field. Our filter is set such that we disregard contributions from the (-2) and (-1) diffraction orders back into the glass, as well as direct radiation of the cavity into the glass substrate. **c**, Schematic of the optical setup used to probe the response of the array. The incoming excitation beam can be moved in position, resulting in a varying position of the focus in the back-focal-plane (BFP), which in turn changes the angle of incidence on the array. The reflection is Fourier filtered to ensure that only specular reflection is recorded on the detector. The real space filter suppresses background singles of antennas that are not coupled to the cavity. EPI: EPI illumination using an infrared source, which is used to determine the maximum collection angle of the objective (fig. 3.4c-e).

(−1) diffraction orders propagating back into the glass, such that our detector only senses the specular reflection exiting from the objective. In addition we employ a real-space filter, selecting a circular area of ∼4.5 µm in diameter, to reduce background signals not originating from antennas coupled to the cavity. Importantly, the implemented Fourier-space filtering ensures that only two possible light paths (both depicted in fig. 3.2b) contribute to the detected reflection signal; a) direct reflection of the antenna array, indicated by the solid red arrow marked with a (0) and b) the path array-cavity-array (blue arrows). Note that this latter path has to diffract twice to end up in the specular reflection path and interfere with the driving field $\mathbf{E}_{\mathrm{in}}$ on the array. The implemented filtering also safeguards that the excited cavity mode can not directly radiate into the detection channel. As such we meet the necessary requirements for a proper backaction measurement stated at the beginning of this section, meaning that a change in detected signal can be directly attributed to cavity-mediated backaction fields acting on the array.

In absence of the cavity, the array (fig. 2.1b) exhibits a broadband resonant response centred at $\omega_{\mathrm{a}}/2\pi \approx 208\,\mathrm{THz}$ (with linewidth $\gamma \approx 55\,\mathrm{THz}$), while the employed microtoroid (fig. 2.1a) has an intrinsically more narrow resonance (linewidth $\kappa \approx 30\,\mathrm{MHz}$) at slightly red-detuned frequency $\omega_{\mathrm{c}}/2\pi \approx 194.4\,\mathrm{THz}$. These numbers are obtained from independent spectroscopic measurements discussed in chapter 2. In our experiment, we probe the antennas through zero-order reflectance at a small (around 30 degree) incident angle. A technical complication is that the antennas lie on a glass-air interface which in itself is

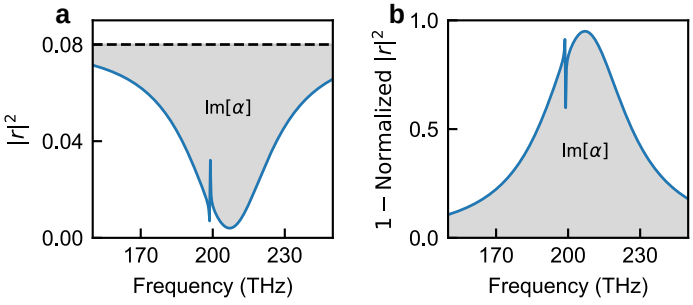

Figure 3.3: Induced transparency (depolarization) in reflection. a, Sketch of a specular reflectance spectrum for nanorods placed on a glass-air interface in the presence of a narrow cavity mode. To first-order, the broadband resonant dip in reflectance is directly proportional to Im[α] (filled grey area) of the array. A reduction of Im[α] (increasing reflectance) occurs in a narrow bandwidth centred at the cavity resonance frequency. The dashed black line indicates background reflectance resulting from the glass-air interface. **b**, To more pronouncedly visualize a reduction in Im[α], experimental data will be plotted as '1−Normalized $|r|^2$', where normalization is performed with respect to the reflectance on the bare glass-air interface. This representation allows us to directly link a reduction in Im[α] to a reduced value on the vertical axis.

reflective. Thereby it is not obvious that the reflectance signal is a measure for polarizability. To predict the lineshape that we expect for such a reflectance measurement, we quote an expression for the specular reflection r of a particle array, at normal incidence, as derived in [12]

$$r = r_{\text{glass}} + \frac{2\pi \mathrm{i} k \alpha}{A}, \tag{3.14}$$

where A is the unit-cell area of the array, k the wave number and α the polarizability for a particle placed in the centre of the array. While this expression is only strictly valid at normal incidence, it shows as main characteristic that one expects a reflection baseline given by the glass-air interface on which the resonant plasmon feature appears as a broadband reflection minimum (fig. 3.3a). This arises from destructive interference, and one can show that the deep minimum primarily reports on $\mathrm{Im}[\alpha]$. In this chapter we will show $1 -$ normalized $|r|^2$ data ($1 - \frac{|r|^2}{|r_{\text{glass}}|^2}$), such that a reduction on the vertical axis directly corresponds to a reduction in $\mathrm{Im}[\alpha]$ (fig. 3.3b). Moreover, this procedure allows us to correct the measured data for varying background values, which change as a function of the angle of incidence of the incoming drive field. Returning to our experiment in which we approach the array with the cavity, our prediction (using eq. (3.8) for α) is that the polarizability will show a reduction over a narrow spectral region, which will hence appear as a minimum in normalized $1-|r|^2$ (fig. 3.3). Such a 'transparency' peak directly connects to electromagnetically/plasmon/optomechanically induced transparency [15–18]. In these systems, the broad resonator (array) is rendered 'transparent', *i.e.* experiences a reduced susceptibility to an incident field field at the resonant frequency of the narrow resonator (cavity). Typically, the narrow peak in such systems is well described using the dimensionless 'cooperativity' ($\mathcal{C}$) parameter. To strengthen the connection between our work and induced transparency effects, we discuss the magnitude of the backaction observed in our experiment in terms of $\mathcal{C}$ in section 3.4.

3.3.2 Measurement result

The first experimental situation that we consider is shown in fig. 3.4. In particular, fig. 3.4a shows Fourier-space data that is obtained by imaging the back focal plane of the objective in *absence* of the Fourier-filter. The figure is obtained after calibration of our imaging system (fig. 3.4c-e), and is an overlay of two separate figures 1) the radiation profile of the two propagating cavity modes (clockwise/counterclockwise), obtained by directly exciting the cavity using an evanescently coupled tapered fibre (visualized using the colour scale), and 2) the position of three diffraction orders of the array for this particular illumination condition, indicated by arrows. We carefully choose an angle of incidence of $k_{\parallel}/k_0 = 0.84$, such that the (-2) diffraction order of the array overlaps with one of the propagating whispering-gallery-modes in

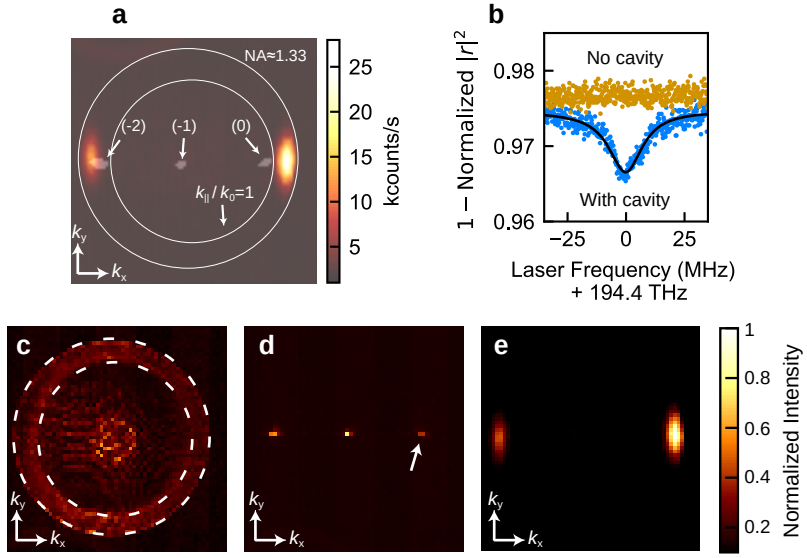

Figure 3.4: Measuring backaction. **a,** An overlay of different Fourier-images obtained via back-focal-plane imaging. The transparent white blobs indicated by arrows represent diffraction orders reflecting back into the substrate. The specular reflection, indicated by (0), is measured at $k_{\|}/k_0 = 0.84$. We stress that the angle of incidence is chosen such that the (-2) diffraction order overlaps with one of the cavity modes (indicated with the colour scale). This allows us to excite the cavity mode *via* the antenna-array. The cavity modes are visualized by driving one of them using an evanescently coupled tapered fibre, explaining the intensity difference observed between both modes. The circles indicating the numerical and maximum aperture are extracted from a fit (explained in **c**). **b,** In the presence of a cavity (blue points), the amount of scattered light into the specular reflection channel is increased with respect to the scenario without cavity (orange points), indicative of a changing Im$[\alpha]$. The reflection is normalized to the reflection on bare glass, and is measured for the situation depicted in panel **a**. The solid black line is a fit using the coupled-oscillator model. **c-e**, To generate the Fourier space images in panel **a**, we use three separately measured camera images. The colour scale next to panel **e** is similar for **c-e**. **c**, Using epi-illumination on bare glass, the brighter circular area on the edge of the figure, squashed between the two white dashed circles, is associated with Total-Internal Reflection (high reflectance). Fitting the inner and outer edge of this bright area with circular shapes gives the position of the $k_{\|}/k_0 = 1$ and NA ≈ 1.33 circles indicated in panel **a**. The fitted $k_{\|}/k_0 = 1$ circle is used as a ruler for **d** and **e**. **d**, Diffraction orders on the antenna array. To obtain the angle of incidence, we take a cross-cut along the horizontal (k_x) direction and fit the rightmost peak (0 order reflection, indicated with an arrow) with a Gaussian lineshape. To generate the overlay in **a**, we display the results using a grey saturated colour scale. **e**, The cavity mode profile is obtained by directly exciting the cavity using an evanescently coupled tapered fibre. To collect the radiation profile we position the cavity mode close to the bare glass substrate. From a fit to a cross-cut along the horizontal direction, using a Gaussian lineshape, we obtain a width in Fourier space of approximately $0.15k_{\|}/k_0$.

the microtoroid. This condition enables the incoming field to efficiently scatter to the cavity mode *via* the array using the diffraction order, which is one of the key requirements for a successful backaction experiment. Furthermore, we stress that the chosen angle of incidence also prevents direct excitation of the cavity mode, which was verified by monitoring the light exiting a tapered fibre evanescently coupled to the cavity, when measuring on the bare glass substrate. Figure 3.4b shows the resulting response of the antenna array (in the presence of the Fourier filter) in absence (orange points) and presence (blue points) of the cavity for this particular situation. We note that the overall $|r|^2 \ll 1$, meaning that we operate deep in the broadband plasmon-induced reflectance dip (fig. 3.3a). The backaction of the cavity on the array leads to a small (1%) dip in our normalized reflectance spectrum, from which we infer a small change in $\mathrm{Im}[\alpha]$. The cavity thus effectively depolarizes the nanorods over a narrow bandwidth that is commensurate with the linewidth of the high-Q cavity mode, providing evidence for the modification of $\mathrm{Im}[\alpha]$ as was previously predicted for single antennas in [8] and [9].

3.4 Controlling backation

The small effect that we observe in fig. 3.4b mainly results from a large cavity-array distance. To increase the backaction feature, we proceed by moving the cavity closer to the array (to a cavity-array distance of $\approx$1 µm), which we hope will increase the backaction strength that we can observe. Moreover, we exploit the fact that the cavity mode has a finite width in Fourier space. This suggests that the strength of the backaction does not only depend on frequency, but can also be controlled via the amount of overlap between the (-2) diffraction order and the cavity mode profile. We investigate this interesting possibility by varying the angle of incidence of the incoming drive field (fig. 3.5). As shown in fig. 3.5b, this effectively sweeps the (-2) diffraction order over the cavity mode, thus varying the degree to which the array and the cavity mode are phase-matched. The resulting spectra for various $k_{\|}/k_0$ are shown in fig. 3.5a. From this figure, we qualitatively observe a dependence of the backaction strength on the incoming angle, which is expressed as a varying depth of the cavity-induced dip. In line with the phase-matching argument, visual inspection of fig. 3.5a and fig. 3.5b suggests that cavity-mediated backaction is most prominent when the cavity mode profile and the (-2) diffraction order of the array experience better overlap. For optimal overlap, the dip in reflectance seems to be approximately 25%, a much more prominent effect than previously obtained. Full quantification of the backaction is however not straightforward, as the resonant (cavity) backaction interferes with a varying nonresonant (plasmon) background, leading to spectra exhibiting Fano lineshapes. We explain this, by noting that scatterers positioned on an interface also experience backaction related to broadband reflections originating from the interface [3, 19]. Impor-

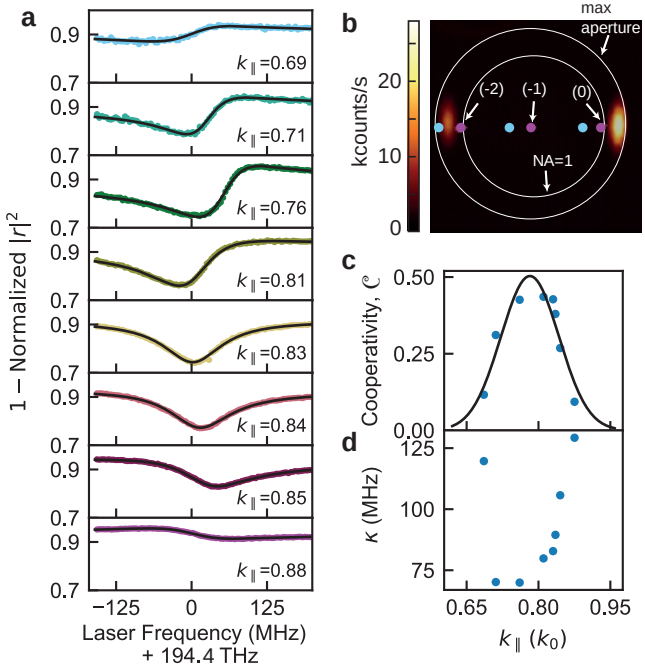

Figure 3.5: Tuning backaction. **a**, Response measurements on the array for different values of outgoing $k_{\|}$ (in units of k_0). Visual inspection of the different spectra shows that the strength of the backaction strongly depends on the incoming angle, and increases for stronger overlap between the (-2) diffraction order and the cavity mode (see panel **b**). The spectra resemble a (changing) Fano lineshape, indicative of interfering nonresonant and resonant interactions, and are fitted (black lines) with our coupled-mode model. **b**, Fourier-image overlay that shows the position of the diffraction orders at the start (blue dot, $k_{\|} = 0.69$) and stop (pink dot, $k_{\|} = 0.88$) values of the $k_{\|}$ sweep displayed in panel **a**. **c**, Values for the cooperativity obtained from fitting our coupled mode model to the spectra in **a**. We observe a clear maximum for $\mathcal{C}$ at approximately $0.78k_{\|}/k_0$. The black solid line is a fit to these data points using a Gaussian lineshape, yielding a fitted width of $k_{\|}/k_0 \approx 0.14$, in good agreement with the width directly found from the Fourier-space images ($k_{\|}/k_0 \approx 0.15$). **d,** Fitted values for the linewidth of the high-Q cavity mode, which is the bandwidth over which the nanorods are depolarized. As discussed in chapter 1, the cavity linewidth narrows when the radiation patterns of the cavity and array overlap.

tantly, the nature (phase and amplitude) of this backaction is governed by the complex Fresnel coefficient associated with the interface, which exhibits a rapid change in phase for the (evanescent) (-2) diffraction order. A changing angle of incidence thus modifies the phase of interface-mediated backaction. In our experiment, however, we measure the scatterers' response in the presence of all backaction, which is a coherent sum of the broadband interface-induced backaction plus the resonant cavity-mediated backaction. The changing phase of interface-mediated backaction when sweeping $k_{\|}$ thus directly affects the Fano lineshape as it is observed in the experiment.

3.4.1 Quantifying backaction

To facilitate a quantitative assessment, we develop a simple model based on coupled-mode theory [20] that allows us to disentangle the resonant backaction from the nonresonant background. Treating the array and cavity as resonators (fig. 3.1b), coupled at rate g and described by a Lorentzian response with complex field amplitudes a and c, respectively, we solve the driven system

$$\begin{pmatrix} \Delta_\mathrm{a} + \mathrm{i}\gamma/2 & g \\ g & \Delta_\mathrm{c} + \mathrm{i}\kappa/2 \end{pmatrix} \begin{pmatrix} a \\ c \end{pmatrix} = \begin{pmatrix} \mathrm{i}\sqrt{\gamma_\mathrm{ex}} s_\mathrm{in} \\ 0 \end{pmatrix} \tag{3.15}$$

for a, where we now assumed the high-Q limit. Here we defined $\Delta_\mathrm{a} \equiv \omega - \omega_\mathrm{a}$ and $\Delta_\mathrm{c} \equiv \omega - \omega_\mathrm{c}$, where ω is the frequency of the incident field s_in driving the array and γ_ex the rate at which the array and input/output channel are coupled. Together with the input-output relation $s_\mathrm{out} = s_\mathrm{in} - \sqrt{\gamma_\mathrm{ex}} a$ this results in

$$\frac{s_\mathrm{out}}{s_\mathrm{in}} = 1 - \frac{\mathrm{i}\gamma_\mathrm{ex}}{\Delta_\mathrm{a} + \mathrm{i}\gamma/2 - \frac{g^2}{\Delta_\mathrm{c} + \mathrm{i}\kappa/2}}. \tag{3.16}$$

From here, we proceed by parametrizing the interaction between both resonators using the cooperativity $\mathcal{C}$, defined as $\mathcal{C} = 4g^2/(\gamma\kappa)$ with $\gamma(\kappa)$ the total loss rate of the antennas(cavity). This yields

$$\frac{s_\mathrm{out}}{s_\mathrm{in}} = 1 - \frac{2\eta}{\frac{2\Delta_\mathrm{a}}{\mathrm{i}\gamma} + 1 + \frac{\mathcal{C}}{\frac{2\Delta_\mathrm{c}}{\mathrm{i}\kappa} + 1}}, \tag{3.17}$$

where we used the coupling efficiency $\eta \equiv \gamma_\mathrm{ex}/\gamma$ that determines the nonresonant background reflection. At this point we note that the cooperativity is a frequently used parameter to describe the coupling strength between two generic resonators in, for example, optomechanics [21] and CQED [22], and is the determining quantity for the height (strength) of the typical sharp spectral feature observed in electromagnetically induced transparency. Interestingly, it can be seen from eq. (3.17) that for $\Delta_\mathrm{c} = 0$, the cooperativity is essentially a measure for the increase in loss that resonator a (the 'broad' driven resonator) experiences due to coupling to a narrow linewidth resonator. This directly

connects to section 3.2.1, where we showed that the total decay rate of a single scatterer increases with the product of the Albedo (A) with the Purcell factor (F) due to the presence of a single cavity mode. We thus conclude that the cooperativity is directly proportional to the 'AF' product. Considering that we measure on multiple antennas, we will here use the cooperativity as a more general parameter quantifying the interaction in our system.

Proceeding by assuming $\omega \approx \omega_a$ and allowing the direct reflection path to pick-up an arbitrary phase ϕ, we obtain an expression for the reflectance $|r|^2 = |s_{out}/s_{in}|^2$ that reads

$$|r|^2 = \left| \exp(i\phi) - \frac{2\eta}{1 + \frac{\mathcal{C}}{\frac{2(\Delta_c - \Delta)}{i\kappa} + 1}} \right|^2 , \tag{3.18}$$

where Δ is a parameter capturing small changes in ω_c. Note that for $\{(\Delta_c - \Delta), \phi\} = 0$ this simplifies to

$$|r|^2 = \left| 1 - \frac{2\eta}{1 + \mathcal{C}} \right|^2 , \tag{3.19}$$

which is analogous to the expression used for the on-resonance optomechanically induced transparency peak discussed in the following chapters, and describes the typical spectral features observed in EIT. More importantly, we can now fit eq. 3.18 to our experimental data, yielding values for $\mathcal{C}$ as a function of $k_\parallel$ that are shown in fig. 3.5c (blue points). From a fit to this data using a Gaussian lineshape (black line), we obtain a maximum cooperativity of $\mathcal{C} \approx 0.5$ at $k_\parallel/k_0 \approx 0.78$. Notably, both the width ($k_\parallel/k_0 \approx 0.14$) and centre of this fitted Gaussian are in good agreement with the expected values based on the cavity mode profile observed in fig. 3.4a and fig. 3.5b. In addition, fig. 3.5d displays the linewidth κ of the cavity mode obtained from the fits in fig. 3.5a. In line with the discussion in chapter 2, we measure cavity linewidth narrowing when the radiation patterns of the antenna array and cavity overlap.

In conclusion, we showed that the backaction imparted by the microtoroid on an array of scatterers can be tuned via the mode overlap of a propagating WGM in the ring resonator with a diffraction order of the array. To quantify this, we parametrized the strength of the backaction via the dimensionless parameter $\mathcal{C}$. We did so using a generic coupled-mode model, allowing to disentangle resonant and nonresonant interactions, and retrieve a maximum fitted value of $\mathcal{C} \approx 0.5$. This value for $\mathcal{C}$ effectively means that about 1/3 of all antenna radiation is lost via the cavity. We think that the relatively modest value of $\mathcal{C} = 0.5$ is mainly related to the large cavity-array distance, and can be improved by more optimal positioning of the array with respect to the cavity.

3.5 Analytical dipole-dipole calculations

The previous section discussed a general model that we used to fit our experimental data. Here, we aim to provide stronger support for our experimental results and the interpretation thereof using a full electrodynamic theory. We do this using an analytical point-dipole model, which calculates the polarizability associated with a periodic lattice of dipole scatterers [12] and directly originates from Maxwell's equations. Not considering the cavity for now, this model treats each antenna in the array as a separate dipole. For such a periodic array, the associated polarizability is entirely summarized by the polarizability of a particle at the origin [12]. Importantly, and in contrast to the brief introduction in section 3.2, this polarizability is now corrected for fields generated by all other particles in the array, and the presence of the glass-air interface. To facilitate the discussion and familiarize ourself with the most important concepts, we shortly reiterate the theory as it is presented in for example [19].

The dipole moment $\mathbf{p}$ for a particle placed at the origin of an array at a distance d from an interface, that is excited by a plane wave with parallel wavevector $\mathbf{k}_\parallel$, is written as

$$\mathbf{p} = \left[\overleftrightarrow{\alpha}_{\mathrm{int}}^{-1} - \sum_{n \neq 0} \overleftrightarrow{G}_{\mathrm{b}} \left((\mathbf{R}_n, d), (0, d) \right) e^{i\mathbf{k}_\parallel \cdot \mathbf{R}_n} \right]^{-1} \mathbf{E}'_{\mathrm{in}}. \tag{3.20}$$

Here the sum over $\overleftrightarrow{G}_{\mathrm{b}}$ indicates the field at the origin generated by all particles, excluding the field generated by the dipole placed at this position. Furthermore, $\mathbf{R}_n$ is the real space lattice vector for each dipole n (indicating its position) and $\mathbf{E}'_{\mathrm{in}}$ the incident field including its reflection at the interface. Importantly, note that the single particle polarizability $\overleftrightarrow{\alpha}_{\mathrm{int}}$ in this formula is already corrected for its homogeneous (embedding) environment *and* the interface [3], but not its neighbouring dipoles. The lattice summed Green function $\mathcal{G}$ over all point-dipoles except the origin ($n \neq 0$) is then defined as

$$\mathcal{G}^{\neq} \equiv \sum_{n \neq 0} \overleftrightarrow{G}_{\mathrm{b}} \left((\mathbf{R}_n, d), (0, d) \right) e^{i\mathbf{k}_\parallel \cdot \mathbf{R}_n}, \tag{3.21}$$

which should be solved to find the response of the lattice. We will not discuss in detail on how to do this, but instead point to the relevant literature (see *e.g.* [19, 23] for details). The formalism in eqs. (3.20) and (3.21) is well established for 2D lattices in homogeneous space, using Ewald summation for exponential convergence of the lattice sums in the case that $\overleftrightarrow{G}_{\mathrm{b}}$ is $\overleftrightarrow{G}_{\mathrm{hom}}$ (with $\overleftrightarrow{G}_{\mathrm{hom}}$ the Green function for homogeneous space) [12]. Recently, Kwadrin *et al.* [19] showed how to generalize this approach for the case of lattices placed in front of a single reflective interface. In this case, one separates $\overleftrightarrow{G}_{\mathrm{b}}$ as the sum of $\overleftrightarrow{G}_{\mathrm{hom}}$ and a reflected Green function $\overleftrightarrow{G}_{\mathrm{refl}}$, where $\overleftrightarrow{G}_{\mathrm{refl}}$ is written in the angular

spectrum representation, taking the wavevector dependent Fresnel coefficient as an input. After solving for $\mathcal{G}^{\neq}$, the subsequently obtained lattice- and interface-corrected polarizability α_{lat} can used to calculate far-field observables such as, for example, reflection and transmission properties [3].

3.5.1 Simple model for cavity interaction

Due to the curvature of the microtoroid cavity, lattice sum theory that relies on wavevector conservation arguments is not strictly applicable to our experiment. To nonetheless approximate the experiment, we propose to mimic the cavity response by a resonant planar structure. This is a feasible approach, because the extension of lattice sum theory to lattices near mirrors (as reported by [19]) is not restricted to a single reflective interface. Instead, one can also consider an array of scatterers positioned in a half space in front of an arbitrary multi-layer stack. This approach simply relies on replacing the Fresnel coefficient of the single interface with the multi-layer reflection coefficient r_{eff}. We refer to fig. 3.6a/b for the proposed multilayer description. The antenna array is positioned at 50 nm from the interface, and the reflection coefficient of the stack is given by

$$r_{\mathrm{eff}} = r_{\mathrm{cav}} + r_{\mathrm{glass}}. \tag{3.22}$$

Due to the resonant nature of the single cavity mode (in frequency and wavevector), r_{eff} is equivalent to r_{glass}, except for very specific frequencies and wavevectors at which it is possible to excite the cavity. For our calculations, we approximate r_{cav} as

$$r_{\mathrm{cav}} \equiv \frac{-\kappa_{\mathrm{ex}}}{(\omega - \omega_{\mathrm{c}}) + \mathrm{i}\kappa/2}, \tag{3.23}$$

with κ_{ex} defined as

$$\kappa_{\mathrm{ex}} \equiv \frac{\kappa}{2} \times e^{(-|k_{\parallel} - k_{\parallel,\mathrm{c}}|^2)/(2\sigma^2)}. \tag{3.24}$$

Here κ_{ex} constitutes a Gaussian lineshape centred at $k_{\parallel,\mathrm{c}}$ (the wavevector of the cavity mode) with a width given by σ. As a result of these definitions, r_{cav} is only nonzero over a small (Lorentzian) frequency bandwidth and for particular wavevectors, in close analogy the experimental situation. We note that the pre-factor $\kappa/2$ in eq. (3.24) is chosen such that eq. (3.23) yields unity reflection for perfect phase-matching and $\omega = \omega_{\mathrm{c}}$, maximizing the effect of our resonant structure. A drawback of our model is that we can not easily determine the 'real' pre-factor that we should use. In reality, the pre-factor should relate to the cavity-array distance, and determine the strength of the backaction. This is easily realized when taking the limit of infinite cavity-array separation, then r_{eff} should be entirely given by r_{glass} such that r_{cav} is always 0. To end this section, we mention two other approximations. First of all, we note the resonant planar structure has an equal interaction with all antennas in the array. Although this is a requirement for the proper implementation of

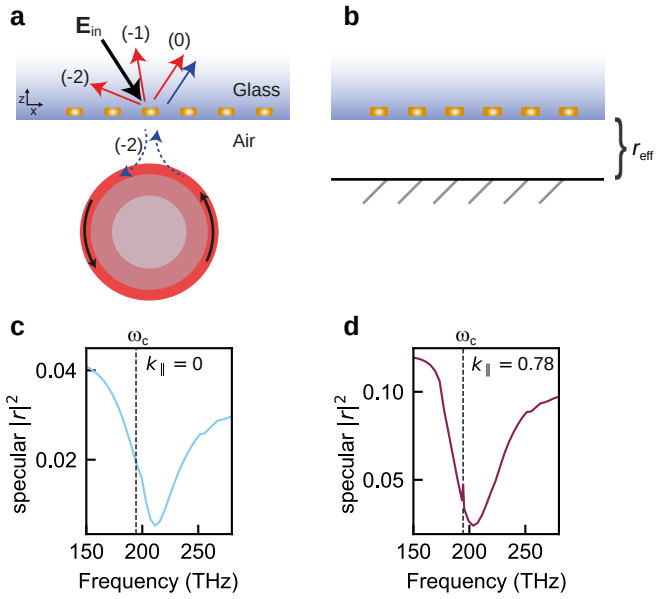

Figure 3.6: Lattice-sum calculations. **a**, Cartoon explaining the position of the antennas in the lattice-sum calculation. In contrast to the experiment, the antennas are placed inside the glass (which is given a refractive index of 1.5) environment. **b**, In our calculation, we capture the combined effect of the interface and cavity in a single Fresnel coefficient r_{eff}. **c**, The calculated specular reflectance of the array (for normal incidence) shows a clear broadband dip associated with the plasmon resonance. The dashed line indicates the resonance frequency associated with the cavity mode. **d**, For $k_{\parallel}/k_0 = 0.78$, we observe the same signature. Note that due to the larger angle of incidence, the background signal coming from the glass-air interface is higher than in **c**. Importantly, the sharp feature that is visible at ω_c is directly related to the presence (backaction) of the cavity. A zoomed in plot further exploring this effect is given in fig. 3.7. Importantly, for both calculations, so also for larger incoming angles, the expected reflectance feature of the array is similar to our expectation that was discussed in section 3.3.

our calculations, it is in contrast to our experiment, where the curvature of the microtoroid ensures that the single cavity mode only interacts with a select number of antennas. A second difference between experiment and calculation is the positioning of the antenna array inside the glass environment, which is necessary to approximate the interface+cavity as a simple reflective multilayer. This positioning will slightly influence the total field at the position of the array. However, taking into account that s-polarized fields are continuous across the boundary, and that we positioned our antennas at a distance of $\lambda/20$ from the substrate, we estimate the resulting difference originating from this change in position to be relatively small.

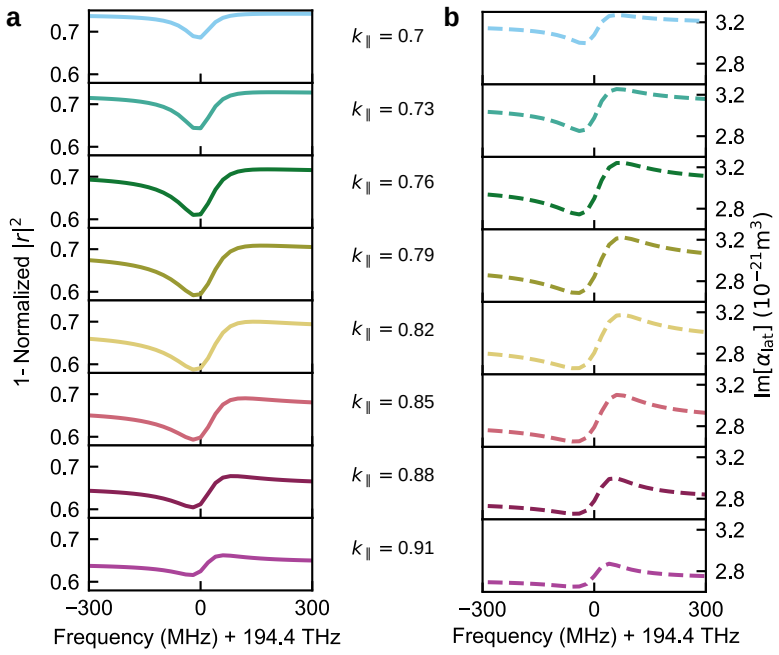

Figure 3.7: Sweeping the angle in our lattice-sum calculations. For both **a** and **b** the sub panels are associated with incoming wavevectors (in units of k_0) given by the values in between **a** and **b**. **a,** Similar to our experiment, the calculation predicts a narrow bandwidth dip in reflectance resulting from backaction, that is maximized for a wavevector for which the second diffraction order matches the wavevector of the cavity. **b,** The modification of $\mathrm{Im}[\alpha_{\mathrm{lat}}]$ also displays this strong dependence on incoming wavevector. Interestingly, its shape is more reminiscent of a Fano lineshape. We attribute this to the fact that we do not perform a pure extinction measurement, solely probing $\mathrm{Im}[\alpha_{\mathrm{lat}}]$, but are instead also sensitive to a term scaling with $|\alpha_{\mathrm{lat}}|^2$.

3.5.2 Calculation results

Using our model, we plot the specular reflectance spectra for two different illumination conditions in fig. 3.6c (normal incidence) and fig. 3.6d ($k_\parallel/k_0 = 0.78$). In both scenarios, we observe a broadband dip that can be attributed to the plasmon resonance. It is noteworthy that these analytical calculations show very good agreement with the specular reflectance spectrum as predicted in section 3.3. In addition to this broadband dip, we observe a small peak in the reflectance spectrum that is associated with the presence of the cavity in fig. 3.6d. To investigate this in more detail, fig. 3.7a displays small frequency bandwidth spectra for various $k_\parallel$, in a similar presentation as previously discussed for the experiment. From this figure we directly observe a dip in '1 − normalized reflectance' similar to that we measured our experiment.

Moreover, the depth of this dip significantly depends on the angle of incidence, showing that the we can reproduce the main feature of our experiment using our model. The benefit of doing these calculations is the access to the (corrected) polarizability α_{lat} of the array. Figure 3.7b shows the imaginary part of α_{lat} as we obtain it from our model. Similar to the reflectance, this plot shows that the backaction and its effect on α_{lat} can be controlled via the incident angle of the incoming drive field. Interestingly, whereas the specular reflectance (fig. 3.7a) displays a clear dip, the polarizability has a more Fano-like resonant signature. The polarizability of the array thus quickly changes around the cavity resonance frequency. We attribute this somewhat surprising discrepancy in shape between ($1 -$ normalized $|r|^2$) and $\mathrm{Im}[\alpha_{\mathrm{lat}}]$ to the fact that we do not perform a pure extinction measurement, but instead also partly probe $|\alpha_{\mathrm{lat}}|^2$, which can be related to scattering by the antennas. The interplay between these two contributions, scattering and extinction, most likely gives rise to a more complex behaviour that results from the interplay between the real and imaginary parts of $\overleftrightarrow{G}_{\mathrm{hom}}$, $\overleftrightarrow{G}_{\mathrm{refl}}$ and $\overleftrightarrow{G}_{\mathrm{c}}$. Finally, we point towards an observed difference in Fano lineshapes for $|r|^2$ as we calculate them in fig. 3.7a, and observe them experimentally in fig. 3.5a. For example, for large angle of incidence (the bottom panel in both figures), the observed shapes exhibit an opposite Fano lineshape. We think that this difference can be attributed to the positioning of the antennas. In the experiment we place the array on the air side of the interface, while in the calculation we put them inside the glass environment. As scatterers positioned on an interface also experience backaction that relates to reflections originating from the interface, the phase of these reflections (contained in the complex Fresnel coefficient) is important. For evanescent waves (the (-2) diffraction order) incident from the air side, this phase is opposite to that experienced by evanescent waves entering from the glass side. This opposite phase might change the interference condition with the directly reflected (zero-order) light, and as a consequence can lead to a difference in reflectance signal.

3.6 Conclusion

In conclusion, we have monitored the linear response of an antenna array in the presence of a high-Q single cavity mode, in an experiment that was designed to measure cavity-mediated backaction on the array. In other words, our measurements effectively probed a bright broadband resonant feature (array) in the presence of a dark spectrally narrow cavity mode. In doing so, we observed typical EIT like lineshapes, where the bright (broad) resonator experiences a reduced susceptibility in a spectrally narrow window around the resonance frequency of the dark mode. This reduced susceptibility is directly related to cavity-mediated backaction fields imparted on the array. Interestingly, the use of an array allowed us to use a diffraction order to control the backation

strength, which we explained using a phase-matching argument. Our results are well-explained using a coupled-mode model, and allow us to retrieve a maximum cooperativity of $\mathcal{C} = 0.5$. For a single antenna, taking into account that the Albedo is always equal or less than 1, this value for the cooperativity translates into a (modest) Purcell-enhanced radiative decay rate with a Purcell factor ≥ 0.5. This relatively low number mainly results from the large distance between the cavity and array, significantly limiting the backaction imparted on the antennas. Using a fully analytical point-dipole theory, we provided further evidence for the dressing of α resulting from backaction by the cavity mode. From a fundamental point of view, we think that our results could benefit the understanding of hybrid cavity-antenna systems, which are seen as a promising platform for the emission enhancement of single emitters. Moreover, the experiments performed here provide simple and independent free-space readout of the cavity emission enhancement factor, linewidth and resonance frequency. The strong frequency and wavevector dependent modification of α allows to selectively enhance emission of nearby placed emitters in a very narrow frequency range.

References

[1] C. F. Bohren, and D. R. Huffman, *Absorption and scattering of light by small particles* (John Wiley and Sons, 1983).

[2] J. W. Strutt, *On the light from the sky, its polarization and colour*, Philos. Mag. **41**, 107 (1871).

[3] L. Novotny, and B. Hecht, *Principles of nano-optics* (Cambridge University Press, Cambridge, 2012), 2nd ed.

[4] P. de Vries, D. V. van Coevorden, and A. Lagendijk, *Point scatterers for classical waves*, Rev. Mod. Phys. **70**, 447 (1998).

[5] M. Agio, and A. Alù, *Optical antennas* (Cambridge University Press, 2013).

[6] B. C. Buchler, T. Kalkbrenner, C. Hettich, and V. Sandoghdar, *Measuring the quantum efficiency of the optical emission of single radiating dipoles using a scanning mirror*, Phys. Rev. Lett. **95**, 063003 (2005).

[7] K. Drexhage, *Influence of a dielectric interface on fluorescence decay time*, J. Lumin. **1-2**, 693 (1970).

[8] M. Frimmer, and A. F. Koenderink, *Superemitters in hybrid photonic systems: A simple lumping rule for the local density of optical states and its breakdown at the unitary limit*, Phys. Rev. B **86**, 235428 (2012).

[9] H. M. Doeleman, E. Verhagen, and A. F. Koenderink, *Antenna–cavity hybrids: matching polar opposites for purcell enhancements at any linewidth*, ACS Photonics **3**, 1943 (2016).

[10] Y.-F. Xiao, et al., *Strongly enhanced light-matter interaction in a hybrid photonic-plasmonic resonator*, Phys. Rev. A **85**, 031805 (2012).

[11] A. F. Koenderink, *Single-Photon Nanoantennas*, ACS Photonics **4**, 710 (2017).

[12] F. J. García de Abajo, *Colloquium: Light scattering by particle and hole arrays*, Rev. Mod. Phys. **79**, 1267 (2007).

[13] M. Frimmer, *Spontaneous emission near resonant optical antennas*, Ph.D. thesis, University of Amsterdam (2012).

[14] E. M. Purcell, *Spontaneous emission probabilities at radio frequencies*, Phys. Rev. **69**, 681 (1946).

[15] M. Fleischhauer, A. Imamoglu, and J. P. Marangos, *Electromagnetically induced transparency: Optics in coherent media*, Rev. Mod. Phys. **77**, 633 (2005).

[16] S. Zhang, D. A. Genov, Y. Wang, M. Liu, and X. Zhang, *Plasmon-induced transparency in metamaterials*, Phys. Rev. Lett. **101**, 047401 (2008).

[17] N. Liu, et al., *Plasmonic analogue of electromagnetically induced transparency at the Drude damping limit.*, Nat. Mater. **8**, 758 (2009).

[18] S. Weis, et al., *Optomechanically induced transparency*, Science **330**, 1520 (2010).

[19] A. Kwadrin, C. I. Osorio, and A. F. Koenderink, *Backaction in metasurface etalons*, Phys. Rev. B **93**, 104301 (2016).

[20] H. A. Haus, *Waves and fields in optoelectronics* (Prentice-Hall, 1984).

[21] M. Aspelmeyer, T. J. Kippenberg, and F. Marquardt, *Cavity optomechanics*, Rev. Mod. Phys. **86**, 1391 (2014).

[22] P. Lodahl, S. Mahmoodian, and S. Stobbe, *Interfacing single photons and single quantum dots with photonic nanostructures*, Rev. Mod. Phys. **87**, 347 (2015).

[23] C. M. Linton, *Lattice sums for the Helmholtz equation*, SIAM Rev. **52**, 630 (2010).

Part II

Nonreciprocity in Optomechanics

Chapter 4

Theory of Optomechanically Induced Nonreciprocity

Optical isolation, artificial magnetic fields for photons and topological photonic phases based on synthetic gauge fields have raised significant interest in recent literature. Cavity-optomechanical systems that involve multiple optical modes parametrically coupled to common mechanical modes form a versatile platform to realize these effects. In this chapter, we establish a unifying theoretical framework describing optical nonreciprocity in multimode optomechanical systems consisting of two optical cavities coupled to a single mechanical resonator. We highlight two general scenarios to achieve isolation, relying on either optical or mechanical losses. Depending on the loss mechanism, our theory defines the requirements for optimal isolation and the available operational bandwidth in these systems. Our results provide general insights into a broad class of parametrically modulated nonreciprocal devices, paving the way towards optimal nonreciprocal systems for low-noise integrated nanophotonics.

4.1 Introduction

The creation of engineered photonic systems exhibiting transmission properties that differ upon a switch of source and detector would give access to asymmetric devices such as isolators and nonreciprocal phase shifters (gyrators). To obtain these unusual systems it is required to break Lorentz reciprocity, a fundamental property of electromagnetic waves that propagate in a linear and time-independent medium [1, 2]. Traditional approaches to break Lorentz reciprocity involve the interaction between a static magnetic-field and magneto-optic materials [3–6], exploiting the Faraday effect, where the magnetic field induces a propagation-dependent phase shift on different components of the propagating light field. Although state-of-the-art on-chip implementations have achieved isolation ratios as high as 19.5 dB at telecom wavelengths [6] using this approach, it requires non-standard materials and presents a challenging scaling and integration problem. Moreover, the external magnetic fields involved are generally not commensurate with sensitive quantum information processes that require a minimum of disruptive external influence. As such, the search for alternative physical methods that mimic the role of the external magnetic field has taken shape in recent years [7–23]. A promising approach relies on spatiotemporal modulation of the refractive index to break time-reversal symmetry. As first demonstrated by the research group of Shanhui Fan, such modulation allows to impart a nonreciprocal phase on the transfer of a signal between two optical modes [10, 24–26]. Cavity-optomechanical systems [27] that involve two optical modes coupled to a common mechanical mode form an useful platform to realize these effects, as in these systems it is the optical cavity field itself that can provide the modulation of the refractive index via a coupling to a mechanical resonator. This platform has recently provided successful implementations of optomechanically induced nonreciprocal light transmission in optomechanical ring resonators [28, 29], photonic-crystal circuits [30] and has also been demonstrated in electromechanical systems [23, 31, 32].

In this chapter a unifying theoretical framework to analyze optical nonreciprocity in three-mode optomechanical systems is presented. To start, section 4.2 discusses the most basic requirements that need to be fulfilled to obtain a nonreciprocal response in a system of two optical modes that are coupled to two in/output ports. Section 4.3 treats how the coupling between these optical modes via a joint mechanical resonator can lead to a nonreciprocal phase pickup. Afterwards, two specific optomechanical implementations are highlighted, which are discriminated based on their interference and dissipation channels that lead to optical isolation. Depending on the interference and loss mechanism, the theoretical framework predicts the requirements for optimal isolation. In addition, the available operational bandwidth is shown to critically depend on the loss mechanism involved. In conjunction with a formal derivation of the scattering parameters that describe these systems, we provide intuitive explanations capturing the physics.

4.2 Nonreciprocity in a two-mode optical system

Before investigating the multimode optomechanical system at the core of this chapter, consider a general two-mode system as shown in fig. 4.1. The temporal-evolution equations of a such a system can be described via [33]

$$\frac{\mathrm{d}}{\mathrm{d}t}\begin{pmatrix} a_1 \\ a_2 \end{pmatrix} = \mathrm{i}\mathcal{M}\begin{pmatrix} a_1 \\ a_2 \end{pmatrix} + D^{\mathrm{T}}\begin{pmatrix} s_1^+ \\ s_2^+ \end{pmatrix}, \tag{4.1}$$

$$\begin{pmatrix} s_1^- \\ s_2^- \end{pmatrix} = C\begin{pmatrix} s_1^+ \\ s_2^+ \end{pmatrix} + D\begin{pmatrix} a_1 \\ a_2 \end{pmatrix}, \tag{4.2}$$

where $\mathcal{M}$ represent a linear matrix that describes the time-evolution of the fields in modes $\{a_1, a_2\}$ in the absence of external driving. As noted in section 1.3, the matrix D describes the coupling between the two ports and optical modes and C describes the direct scattering path between ports 1 and 2. Note that s_j^+ and s_j^- are normalized such that $|s_j^+|^2$ is the input photon flux in channel j, while a_1 and a_2 are normalized such that the energy in mode i is given by $|a_i|^2$. Analogous to the discussion in section 1.3, we have enforced the optical modes to each satisfy reciprocity, in the sense that the in- and out-coupling rates of a particular mode and port are equal, thus the coupling is described through the same matrix D (and its transpose) in eqs. (4.1) and (4.2) [33]. Here we assume that the evolution operator $\mathcal{M}$ does not explicitly depend on time, as in the case of systems with externally controlled parametric modulation. However, $\mathcal{M}$ can include time derivatives, which for example applies to optomechanical systems exhibiting self-induced parametric modulation.

The Fourier transform of $\mathcal{M}$ is written as M and contains two terms: (1) the bare optical evolution and (2) a term related to the optomechanical coupling. We write the term related to the optical evolution as Θ, which itself can be written as $\Theta = O + \mathrm{i}K/2$. Here O and K are real and symmetric matrices,

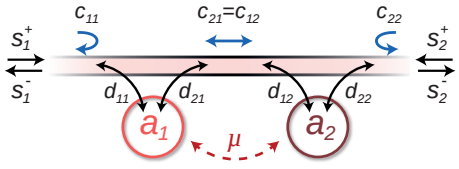

Figure 4.1: Schematic representation of a two-port waveguide-cavity arrangement involving two optical modes. The relevant mode-to-port coupling rates are indicated by the rates d_{ji}, which are matrix elements of the coupling matrix D. In addition, elements of the direct-scattering matrix C are indicated, where C is considered reciprocal such that $c_{12} = c_{21}$. The direct mode-to-mode coupling rate (μ) is indicated by a red dashed arrow.

with the diagonal and off-diagonal elements of O containing the resonance frequencies $\{\omega_1, \omega_2\}$ of the two optical modes and their direct coupling rate μ, respectively. The losses of both modes are captured in K, and can be decomposed into exchange (K_e) and intrinsic losses (K_0) as $K = K_0 + K_\mathrm{e}$. The diagonal and off-diagonal elements of K represent the total losses of each mode (κ_1, κ_2), and the coupling between two modes due to interference in the joint output channels (κ_r), respectively.

For completeness we note that in absence of radiative coupling ($\kappa_\mathrm{r} = 0$), the bare optical evolution matrix Θ is analogous to the M matrix shown in eq. (1.13), containing only a passive coupling rate on the off-diagonal elements (and thus not the optomechanical coupling). Even though in general Θ is not diagonal, it is possible to choose a proper eigenmode basis such that Θ becomes diagonal [29]. This diagonalization leads to normal modes whose complex frequencies are, for example, 'dressed' by the original couplings μ, such that $\omega_1 = \omega_1 - \mu$ and $\omega_2 = \omega_2 + \mu$, and 2μ is the normal-mode frequency splitting. In the following, we consider these dressed eigenfrequencies, and thus take as a convention a diagonalized optical evolution matrix Θ.

In the frequency domain*, eqs. (4.1) and (4.2) directly give the scattering matrix S, defined via

$$\begin{pmatrix} s_1^- \\ s_2^- \end{pmatrix} = S \begin{pmatrix} s_1^+ \\ s_2^+ \end{pmatrix}, \tag{4.3}$$

reading

$$S = C + \mathrm{i}D(M + \omega I)^{-1} D^\mathrm{T}, \tag{4.4}$$

where I represents the 2×2 identity matrix. For clarity, we stress that here the M matrix contains the bare optical evolution captured in Θ, and in addition also the yet unknown contribution from the optomechanical interaction. Any nonreciprocal element exhibits an asymmetric S matrix [2], which for an ideal isolator is given by

$$S = \begin{pmatrix} 0 & 0 \\ 1 & 0 \end{pmatrix} \tag{4.5}$$

In this context, our main interest lies with the difference between off-diagonal scattering elements, representing backward and forward transmission, respectively. For a symmetric (reciprocal) scattering matrix C, their contrast is given by

$$s_{21} - s_{12} = \frac{\mathrm{i}\det(D)(m_{12} - m_{21})}{\det(M + \omega I)}. \tag{4.6}$$

This result directly shows that a the necessary condition for breaking reciprocity is to ensure $\det(D) \times (m_{12} - m_{21}) \neq 0$, which needs (a) $\det(D) \neq 0$, and (b) $m_{12} \neq m_{21}$. The first condition requires D to be a full rank matrix, which is expected as in the case of a non-full-rank D both optical modes are symmetrically coupled to the two ports, thus preserving reciprocity. The second

*with the Fourier transform defined as $a[\omega] = \int a(t) \exp(\mathrm{i}\omega t)\, \mathrm{d}t$

condition is quite demanding as it requires an asymmetry in the *total* evolution matrix M, enforcing the coupling rate from mode 1 to mode 2 to be different from that of mode 2 to mode 1. In the next section, however, we show that optomechanical interactions can break the symmetry in this mode-conversion process, leading to a nonreciprocal optical response.

4.3 Multimode optomechanics

Consider a basic system (fig. 4.2) of two optical modes with frequencies $\{\omega_1, \omega_2\}$ and photon annihilation operators $\{\hat{a}_1, \hat{a}_2\}$, both coupled (with single photon-phonon coupling rate g_0) to a mechanical mode (phonon annihilation operator $\hat{b}$) with frequency Ω_m. Note that in the remainder we omit the operator 'hat' symbol for the photon and phonon annihilation operators, realizing that the equations of motion (EOM) in a quantum optics picture directly map to the EOM as they are obtained for a classical complex mode amplitude [27].

If both optical modes are driven by a strong coherent control laser to an intracavity field $\alpha_i \exp(-\mathrm{i}\omega_\mathrm{control} t)$, the linearized optomechanical Hamiltonian ([27] and section 1.5) in a frame rotating at ω_control reads

$$H_\mathrm{L} = -\hbar \sum_{i=1,2} \bar{\Delta}_i \delta a_i^\dagger \delta a_i + \hbar \Omega_\mathrm{m} b^\dagger b \\ -\hbar \sum_{i=1,2} (g_i^* \delta a_i b^\dagger + g_i \delta a_i^\dagger b + g_i^* \delta a_i b + g_i \delta a_i^\dagger b^\dagger). \tag{4.7}$$

Here $\bar{\Delta}_i$ is the control detuning with respect to the two cavity frequencies and, as a result of the linearization, δa_i and $\delta a_i^\dagger$ describe the small-amplitude changes

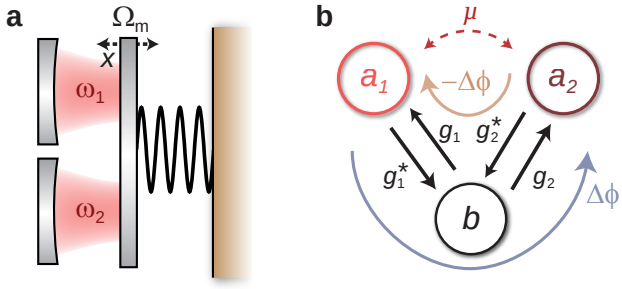

Figure 4.2: Nonreciprocity in a multimode optomechanical system. **a**, Optomechanical system: two optical resonators at frequencies ω_1 and ω_2, both coupled to a mechanical mode at frequency Ω_m. **b**, General description: the optical modes (a_1, a_2) are coupled to a mechanical mode b with the control-field enhanced optomechanical coupling rates g_1 and g_2. The path $a_1 \to b \to a_2$ picks up a phase $\Delta\phi = \arg(g_2) - \arg(g_1)$ that is opposite to that of the reversed path $a_2 \to b \to a_1$.

of the optical field. The interaction terms on the second line describe the coupling between the optical and mechanical modes at rates $g_i = g_0\alpha_i$, controlled through the fields α_i. These terms correspond to Raman-like interactions that involve the creation or annihilation of photons in sidebands of the control laser upon creation or annihilation of phonons in the mechanical resonator. Interestingly, the crucial role of the relative phases of g_i is immediately revealed when considering energy-conserving pairs that mediate inter-mode transfer. For example, photon annihilation in mode 1 upon phonon creation ($g_1^*\delta a_1 b^\dagger$), and the subsequent annihilation of the phonon with photon creation in mode 2 ($g_2\delta a_2^\dagger b$) leads to a phase pickup $\Delta\phi = \arg(g_2) - \arg(g_1)$, whereas the reverse process provides an opposite phase $-\Delta\phi$ (fig. 4.2b) [34, 35]. Strongest nonreciprocity is thus achieved when the two optical modes are driven with a phase difference $\Delta\phi = \pm\pi/2$.

To investigate this in more detail, we use eq. (4.7) to derive equations of motion for the photon and phonon annihilation operators, including dissipation and coupling between the mechanical resonator and its thermal bath. Moreover, we incorporate coupling to the optical (input/output) bath using a standard procedure as detailed in section 1.5 and for example ref. [36]. Introducing shorthand notations $\mathbf{a} = (\delta a_1, \delta a_2)^{\mathrm{T}}$ and $\mathbf{s}^+ = (\delta s_1^+, \delta s_2^+)^{\mathrm{T}}$, and assuming the diagonalized optical modes, the equations of motion read

$$\dot{\mathbf{a}} = \mathrm{i}\begin{pmatrix} \bar{\Delta}_1 + \mathrm{i}\kappa_1/2 & 0 \\ 0 & \bar{\Delta}_2 + \mathrm{i}\kappa_2/2 \end{pmatrix}\mathbf{a} + \mathrm{i}\begin{pmatrix} g_1(b+b^\dagger) \\ g_2(b+b^\dagger) \end{pmatrix} + D^{\mathrm{T}}\mathbf{s}^+, \tag{4.8}$$

and

$$\dot{b} = (-\mathrm{i}\Omega_{\mathrm{m}} - \Gamma_{\mathrm{m}}/2)\, b + \mathrm{i}(g_1^*\delta a_1 + g_1\delta a_1^\dagger + g_2^*\delta a_2 + g_2\delta a_2^\dagger) + \sqrt{\Gamma_{\mathrm{m}}}b_{\mathrm{in}}. \tag{4.9}$$

Here, the rightmost term accounts for (thermal) fluctuations entering via the mechanical bath, which, via an anti-Stokes scattering process, can lead to unwanted noise photons entering the system. For now we neglect these fluctuations impinging on the mechanical resonator. Likewise, we neglect noise at optical frequencies.

In the frequency domain, after making the rotating-wave approximation, eqs. (4.8) and (4.9) result in

$$\mathrm{i}\left[\begin{pmatrix} \Sigma_{\mathrm{o}_1} & 0 \\ 0 & \Sigma_{\mathrm{o}_2} \end{pmatrix} + \left(\frac{1}{\Sigma_{\mathrm{m}}^-} - \frac{1}{\Sigma_{\mathrm{m}}^+}\right)\begin{pmatrix} |g_1|^2 & g_1 g_2^* \\ g_1^* g_2 & |g_2|^2 \end{pmatrix}\right]\mathbf{a} + D^{\mathrm{T}}\mathbf{s}^+ = 0, \tag{4.10}$$

where we defined the inverse susceptibilities

$$\Sigma_{\mathrm{m}}^{\pm} \equiv \omega \mp \Omega_{\mathrm{m}} + \mathrm{i}\frac{\Gamma_{\mathrm{m}}}{2}; \quad \Sigma_{\mathrm{o}_{1,2}} \equiv \omega + \bar{\Delta}_{1,2} + \mathrm{i}\frac{\kappa_{1,2}}{2}. \tag{4.11}$$

Given that we are particularly interested in probe signals that are detuned from the control by approximately the mechanical resonance frequency ($|\omega \mp$

$\Omega_\mathrm{m}| \ll \Omega_\mathrm{m}$), one can always neglect one of the two terms involving mechanical susceptibilities $1/\Sigma_\mathrm{m}^\pm$. For $\bar{\Delta}_i \approx \mp\Omega_\mathrm{m}$, where the sign indicates the detuning of the control field to the red (top sign) or blue(bottom sign) motional sideband of the cavity modes (see also fig. 1.6), the frequency-domain evolution matrix M (section 4.2) is found from eq. (4.10) as

$$M = \begin{pmatrix} \bar{\Delta}_1 + \mathrm{i}\frac{\kappa_1}{2} & 0 \\ 0 & \bar{\Delta}_2 + \mathrm{i}\frac{\kappa_2}{2} \end{pmatrix} \mp \frac{1}{\Sigma_\mathrm{m}^\pm} \begin{pmatrix} |g_1|^2 & g_1 g_2^* \\ g_1^* g_2 & |g_2|^2 \end{pmatrix}. \tag{4.12}$$

Clearly, in order to break the symmetry of M – a necessary condition to break reciprocity of the system – one needs to enforce $g_1 g_2^* \neq g_1^* g_2$. As previously established by direct assessment of the linearized Hamiltonian (4.7), this requires $\Delta\phi = \arg(g_2) - \arg(g_1) \neq n\pi$ where $n \in \mathbb{N}$.

Using the retrieved M matrix in combination with eq. (4.4) yields the scattering matrix S *including* optomechanical interactions, reading

$$\begin{aligned} S &= C + \mathrm{i}D(M + \omega I)^{-1} D^\mathrm{T} \\ &= C + \mathrm{i}D \begin{pmatrix} \Sigma_{\mathrm{o}_1} \mp |g_1|^2/\Sigma_\mathrm{m}^\pm & \mp(g_1 g_2^*)/\Sigma_\mathrm{m}^\pm \\ \mp(g_1^* g_2)/\Sigma_\mathrm{m}^\pm & \Sigma_{\mathrm{o}_2} \mp |g_2|^2 \Sigma_\mathrm{m}^\pm \end{pmatrix}^{-1} D^\mathrm{T}. \end{aligned} \tag{4.13}$$

Together with eq. (4.6), the difference in transmission $s_{21} - s_{12}$ is directly given as

$$s_{21} - s_{12} = 2\sin\Delta\phi \frac{\det D}{\sqrt{\kappa_1\kappa_2}} \frac{\mp 2\sqrt{\mathcal{C}_1\mathcal{C}_2}}{(\delta_\pm + \mathrm{i})(\delta_1 + \mathrm{i})(\delta_2 + \mathrm{i}) \mp (\mathcal{C}_2(\delta_1 + \mathrm{i}) + \mathcal{C}_1(\delta_2 + \mathrm{i}))}, \tag{4.14}$$

where again the upper and lower signs relate to red ($\bar{\Delta}_{1,2} \approx -\Omega_\mathrm{m}$) and blue ($\bar{\Delta}_{1,2} \approx +\Omega_\mathrm{m}$) detuned regimes respectively, and we have defined the cooperativities $\mathcal{C}_i$ and normalized detunings δ as

$$\mathcal{C}_i \equiv \frac{4|g_i|^2}{\kappa_i \Gamma_\mathrm{m}}, \quad \delta_\pm \equiv \frac{\omega \mp \Omega_\mathrm{m}}{\Gamma_\mathrm{m}/2}, \quad \delta_i \equiv \frac{\omega + \bar{\Delta}_i}{\kappa_i/2}. \tag{4.15}$$

To conclude, note that eqs. (4.14) and (4.13) are general in the sense that they are valid regardless of the way the modes are coupled to the ports. In section 4.5 we will consider specific implementations and derive the resulting D matrices completing these expressions.

4.3.1 The determinant of the coupling matrix D

From eq. (4.14) it is observed that the contrast between forward and backward transmission coefficients is directly proportional with the determinant of the mode-port coupling matrix D. In this section, we show that this determinant

can be obtained in terms of the out-coupling losses of the optical modes. The energy-conservation relation $D^\dagger D = K_\mathrm{e}$ [33, 37] implies that:

$$|\det(D)|^2 = \det(K_\mathrm{e}) = \eta_1\kappa_1\eta_2\kappa_2, \tag{4.16}$$

where $\eta_1 = \kappa_{\mathrm{e}_1}/\kappa_1$ and $\eta_2 = \kappa_{\mathrm{e}_2}/\kappa_2$ represent the ratio of out-coupling to total losses for each mode. At the same time, the time-reversal symmetry requirement of the optical system, *i.e.* $CD^* = -D$ [33, 37], links the direct scattering matrix C to the mode-port coupling matrix D. As a result, we obtain a condition on their respective determinant that reads $\det(C)\det(D)^* = \det(D)$. Multiplying left and right with $\det(D)$ yields $\det(C)|\det(D)|^2 = (\det(D))^2$. Equation (4.16) now directly gives

$$\det(D) = \sqrt{\eta_1\eta_2\kappa_1\kappa_2}\det C. \tag{4.17}$$

Note that, in general, C is a unitary matrix with $|\det(C)| = 1$. In addition, by adjusting the evaluation point at the two ports one can properly choose the phase of $\det(C)$. For the systems we consider in section 4.5, we have chosen $\det(C) = -1$, which results in $\det(D) = \mathrm{i}\sqrt{\eta_1\eta_2\kappa_1\kappa_2}$. According to this relation a necessary condition for breaking reciprocity is that $\eta_1 \neq 0$ and $\eta_2 \neq 0$. This latter means that both optical modes should be coupled to the ports. A possible scenario that violates this condition is the presence of a dark state which is decoupled from the two ports of the system [38]. This is in fact a scenario that would arise when diagonalizing a system that consists of two modes that have equal symmetry with respect to the output channels, through which they would couple at finite rate κ_r. This is in accordance with the condition derived in section 4.2, where we derived that both optical modes should be (asymmetrically) coupled to the output ports.

4.4 Intermezzo: Fabry-Pérot model systems

In this section, we try to provide an intuitive understanding of the underlying physics involved in a nonreciprocal optomechanical system by considering two Fabry-Pérot models, in analogy with the Fabry-Pérot model with a movable mirror that is often used to describe a general (two-mode) optomechanical system. We refer to these two models as the end- and side-coupled structures, fig. 4.3a/c and fig. 4.3b/d, respectively, in analogy with their integrated photonic counterparts (see fig. 4.4). The difference between both structures is a direct light propagation path between the two input and output ports in fig. 4.3b/d, which is absent in fig. 4.3a/c. Taking the example of a red-detuned control frequency, it can directly be seen from eq. (4.12) that for both systems the mechanically-mediated hopping rate (mode-conversion at rate μ_m) from mode 1 to 2 reads $\mu_\mathrm{m}^{1\to2} = -g_1^* g_2/\Sigma_\mathrm{m}^+(\omega)$, while for the opposite process $\mu_\mathrm{m}^{2\to1} = -g_1 g_2^*/\Sigma_\mathrm{m}^+(\omega)$. At resonance and for $\Delta\phi = \pi/2$ ($g_2 = \mathrm{i}g_1$),

this coupling reduces to $\mu_{\mathrm{m}}^{2\to1} = |g_1||g_2|/(\Gamma_{\mathrm{m}}/2)$ and $\mu_{\mathrm{m}}^{1\to2} = -\mu_{\mathrm{m}}^{2\to1}$, which reveals that this optomechanically-mediated photon transfer path imprints an opposite phase on oppositely (from optical mode 1 to 2, or vice versa) travelling photons, effectively providing gyration. However, in order to obtain isolation this nonreciprocal mode transfer path needs to interfere with a second optical path.

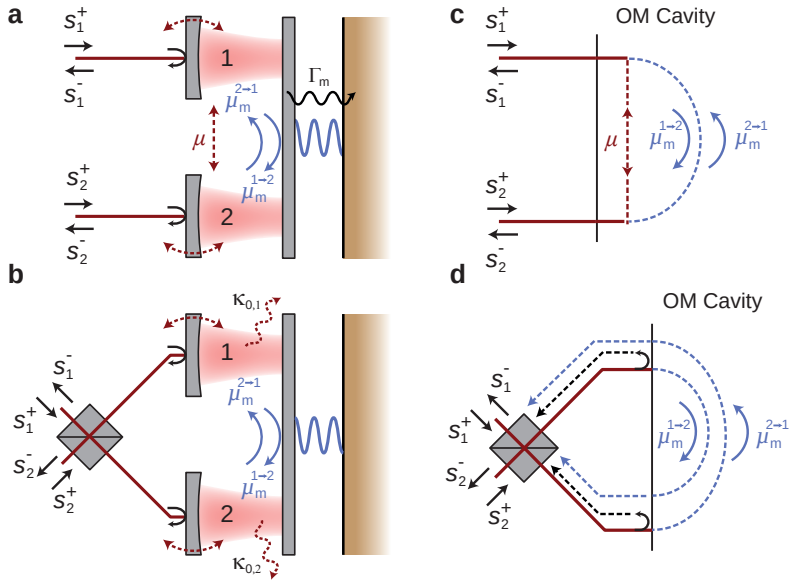

Figure 4.3: Fabry-Pérot models of nonreciprocal optomechanical systems. The mechanically mediated mode-conversion rate μ_{m} is in general nonreciprocal, imprinting opposite phases for photons hopping from optical mode 1 to 2, versus those hopping from mode 2 to 1. **a**/**c**, In the absence of a direct scattering path between port 1 and 2, and the absence of direct optical coupling ($\mu = 0$), the end-fire geometry operates as a nonreciprocal phase shifter. To obtain isolation, the path that experiences a nonreciprocal phase pickup as a result of mechanically mediated mode transfer needs to interfere with the direct mode coupling path (requiring $\mu \neq 0$). Optimal isolation can be achieved when the two interfering paths are balanced ($\mu = |\mu_{\mathrm{m}}|$). Note that in this scenario loss through the mechanical bath is required to achieve isolation, limiting the nonreciprocal bandwidth to twice the intrinsic mechanical linewidth. **b**/**d**, In contrast, in the presence of a direct-scattering path as common in a side-coupled geometry, isolation is achieved when the 'mechanically-mediated path' interferes with direct transmission between the ports. In this geometry, maximum isolation is achieved for $|g_1||g_2| \to \infty$. As in this system the nonreciprocal behaviour is fuelled by losses to the optical bath, the bandwidth is ultimately limited by the optical linewidth κ. The dashed lines in **c**/**d** indicate interfering optical paths.

To gain more insight on this interference condition, for now we treat the end-coupled system (fig. 4.3a/c) as two non-diagonalized degenerate optical modes

($\omega_1 = \omega_2$) in the presence of a direct mode-to-mode hopping (coupling) rate μ. In this geometry, it is the finite direct optical coupling ($\mu \neq 0$) that provides the additional path with which the mechanically-mediated path (μ_{m}) can interfere. If there is destructive interference between these two paths, there will be optical isolation. Critically, for complete destructive interference between the two paths, a careful match between hopping rates is required. Optimal isolation in the end-coupled geometry therefore occurs for $\mu = |\mu_{\mathrm{m}}|$, which is consistent with the condition derived in [30] following a different theoretical approach. At first sight, this result seems to suggest that it is possible to equally increase or decrease both μ and $|\mu_{\mathrm{m}}|$ to achieve ideal isolation. However, careful inspection of the underlying equations, as detailed in section 4.6, shows that there is an optimum value for μ that relates to the rate at which photons are lost through the mechanical loss channel.

In contrast, the side-coupled geometry (fig. 4.3b) in the absence of direct mode-to-mode coupling μ, can be seen as the end-coupled system of fig. 4.3a positioned in an optical interferometer that is tuned such that away from cavity resonance, light from port 1 constructively interferes in port 2 and vice versa. In this case, a direct propagation channel provides the path with which the mode-transfer processes can interfere that is *external* to the cavities. Considering the direct channel to be lossless, one can intuitively understand that complete destructive interference takes place when all the light entering the optomechanical system at cavity 1 exits at cavity 2. In other words, complete isolation is achieved for ideal mode-transfer, occurring for $|g_1||g_2| \to \infty$.

We conclude by noting that a theoretical model that uses diagonalized optical modes can be used to describe both models that were presented in this section. In the diagonalized description, with which we started in section 4.3, the full-scattering matrix S is found by inserting explicit expressions for the C and D matrices (eq. (4.13)). As a reminder, the C matrix describes direct port-to-port scattering, while the D matrix concerns the mode-port coupling. From fig. 4.3, we directly observe that the C matrices for the end-coupled and side-coupled situation should be different. After all, when operating off-resonance, the end-coupled geometry should be fully reflective, while there is direct port-to-port transmission in the side-coupled geometry. In the next sections we will derive the explicit C (and D) matrices for both scenarios. Afterwards, we then show how these matrices influence the resulting scattering parameters for the end- and side-coupled geometry.

4.5 System-specific C and D matrices

Moving towards full S-matrix expressions (completing eq. (4.13)) requires the derivation of the C and D matrices associated with the end-coupled and side-coupled geometries. To do this, consider the Fabry-Pérot models introduced in the previous section, but now modelled as abstract waveguide representations

sketched in fig. 4.4. On one hand, we can consider two coupled single mode optical cavities with a mode hopping rate μ (fig. 4.4, bottom row). Alternatively we can diagonalize the system and consider a single cavity to support two normal modes with frequency splitting 2μ (fig. 4.4, top row). This assumption, utilizing the two hybrid optical modes, simplifies the derivation of coupling matrix D, as symmetry arguments now allow us to easily determine the phase relation with which the two hybrid modes couple to the input and output ports. For the end-coupled geometry depicted in fig. 4.4a, for example, symmetry dictates $d_{11} = d_{21}$ (even mode) and $d_{12} = -d_{22}$ (odd mode).

We proceed by briefly repeating that energy-conservation and time-reversal symmetry impose stringent restrictions on the C and D matrices [33, 37], resulting in the relations $D^\dagger D = K_\mathrm{e}$ and $CD^* = -D$. Considering that the direct scattering matrix C in the end-coupled geometry reads

$$C = \begin{pmatrix} \mathrm{i} & 0 \\ 0 & \mathrm{i} \end{pmatrix}, \tag{4.18}$$

where the arbitrary phase of the reflection coefficient is chosen to ensure $\det(C) = -1$, we obtain

$$D = \frac{\exp(-\mathrm{i}\pi/4)}{\sqrt{2}} \begin{pmatrix} \sqrt{\eta_1\kappa_1} & -\sqrt{\eta_2\kappa_2} \\ \sqrt{\eta_1\kappa_1} & \sqrt{\eta_2\kappa_2} \end{pmatrix}. \tag{4.19}$$

In contrast, for the side-coupled geometry the direct path scattering matrix is given by

$$C = \begin{pmatrix} 0 & 1 \\ 1 & 0 \end{pmatrix}, \tag{4.20}$$

resulting in a D matrix that reads

$$D = \frac{1}{\sqrt{2}} \begin{pmatrix} \mathrm{i}\sqrt{\eta_1\kappa_1} & -\sqrt{\eta_2\kappa_2} \\ \mathrm{i}\sqrt{\eta_1\kappa_1} & \sqrt{\eta_2\kappa_2} \end{pmatrix}. \tag{4.21}$$

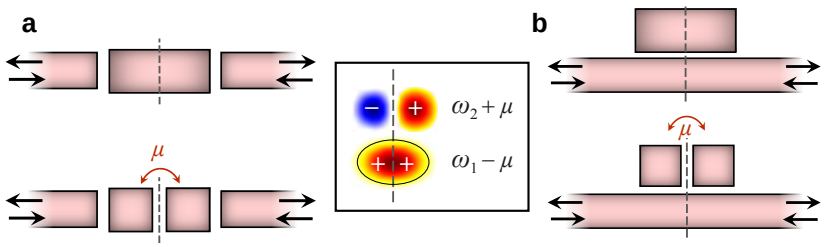

Figure 4.4: Integrated photonic geometries. **a**, End-coupled geometry and **b**, side-coupled geometry. The system can be composed of a single cavity with two modes (top), or two coupled single-mode cavities (bottom). The inset depicts the two hybrid optical modes with even and odd symmetry.

Together with eq. (4.13), we now have all the necessary components to describe the scattering properties of a nonreciprocal optomechanical system. Before finalizing this section we mention that for a ring resonator coupled sideways to a waveguide, which resembles a specific example of the side-coupled geometry, the formalism described here does not allow the use of clockwise a_{cw} and counterclockwise a_{ccw} travelling modes, as these by themselves are not reciprocal. Instead, for the experimental implementation studied in later chapters, we have to consider the even and odd standing modes, $a_1 = (a_{\mathrm{cw}} + a_{\mathrm{ccw}})/\sqrt{2}$ and $a_2 = (a_{\mathrm{cw}} - a_{\mathrm{ccw}})/\mathrm{i}\sqrt{2}$, as the optical mode basis. While in principle any choice of mode basis is possible (rewriting the formulas starting at eq. (4.1) accordingly) our current choice reveals the importance of the optomechanical transfer phases of g_1 and g_2 in creating an artificial magnetic field in all systems.

4.6 Conditions for isolation

In this section we focus on the conditions for (ideal) isolation. We note that nonreciprocal phase transmission could in principle also be studied, as the phase of the transmitted light is easily obtained by taking the argument of any of the following S-matrix elements. For both the end-coupled and side-coupled systems complete expressions for operation in the red- and blue-detuned regime will be given. However, our discussion here will mainly involve the red-detuned scenario. A blue-detuned control frequency is perfectly able to break reciprocity but, as a result of a Stokes scattering process, parametrically amplifies both the mechanical resonator and optical probe fields. The direct result of this amplification is a reduction of the nonreciprocal bandwidth. Furthermore, as any amplification process adds noise [39], using a red-detuned control frequency is typically the more preferred *modus operandi* for optomechanical nonreciprocal elements.

4.6.1 End-coupled geometry

For the end-coupled geometry, the off-diagonal scattering elements are found by inserting eqs. (4.18) and (4.19) in eq. (4.13), and read

$$s_{12} = \left[\frac{\eta_1 A_2 - \eta_2 A_1 \mp 2\mathrm{i}\sqrt{\eta_1\eta_2}\sqrt{\mathcal{C}_1\mathcal{C}_2}\sin(\Delta\phi)}{(\delta_1+\mathrm{i})(\delta_2+\mathrm{i})(\delta_\pm+\mathrm{i}) \mp ((\delta_2+\mathrm{i})\mathcal{C}_1 + (\delta_1+\mathrm{i})\mathcal{C}_2)}\right], \tag{4.22}$$

and

$$s_{21} = \left[\frac{\eta_1 A_2 - \eta_2 A_1 \pm 2\mathrm{i}\sqrt{\eta_1\eta_2}\sqrt{\mathcal{C}_1\mathcal{C}_2}\sin(\Delta\phi)}{(\delta_1+\mathrm{i})(\delta_2+\mathrm{i})(\delta_\pm+\mathrm{i}) \mp ((\delta_2+\mathrm{i})\mathcal{C}_1 + (\delta_1+\mathrm{i})\mathcal{C}_2)}\right], \tag{4.23}$$

where we defined

$$A_i = ((\delta_i+\mathrm{i})(\delta_\pm+\mathrm{i}) \mp \mathcal{C}_i)\,, \tag{4.24}$$

and, for completeness, the upper(lower) signs refer to a red(blue) detuned control field. In the remainder we only discuss the red-detuned scenario.

Using these expressions, it is worthwhile to first consider a scenario where light propagation in one direction is completely blocked. To find a compact result, we define a total cooperativity $\mathcal{C} \equiv \mathcal{C}_1 + \mathcal{C}_2$ and assume ideal conditions. This involves both modes to be equally driven ($2\mathcal{C}_1 = 2\mathcal{C}_2 = \mathcal{C}$, $\Delta_i \approx -\Omega_\mathrm{m}$) with ideal phase difference ($\Delta\phi = -\pi/2$), and that their coupling to connecting waveguides is similar ($\eta_1 = \eta_2 = \eta$, impedance matching). Moreover, we assume that both modes have equal loss rate such that $\kappa_1 = \kappa_2 = \kappa$ and that we are on resonance with the mechanical resonance ($\omega = \Omega_\mathrm{m}$). After inserting a normal-mode frequency splitting of 2μ, such that $\delta_1 = -\delta_2 = \mu/\kappa$, light propagation from port 2 to port 1 ($s_{12} = 0$) is completely blocked for $2\mu/(\kappa/2) = \mathcal{C}$. This corresponds to the direct optical coupling rate μ being equal to the mechanically-mediated coupling rate $|g_1 g_2/\Gamma_\mathrm{m}|$. Notably, because we assumed $\mathcal{C}_1 = \mathcal{C}_2$, this is equivalent to the condition

$$\frac{2\mu}{\kappa} = \mathcal{C}_1 \wedge \frac{2\mu}{\kappa} = \mathcal{C}_2. \tag{4.25}$$

According to these relations and consistent with the discussion in section 4.4, the complete rejection of the backward propagating probe thus requires balancing the normalized mode splitting and cooperativity (mechanically-mediated mode transfer). At the same time, this condition bounds s_{21} to

$$|s_{21}(\omega = \Omega_\mathrm{m})| = \eta \frac{8\mathcal{C}}{(\mathcal{C}+2)^2}. \tag{4.26}$$

This relation directly provides the important result that maximum transmission is obtained for $\mathcal{C} = 2$, resulting in $\max(|s_{21}| = \eta)$. Complete forward transmission and zero insertion loss can thus be achieved when the optical modes have zero absorption, *i.e.,* $\kappa_{0,i} = 0$ or equivalently $\eta = 1$. This is intuitively understood bearing in mind that light needs to be transferred from one optical mode to another, and any loss in these resonators thus causes non-unity transmission.

To get a feeling for the lineshapes that describe nonreciprocal transmittance, we plot $|s_{21}|^2$ (orange line) and $|s_{12}|^2$ (blue line) in fig. 4.5 for the ideal cooperativity $\mathcal{C} = 2$. The different panels are obtained for different normalized mode-splittings $2\mu/\kappa$. As we can see from fig. 4.5b, where we assume the ideal scenario of $2\mu/\kappa = \mathcal{C}_1 = 1$, light in the backwards direction (blue line) is fully blocked while light in the forward direction (orange line) is completely transmitted. Non-ideal transmittance contrast (isolation) is observed when the mode splitting is too small (fig. 4.5a) or too large (fig. 4.5c). Figure 4.6a explores the isolation, or transmittance contrast, in a contour map, varying the normalized mode-splitting (horizontal axis) and cooperativity (vertical axis) for $\eta = 1$, which clearly shows that optimal contrast is indeed obtained for $\mathcal{C}_1 = \mathcal{C}_2 = 2\mu/\kappa = 1$.

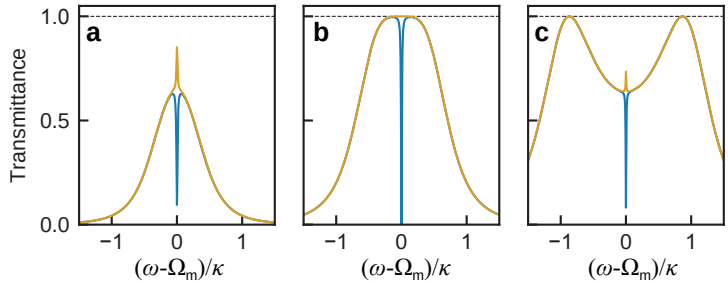

Figure 4.5: Transmittance for the end-coupled structure for varying mode splitting. We plot the transmittance (assuming equivalent cavities) for the forward ($|s_{21}|^2$, orange) and backward ($|s_{12}|^2$, blue) direction for the 'ideal' cooperativity $\mathcal{C} = 2$ (such that $\mathcal{C}_1 = \mathcal{C}_2 = 1$). The panels are discriminated based on the normalized mode splitting $2\mu/\kappa$. For **a**/**b**/**c**, this splitting is equal to 0.5/1/2, respectively. In panel **b** we observe the ideal behaviour, for $2\mu/\kappa = \mathcal{C}_1 = 1$, that was described in the text: unity transmission in the forward direction, while light in the backward direction is fully blocked.

Although we established that the optomechanical system can provide *optical* isolation, this is in some way remarkable when taking into account that ideal isolation is only obtained in the absence of optical losses. The subsequent question to ask is where the unidirectionally blocked light is lost from the system. To investigate this in more detail, we plot the transmittance ($|s_{21}|^2$, orange line and $|s_{12}|^2$, blue line) as a function of normalized probe frequency in fig. 4.6b for the optimal parameters. Under these conditions, light propagation in both directions is mediated by the susceptibility of the optical modes (clearly visible in fig. 4.5b), essentially yielding a passband over a bandwidth commensurate with κ. However, we can observe from fig. 4.6b that there is a narrow bandwidth ($2\Gamma_\mathrm{m}$) over which the backward probe is rejected. This means that the mechanical bath is responsible for unidirectional dissipation.

In fact, for any (general) two-resonator system the cooling rate Γ_cool, which is the rate at which an optical bath can extract phonons from the coupled (at rate g_1) mechanical resonator, is given by $\Gamma_\mathrm{cool} = 4|g_1|^2/\kappa$ [27]. Vice-versa, the mechanical resonator is capable of dissipating optical photons from an optical resonator into the mechanical bath at rate $4|g_1|^2/\Gamma_\mathrm{m}$. As intrinsic optical losses in the ideal scenario are absent, this must mean that $\kappa = 4|g_1|^2/\Gamma_\mathrm{m}$, directly yielding $\mathcal{C}_1 = 1$. This condition is completely equivalent to the requirement on $\mathcal{C}_1$ and $\mathcal{C}_2$ as retrieved by direct assessment of the scattering matrix elements, and can be seen as if the optical mode is unidirectionally 'critically coupled' to the mechanical bath. The simple argument provided here thus proves that it is indeed the mechanical bath that provides the necessary losses yielding unidirectional transmission. The effective nonreciprocal bandwidth of $2\Gamma_\mathrm{m}$ is a direct consequence of optical cooling, introduced in section 1.5.3, of the mechanical resonator. Stressing that only photons leaving via the optical bath

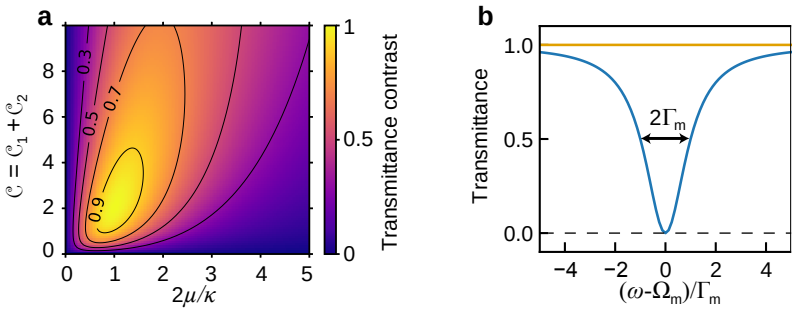

Figure 4.6: Transmittance contrast in the end-coupled geometry. **a**, Maximum transmittance contrast in the end-coupled structure as a function of the normalized mode splitting $2\mu/\kappa$, and multiphoton cooperativity $\mathcal{C}$. Optimal isolation is achieved for $\mathcal{C}_1 = \mathcal{C}_2 = 2\mu/\kappa = 1$. **b**, For these optimal parameters, light in both the forward (orange) and backward (blue) direction is transmitted over the optical bandwidth. Only in a narrow bandwidth, corresponding to the twice the mechanical linewidth, is backwards travelling light rejected (lost in the mechanical bath), resulting in optical isolation. The black dashed line indicates 0 transmittance.

contribute to this cooling, which in the scenario considered here is half of the total photons, the effective linewidth is given by $\Gamma_{\text{eff}} = \Gamma_m(1 + \mathcal{C}/2) = 2\Gamma_m$.

Summarizing, we have shown that it is the coupling to the mechanical bath [18, 19] that provides the required losses to block propagation in the backward direction in the end-coupled geometry. This is visible in fig. 4.6b, where in the absence of a pump laser, the end-coupled geometry yields a pass band for light with a bandwidth given by the optical linewidth. Although the considered end-coupled geometry has the benefit of reaching optimal isolation at a relatively low cooperativity $\mathcal{C}_1 = \mathcal{C}_2 = 1$, the loss mechanism in this specific situation directly limits the isolation bandwidth to $2\Gamma_m$.

4.6.2 Side-coupled geometry

Analogous to the previous section, off-diagonal scattering matrix elements are obtained by insertion of eqs. (4.20) and (4.21) into eq. (4.13), yielding

$$s_{12} = 1 - \mathrm{i}\left[\frac{\eta_2 A_1 + \eta_1 A_2 \mp 2\sqrt{\eta_1\eta_2}\sqrt{\mathcal{C}_1\mathcal{C}_2}\sin(\Delta\phi)}{(\delta_1 + \mathrm{i})(\delta_2 + \mathrm{i})(\delta_\pm + \mathrm{i}) \mp (\delta_2 + \mathrm{i})\mathcal{C}_1 \mp (\delta_1 + \mathrm{i})\mathcal{C}_2}\right], \tag{4.27}$$

$$s_{21} = 1 - \mathrm{i}\left[\frac{\eta_2 A_1 + \eta_1 A_2 \pm 2\sqrt{\eta_1\eta_2}\sqrt{\mathcal{C}_1\mathcal{C}_2}\sin(\Delta\phi)}{(\delta_1 + \mathrm{i})(\delta_2 + \mathrm{i})(\delta_\pm + \mathrm{i}) \mp (\delta_2 + \mathrm{i})\mathcal{C}_1 \mp (\delta_1 + \mathrm{i})\mathcal{C}_2}\right]. \tag{4.28}$$

Again, these expressions are greatly simplified assuming equal cavities ($\kappa_1 = \kappa_2 = \kappa, \eta_1 = \eta_2 = \eta$) and resonant probe excitation ($\omega = \pm\Omega_m$). In addition, we assume that both modes are pumped with the same number of cavity photons ($\mathcal{C}_1 = \mathcal{C}_2 = \mathcal{C}/2$) and with $\Delta\phi = \pi/2$. Also considering that the absolute value

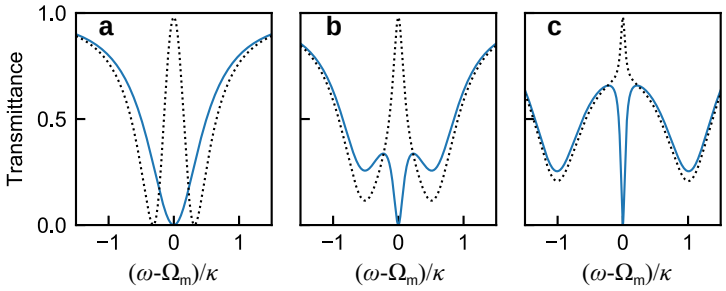

Figure 4.7: Mode splitting. We plot $|s_{21}|^2$ (dotted black line) and $|s_{12}|^2$ (blue solid line) for a red-detuned control field ($\Delta_i \approx -\Omega_\mathrm{m}$, $\Delta\phi = \pi/2$), $\eta = 0.5$ and a cooperativity $\mathcal{C} = 100$. **a**, For degenerate modes we observe an induced transparency peak for the forward direction $|s_{21}|^2$, while the backward direction $|s_{12}|^2$ is completely decoupled from the mechanical resonator. **b**/**c**, In the presence of normal mode splitting (**b**: $2\mu/\kappa = 1$, **c**: $2\mu/\kappa = 2$) probe signals entering the system from both directions experience mechanically-mediated photon transfer. Critically, because we enforce the optimal drive phase of $\Delta\phi = \pi/2$, optimal nonreciprocity is maintained also in the presence of mode-splitting. We note that the simple relation describing the effective bandwidth of an optomechanically induced transparency peak: $\Gamma_\mathrm{eff} = \Gamma_\mathrm{m}(1 + \mathcal{C})$, is strictly only valid for $\mu = 0$. Especially for the situation considered in **c** we observe that this simple relation does not hold any more.

of both 'normalized detunings' δ_1 and δ_2 is equal, such that $|\delta_1| = |\delta_2| \equiv \beta$, we obtain

$$s_{12} = 1 - \eta \frac{2 \pm 2\mathcal{C}}{1 \pm \mathcal{C} + \beta^2}, \tag{4.29}$$

$$s_{21} = 1 - \eta \frac{2}{1 \pm \mathcal{C} + \beta^2}. \tag{4.30}$$

For the condition that both modes are equally split, β simplifies to $\beta = 2\mu/\kappa$, where again 2μ is the frequency splitting between the optical normal modes. In fig. 4.7 we plot $|s_{21}|^2$ (black dotted lines) and $|s_{12}|^2$ (blue solid line) for a red-detuned control field ($\Delta_i \approx -\Omega_\mathrm{m}$) using eqs. (4.30) and (4.29) for $\eta = 0.5$, a cooperativity $\mathcal{C} = 100$ and three different normalized detunings. For degenerate ($2\mu/\kappa = 0$) optical modes as shown in fig. 4.7a, we observe an optomechanically induced transparency peak for $|s_{21}|^2$ that reaches almost unity transmittance. In contrast, the reverse direction $|s_{12}|^2$ lacks this feature, and is 'simply' critically coupled (due to $\eta = 0.5$) and thus displays zero transmittance on resonance. Interestingly, introducing mode splitting, which in fig. 4.7b(c) is given by $2\mu/\kappa = 1(2)$, yields a mechanically-induced peak in the transmittance for *both* $|s_{21}|^2$ and $|s_{12}|^2$. This can be interpreted as if probe signals entering from both ports interact with the mechanical resonator, and is related to the intracavity field at the probe frequency that exhibits non-trivial behaviour due to this splitting. The origin of this effect is discussed in section 5.2 in more detail, and experimental results confirming this effect are

presented in, for example, section 5.4.3.

Using eqs. (4.30) and (4.29) and again assuming critical coupling ($\eta = 0.5$) we find an expression for difference in transmittance for forward and backward probes that reads

$$\Delta T = |s_{21}|^2 - |s_{12}|^2 = \frac{\mathcal{C}(\mathcal{C} + 2\beta^2)}{(1 + \mathcal{C} + \beta^2)^2}, \tag{4.31}$$

which can be further simplified to $\Delta T = (\mathcal{C}/(\mathcal{C}+1))^2$ for the case of degenerate modes ($\beta = 0$). This simplified expression is equal to the height of an optomechanically induced transparency peak for a critically coupled waveguide (fig. 4.7a) as derived in [40]. More importantly, it shows that the contrast between forward and backward transmittance monotonically increases with cooperativity and asymptotically approaches unity for $\mathcal{C} \to \infty$. To illustrate this, fig. 4.8a plots the transmittance contrast ΔT as a function of cooperativity and normalized mode-splitting, which clearly shows the requirement on high $\mathcal{C}$ to obtain maximum contrast at negligible insertion loss. Operating at such high $\mathcal{C}$ has the (very) beneficial advantage that the total nonreciprocal bandwidth also increases (to $\Gamma_{\text{eff}} = \Gamma_{\text{m}}(1 + \mathcal{C})$ in this case), as depicted in fig. 4.8b, which is a direct result of optomechanical cooling of the mechanical resonator when the control laser is tuned to the red motional sideband of the cavity mode [41].

To highlight the difference between the current side-coupled situation and the previous section, it is worth exploring a scenario with no mechanical dis-

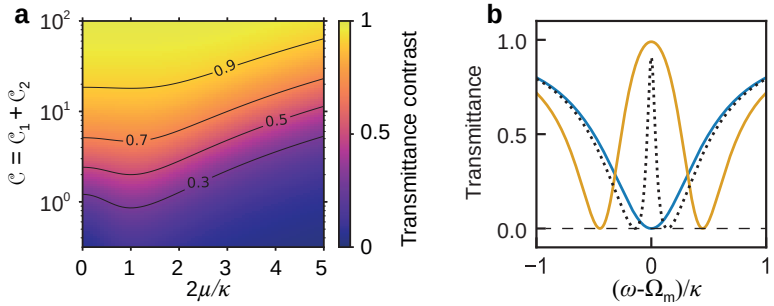

Figure 4.8: Transmittance contrast in the side-coupled geometry. **a**, Maximum transmittance contrast in the side-coupled structure as a function of the normalized mode splitting $2\mu/\kappa$ and multiphoton cooperativity $\mathcal{C}$. In contrast to the end-coupled geometry, there is no single optimum for both values. Instead, higher cooperativities always lead to lower insertion losses and higher transmittance contrast. Interestingly, for $2\mu/\kappa = 1$ both the optical and mechanical bath contribute to the suppression of unwanted light, benefiting the total contrast for this particular splitting. **b**, We plot the frequency dependent transmittance in the forward direction for a cooperativity of $\mathcal{C} = 200(20)$ with orange solid line(black dotted line) and the backward direction (blue solid line), for zero mode-splitting. For higher $\mathcal{C}$, the insertion loss is reduced and the nonreciprocal bandwidth increased. The black dashed line indicates zero transmittance.

sipation. According to eqs. (4.29) and (4.30), the asymptotic limit $\Gamma_m \to 0$ or equivalently $\mathcal{C} \to \infty$, results in $s_{12} = 1 - 2\eta$, while $s_{21} \to 1$. Therefore, this system can operate as an isolator as long as $\eta \neq 1$, *i.e.* as long as internal optical losses exist. Hence, the presence of optical loss leads to zero transmission. This is in strong contrast to the previously discussed end-coupled geometry, where mechanical loss blocks light in the unwanted propagation direction and the optical loss should be as small as possible.

Summarizing, isolation at negligible insertion loss in the side-coupled geometry is possible only at very high cooperativities. Importantly, with a red-detuned control laser, optical cooling of the mechanical mode at these high cooperativities leads to the benefit of an increased nonreciprocal bandwidth that is ultimately limited by the optical linewidth [42].

4.7 Conclusion

In this chapter, we developed a theoretical formalism describing the requirements for nonreciprocal light transmission in a three-mode optomechanical system. In particular, we pointed out an important distinction between the working principle of two optomechanical systems that can achieve nonreciprocal light transmission. For the side-coupled geometry it is optical loss that leads to unidirectional dissipation of energy. On the contrary, in the end-coupled geometry it is mechanical loss that causes dissipation for the unwanted propagation direction, and optical loss should be as low as possible. As a result, isolation at negligible insertion loss in the side-coupled geometry is achieved at very high cooperativities, resulting in a bandwidth ultimately limited by the optical linewidth [42]. Instead, the different loss mechanism in the end-coupled geometry leads to optimal isolation at much lower cooperativities, but at the cost of reduced bandwidths. Because our model does not rely on a specific implementation, it provides useful handles for the design of a variety of nonreciprocal systems.

References

[1] L. Deák, and T. Fülöp, *Reciprocity in quantum, electromagnetic and other wave scattering*, Ann. Phys. (N. Y). **327**, 1050 (2012).

[2] D. Jalas, et al., *What is – and what is not – an optical isolator*, Nat. Photonics **7**, 579 (2013).

[3] J. E. Geusic, and H. E. D. Scovil, *A unidirectional traveling-wave optical maser**, Bell Syst. Tech. J. **41**, 1371 (1962).

[4] L. J. Aplet, and J. W. Carson, *A Faraday effect optical isolator*, Appl. Opt. **3**, 544 (1964).

[5] M. Shirasaki, and K. Asama, *Compact optical isolator for fibers using birefringent wedges*, Appl. Opt. **21**, 4296 (1982).

[6] L. Bi, et al., *On-chip optical isolation in monolithically integrated non-reciprocal optical resonators*, Nat. Photonics **5**, 758 (2011).

[7] C. G. Poulton, et al., *Design for broadband on-chip isolator using stimulated Brillouin scattering in dispersion-engineered chalcogenide waveguides*, Opt. Express **20**, 21235 (2012).

[8] D. L. Sounas, C. Caloz, and A. Alù, *Giant non-reciprocity at the subwavelength scale using angular momentum-biased metamaterials*, Nat. Commun. **4**, 2407 (2013).

[9] E. Li, B. J. Eggleton, K. Fang, and S. Fan, *Photonic Aharonov-Bohm effect in photon-phonon interactions*, Nat. Commun. **5**, 3225 (2014).

[10] L. D. Tzuang, K. Fang, P. Nussenzveig, S. Fan, and M. Lipson, *Non-reciprocal phase shift induced by an effective magnetic flux for light*, Nat. Photonics **8**, 701 (2014).

[11] N. A. Estep, D. L. Sounas, J. Soric, and A. Alù, *Magnetic-free non-reciprocity and isolation based on parametrically modulated coupled-resonator loops*, Nat. Phys. **10**, 923 (2014).

[12] D. L. Sounas, and A. Alù, *Angular-momentum-biased nanorings to realize magnetic-free integrated optical isolation*, ACS Photonics **1**, 198 (2014).

[13] K. M. Sliwa, et al., *Reconfigurable Josephson circulator/directional amplifier*, Phys. Rev. X **5**, 041020 (2015).

[14] X. Guo, C.-L. Zou, H. Jung, and H. X. Tang, *On-chip strong coupling and efficient frequency conversion between telecom and visible optical modes*, Phys. Rev. Lett. **117**, 123902 (2016).

[15] C. Sayrin, et al., *Nanophotonic optical isolator controlled by the internal state of cold atoms*, Phys. Rev. X **5**, 041036 (2015).

[16] J. Kim, M. C. Kuzyk, K. Han, H. Wang, and G. Bahl, *Non-reciprocal Brillouin scattering induced transparency*, Nat. Phys. **11**, 275 (2015).

[17] C.-H. Dong, et al., *Brillouin-scattering-induced transparency and non-reciprocal light storage*, Nat. Commun. **6**, 6193 (2015).

[18] L. Ranzani, and J. Aumentado, *Graph-based analysis of nonreciprocity in coupled-mode systems*, New J. Phys. **17**, 023024 (2015).

[19] A. Metelmann, and A. A. Clerk, *Nonreciprocal photon transmission and amplification via reservoir engineering*, Phys. Rev. X **5**, 021025 (2015).

[20] M. Scheucher, A. Hilico, E. Will, J. Volz, and A. Rauschenbeutel, *Quantum optical circulator controlled by a single chirally coupled atom*, Science **354**, 1577 (2016).

[21] P. Roushan, et al., *Chiral ground-state currents of interacting photons in a synthetic magnetic field*, Nat. Phys. **13**, 146 (2017).

[22] F. Lecocq, et al., *Nonreciprocal microwave signal processing with a field-programmable Josephson amplifier*, Phys. Rev. Appl. **7**, 024028 (2017).

[23] N. R. Bernier, et al., *Nonreciprocal reconfigurable microwave optomechanical circuit*, Nat. Commun. **8**, 604 (2017).

[24] Z. Yu, and S. Fan, *Complete optical isolation created by indirect interband photonic transitions*, Nat. Photonics **3**, 91 (2009).

[25] K. Fang, Z. Yu, and S. Fan, *Realizing effective magnetic field for photons by controlling the phase of dynamic modulation*, Nat. Photonics **6**, 782 (2012).

[26] K. Fang, Z. Yu, and S. Fan, *Photonic Aharonov-Bohm effect based on dynamic modulation*, Phys. Rev. Lett. **108**, 153901 (2012).

[27] M. Aspelmeyer, T. J. Kippenberg, and F. Marquardt, *Cavity optomechanics*, Rev. Mod. Phys. **86**, 1391 (2014).

[28] Z. Shen, et al., *Experimental realization of optomechanically induced non-reciprocity*, Nat. Photonics **10**, 657 (2016).

[29] F. Ruesink, M.-A. Miri, A. Alù, and E. Verhagen, *Nonreciprocity and magnetic-free isolation based on optomechanical interactions*, Nat. Commun. **7**, 13662 (2016).

[30] K. Fang, et al., *Generalized non-reciprocity in an optomechanical circuit via synthetic magnetism and reservoir engineering*, Nat. Phys. **13**, 465 (2017).

[31] G. A. Peterson, et al., *Demonstration of efficient nonreciprocity in a microwave optomechanical circuit*, Phys. Rev. X **7**, 031001 (2017).

[32] S. Barzanjeh, et al., *Mechanical on-chip microwave circulator*, arXiv 1706.00376 (2017).

[33] W. Suh, Z. Wang, and S. Fan, *Temporal coupled-mode theory and the presence of non-orthogonal modes in lossless multimode cavities*, IEEE J. Quantum Electron. **40**, 1511 (2004).

[34] S. J. M. Habraken, K. Stannigel, M. D. Lukin, P. Zoller, and P. Rabl, *Continuous mode cooling and phonon routers for phononic quantum networks*, New J. Phys. **14**, 115004 (2012).

[35] X.-W. Xu, and Y. Li, *Optical nonreciprocity and optomechanical circulator in three-mode optomechanical systems*, Phys. Rev. A **91**, 053854 (2015).

[36] C. Gardiner, and P. Zoller, *Quantum noise: a handbook of Markovian and non-Markovian quantum stochastic methods with applications to quantum optics* (Springer Science & Business Media, 2004), 3rd ed.

[37] H. A. Haus, *Waves and fields in optoelectronics* (Prentice-Hall, 1984).

[38] C. M. Gentry, and M. A. Popović, *Dark state lasers*, Opt. Lett. **39**, 4136 (2014).

[39] A. A. Clerk, M. H. Devoret, S. M. Girvin, F. Marquardt, and R. J. Schoelkopf, *Introduction to quantum noise, measurement, and amplification*, Rev. Mod. Phys. **82**, 1155 (2010).

[40] S. Weis, et al., *Optomechanically induced transparency*, Science **330**, 1520 (2010).

[41] A. Schliesser, R. Rivière, G. Anetsberger, O. Arcizet, and T. J. Kippenberg, *Resolved-sideband cooling of a micromechanical oscillator*, Nat. Phys. **4**, 415 (2008).

[42] M. Hafezi, and P. Rabl, *Optomechanically induced non-reciprocity in microring resonators*, Opt. Express **20**, 7672 (2012).

Chapter 5

Optomechanically Induced Isolation and Unidirectional Amplification

Nonreciprocal components, such as isolators and circulators, provide highly desirable functionalities for optical circuitry. This motivates the active investigation of mechanisms that break reciprocity, and pose alternatives to magneto-optic effects in on-chip systems. In this chapter, we use optomechanical interactions to strongly break reciprocity in a compact system. We do so in a silica microtoroid optomechanical resonator and use quantitative heterodyne spectroscopy to demonstrate up to 10 dB optical isolation at telecom wavelengths. In addition, we show that nonreciprocal transmission is preserved for nondegenerate modes and demonstrate nonreciprocal parametric amplification. These results open a route to exploiting various nonreciprocal effects in optomechanical systems in different electromagnetic and mechanical frequency regimes, including optomechanical metamaterials with topologically non-trivial properties.

5.1 Introduction

Lorentz reciprocity stipulates that electromagnetic wave transmission is invariant under a switch of source and observer [1], and its implications widely permeate physics. To violate reciprocity and obtain asymmetric transmission, suitable forms of time-reversal symmetry breaking are required [2]. In the previous chapter, we explored how an optomechanical system of two optical modes parametrically coupled to a joint mechanical mode can be used to break reciprocity. In these optomechanical systems, pronounced optical time-modulation [3, 4] can be realized, where the displacement x of a mechanical resonator alters the resonance frequency ω_c of the optical cavity modes [5]. Simultaneously, light can control the mechanical motion through radiation pressure, removing the need for external modulation. In recent years, this interaction's dynamics has been exploited for mechanical cooling [6–8], optical amplification [9], wavelength conversion [10–12] and optomechanically induced transparency [13] (OMIT). Moreover, Hafezi and Rabl [14] theoretically predicted that optomechanical interactions in ring resonators can enable nonreciprocal responses, and associated asymmetric cavity spectra were recently observed [15–17]. In other recent work, it was recognized that the mechanically-mediated signal transfer between two optical modes can be made nonreciprocal with suitable optical driving [18, 19], a mechanism that enables phonon circulators and networks with topological phases for sound and light [18, 20, 21].

In this chapter we discuss the experimental implementation of an optomechanical system that enables us to break Lorentz reciprocity. We achieve this using a microtoroid ring resonator, a frequently used optomechanical system that here is evanescently coupled to a feeding waveguide, placing the system into the category of side-coupled geometries discussed in the previous chapter. Importantly, we show that this experimental implementation requires only a single control frequency to optimally drive both optical modes in the microtoroid with a phase difference of $\Delta\phi = \pi/2$. As established in the previous chapter, this is a necessary ingredient to be able to observe nonreciprocal light transmission. Using this platform, we achieve 10 dB of optical isolation and demonstrate that the system can also act as a nonreciprocal optomechanical amplifier. In addition, we show that nearly optimal drive conditions are maintained in the presence of non-degenerate modes, and that strongly nonreciprocal light transmission in such systems is thus preserved.

5.2 The optimal drive condition in a ring resonator

In section 4.3, we derived that nonreciprocal optical transmission in a three-mode optomechanical system (fig. 5.1a) can be realized when both optomechanical transitions (couplings) are driven by a control field in quadrature.

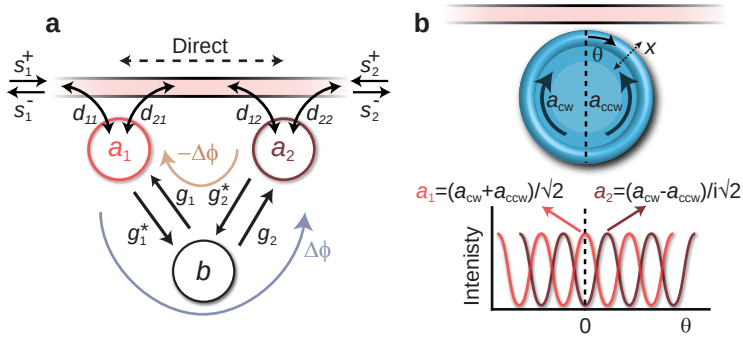

Figure 5.1: Nonreciprocity in a multimode optomechanical system. **a**, General description: the optical modes (a_1, a_2) are coupled to a mechanical mode b with enhanced optomechanical coupling rates g_1 and g_2. The path $a_1 \rightarrow b \rightarrow a_2$ picks up a phase $\Delta\phi = \arg(g_2) - \arg(g_1)$ that is opposite to that of the reversed path $a_2 \rightarrow b \rightarrow a_1$. Two input/output ports (s_1 and s_2) are coupled to the optical modes with rates d_{ij}. Interfering both paths with direct scattering through the waveguide (indicated by the black dashed arrow) can build an optical isolator. **b**, A ring resonator supports even and odd optical modes (a_1, a_2), superpositions of clockwise (a_{cw}) and counterclockwise (a_{ccw}) propagating modes. As the two modes are $\pi/2$ out of phase with respect to a wave propagating in the waveguide, a control field incident from a single input port fulfils the optimal driving conditions to break reciprocity. The graph sketches the spatial intensity profile of the two modes along the rim of the ring resonator as a function of the angle θ with respect to the dashed line.

Interestingly, this requirement is readily met in ring resonators, such as the silica microtoroid [22] studied here. This well-known optomechanical system supports a mechanical radial breathing mode coupled to an even and odd optical standing wave mode [23], both a superposition of the clockwise and counterclockwise propagating modes (fig. 5.1b). Considering a ring resonator, a control beam incident through an evanescently coupled waveguide excites an equal superposition of even and odd modes with $\pi/2$ phase difference [24], such that the requirement on the phase of the control field to maximally break reciprocity is automatically fulfilled. It is the interference between a direct pathway (fig. 5.1a) with the resonant path (that collects a nonreciprocal π phase shift) that enables ideal isolation under appropriate conditions.

Our choice of the even and odd basis (in contrast to the clockwise and counterclockwise basis considered in other work [14, 15, 17]) immediately reveals the role of a nonreciprocal phase in intermode coupling. As a result, our model unifies the description of ring resonator systems discussed here and various geometries studied by other groups [25–28]. Moreover, consider that the incident control field excites an intracavity field that is the coherent sum of the even and odd mode. Under the appropriate bias condition this total cavity field is given by $a_1 + \mathrm{i}a_2$. Performing this summation shows that the intracavity field propagates with a specific handedness (clockwise or counterclockwise). As a

result, the cavity field at the control frequency carries angular momentum. This interesting notion allows one to speculate about the equivalence of, on the one hand, angular momentum biasing [29–31], and, on the other hand, the biasing of intermode transfer as we investigate here. The relevance of effective optical control momentum in the system can be recognized as well by considering what happens microscopically in the ring resonator: When control and probe beam co-propagate, the intracavity field exerts a fluctuating (at the beat frequency) and spatially extended radiation pressure force on the boundaries of the ring that drives the mechanical resonance. In strong contrast, when the control and probe beam counter-propagate, the intracavity field represents a standing wave mode that slowly rotates (at the 'beat' frequency) inside the ring such that the resulting (net) force over the entire cavity boundary is zero. As a result, the mechanical resonator is not driven in the latter scenario.

To investigate the resilience of the optimal drive phase ($\Delta\phi = \pi/2$) against the presence of possible mode-splitting, we use the model developed in chapter 4 and consider a single drive field with amplitude $\bar{s}_{\rm in}$ incident through port 1. The relative phase with which modes a_1 and a_2 are driven is found from

$$\begin{pmatrix} a_1 \\ a_2 \end{pmatrix} = \begin{pmatrix} \Sigma_{\rm o_1}^{-1} & 0 \\ 0 & \Sigma_{\rm o_2}^{-1} \end{pmatrix} D^{\rm T} \begin{pmatrix} \bar{s}_{\rm in} \\ 0 \end{pmatrix} \overset{\omega=0}{=} -\frac{\bar{s}_{\rm in}}{\sqrt{2}} \begin{pmatrix} \sqrt{\eta_1\kappa_1}/(\bar{\Delta}_1 + {\rm i}\kappa_1/2) \\ {\rm i}\sqrt{\eta_2\kappa_2}/(\bar{\Delta}_2 + {\rm i}\kappa_2/2) \end{pmatrix}. \quad (5.1)$$

Here $D^{\rm T}$ is the transpose of the D matrix for the side-coupled geometry (eq. (4.21)), and the matrix in front of $D^{\rm T}$ carries the susceptibilities of both

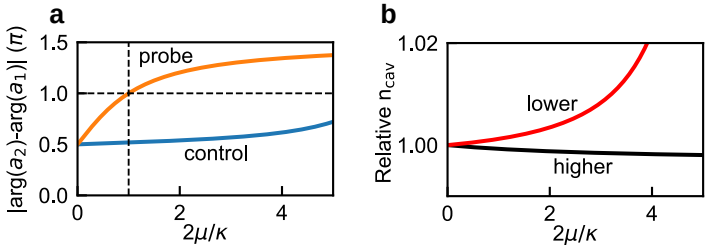

Figure 5.2: Drive phase for control and probe fields. a/b, For $\Omega_{\rm m}/\kappa = 3$ and as a function of normalized mode-splitting, panel **a** displays the phase difference with which optical mode a_1 and a_2 are driven for a red-detuned control field (blue line) and resonant ($\omega = \Omega_{\rm m}$) probe field (orange line). Clearly, for small mode-splitting, the ideal condition of $\Delta\phi = \pi/2$ for the control field is maintained. In strong contrast, probe excitation in the presence of mode splitting leads to a rapid departure from this condition. Importantly, this results in intracavity *probe* field components travelling both clockwise and counterclockwise with respect to the incident probe and control fields. **b**, Relative number of intracavity photons $n_{\rm cav}$ at the control frequency for a red-detuned control beam. Lower(higher): lower(higher) frequency optical mode. For a red-detuned control, the lower frequency mode is more resonant, leading to a strong increase of $n_{\rm cav}$ with respect to the higher frequency optical mode. Normalization is performed with respect to number of cavity photons for degenerate modes.

optical modes. This result reveals that for large detuning $|\bar{\Delta}_{1,2}| \gg \kappa_{1,2}$ (which applies to a detuned control field), the optimal phase difference $\Delta\phi = \pi/2$ with which both modes are driven is indeed automatically obtained. It is this phase that is directly reflected in the enhanced complex optomechanical coupling rates g_1 and g_2. The change with respect to this optimum of $\pi/2$ is given in fig. 5.2a (blue line) as a function of normalized mode-splitting for a certain choice of sideband factor $\Omega_{\mathrm{m}}/\kappa = 3$. This figure shows that for moderate splitting, the optimal phase difference of $\pi/2$ with which both optical modes are driven is maintained. In contrast, the orange curve in fig. 5.2a shows that the phase difference for an incident probe beam ($\omega = \Omega_{\mathrm{m}}$) quickly deviates from this optimum for non-degenerate modes. Interestingly, this means that for non-degenerate modes the intracavity field at the *probe* frequency (which is now only approximately given by $a_1 + \mathrm{i}a_2$) also contains fields propagating opposite to the control and probe beams in the waveguide. This results in the peculiar effect that incident probe beams co-propagating and counter-propagating to the control beam both interact with the mechanical resonator. In sections 5.4.3 and 6.4.2 we experimentally demonstrate that in such a situation, probe fields entering from opposite directions experience opposite mechanically-induced effects. For example, the 'backwards' travelling probe experiences optomechanically induced absorption, while the 'forwards' probe exhibits an induced transparency peak. This ensures that for non-degenerate modes optimal nonreciprocal light transmission is maintained. We conclude this section by noting that both optical modes are driven with an equal number of intracavity *control* photons for small mode splitting (fig. 5.2b). This important condition can be interpreted as if the paths $a_1 \leftrightarrow b$ and $a_2 \leftrightarrow b$ are impedance matched, which is required to reduce unwanted losses or back reflections.

5.3 Experimental system and methods

The silica microtoroid (diameter 41 µm) used in our experiments is fabricated using techniques as previously reported (see for example [22, 23]). The complete optical system is shown in fig. 5.3, and revolves around a tuneable fibre-coupled external cavity diode laser (New Focus, TLB-6728) that is locked to a mechanical sideband of a whispering gallery mode at 1542 nm using a (far-detuned) modified Pound-Drever-Hall (PDH) scheme [32], which can be used independent of the probe beam direction. The locking signal is generated by modulating the control arm using an Electro-Optic Modulator (Covega Mach-10 053) that is weakly driven by a tunable radio-frequency source (Rigol, DSG815) at a frequency of $\Omega_{\mathrm{m}}+\kappa/2$. It is essential to choose a driving frequency different from Ω_{m}, as the beat of the control frequency and modulated sideband would otherwise drive the mechanical mode. The residual transmission of the modulated control beam is incident on detector D2 (New Focus 1811-FC), of

which the output is demodulated (Mini-Circuits ZRPD-1) at the modulation frequency to yield the locking signal, which is subsequently sent to a servo controller (New Focus LB-1005) used to provide feedback to stabilize the laser frequency. To be able to lock at precisely the mechanical sideband, the phase of the demodulation reference is adjusted to yield an absorptive instead of the dispersive lineshape as obtained in standard PDH locking. Adjusting the offset voltage of the servo controller allows fine control over the resulting zero-crossing (*i.e.* locking point) and thus the detuning with respect to the cavity mode.

5.3.1 Optical setup

The probe light is generated using a commercial Double-Parallel Mach-Zehnder Interferometer (DPMZI, Thorlabs LN86S-FC) operated in single-side-band carrier-suppressed mode, driven by the output of a Vector Network Analyzer (VNA, Rohde & Schwarz ZNB-8) at frequency Ω, such that the resulting probe light has frequency $\omega_{\text{probe}} = \omega_{\text{control}} \pm \Omega$. The sign of the frequency shift, as well as the suppression of the carrier (by 50 dB with respect to the generated probe) is controlled by bias voltages applied to the DPMZI (appendix A). Pump and probe amplitude and polarization are controlled with Variable Optical Attenuators (VOA) and Fibre Polarization Controllers (FPC). The probe beam propagating in forward or backward direction is recombined with the control beam and their beat on fast (125 MHz) low-noise photo receivers (D1/D2) is analyzed with the VNA. It should be noted that fluctuations of the optical length difference of probe and control paths generate phase fluctuations of the beat analyzed by the VNA. To minimize these phase fluctuations on

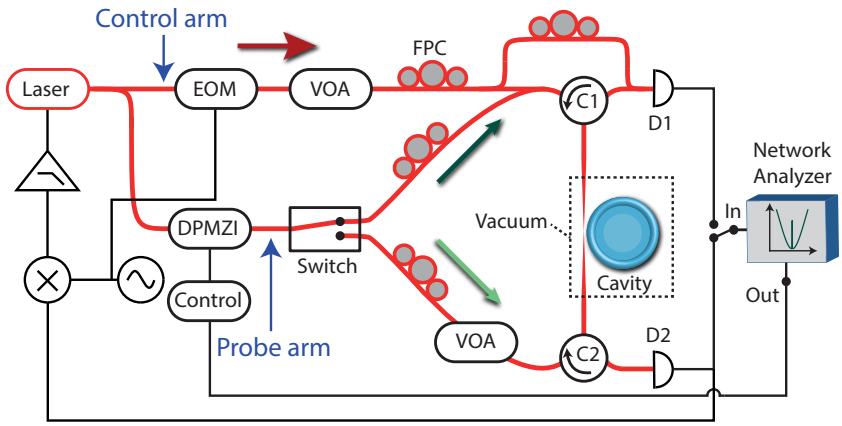

Figure 5.3: Experimental setup. Red lines indicate fibre optics, black lines coaxial cables. Full details are provided in the text. EOM: Electro-Optic Modulator, VOA: Variable Optical Attenuator, FPC: Fibre Polarization Controller, DPMZI: Double-Parallel Mach-Zehnder Interferometer, C_i: Circulator, D_i: Detector.

the time scale of the inverse bandwidth $(5\ \mathrm{kHz})^{-1}$ of the VNA, the lengths of the paths Laser/C1/D2 and Laser/Switch/C1/D2, as well as those of the paths Laser/D1 and Laser/Switch/C2/D1, are approximately (on the order of centimetres) matched using a fibre optic splicer. Finally, we note that the microtoroid is held in a home-built vacuum chamber that is kept at a reduced pressure of (typically) 2×10^{-6} mbar during experiments.

5.3.2 Calibration and fitting

Before each measurement the probe power in both propagation directions is balanced using a VOA in one of the probe arms. The polarization of both probe directions is controlled via FPCs, which are tuned separately to optimize the fibre-to-cavity-mode coupling. To calibrate the transmittance at the probe frequency, a reference measurement is performed with control and probe tuned away from the cavity resonance. Both the reference and measurement are averages of 75 traces of a frequency-swept probe. For each measurement eqs. (4.27) and (4.28) are fitted over a wide ω range used to determine $\bar{\Delta}_j$ and κ_j. Fixing these values, the same equation is fitted to a smaller frequency range surrounding the OMIT peak to yield values for η_j and $|g_j|$. In all fits, the mechanical resonance frequency $\Omega_\mathrm{m}/2\pi$ and linewidth $\Gamma_\mathrm{m}/2\pi$ are kept fixed at the independently determined values from thermal noise spectra obtained with a spectrum analyzer. For the microtoroid carrying two degenerate optical modes the mechanical parameters reads $(\Omega_\mathrm{m}, \Gamma_\mathrm{m})/2\pi \approx (47.04\,\mathrm{MHz},\ 87.7\,\mathrm{kHz})$. For the split-mode experiment (fig. 5.6) we obtain $\Omega_\mathrm{m}/2\pi \approx 35.4\,\mathrm{MHz}$, $|\omega + \bar{\Delta}_{1,2}|/2\pi \approx 4\,\mathrm{MHz}$ and $\kappa_{1,2}/2\pi \approx 12\,\mathrm{MHz}$. Using these values in eq. (5.1) directly gives a deviation from the optimal drive phase $\Delta\phi$ of only $\sim 0.2\%$ in the split mode experiment.

5.4 Experimental results

5.4.1 Isolation

In our experiment, we demonstrate optical isolation by studying the two-way transmittance of a probe signal at frequency ω_probe through a tapered fibre that is coupled to a microcavity ($\omega_{1,2}/2\pi = 194.5$ THz) with linewidth $\kappa_i/2\pi = 28$ MHz. With the control laser incident from one direction, the transmittance is quantified using the heterodyne spectroscopic technique outlined in section 5.3.1. The fact that the measurement technique used here allows to quantify the resulting transmittance provides a means to extract the obtained optical isolation, in contrast to the qualitative measurements reported in [15, 17]. The resulting probe transmittance (fig. 5.4a) for a red-detuned control beam ($\bar{\Delta}_{1,2} = -\Omega_\mathrm{m}$) and near-critical coupling conditions shows a bidirectional transmission dip as the probe frequency is scanned across the cavity resonance. Importantly, the optomechanically induced transparency window [13], which

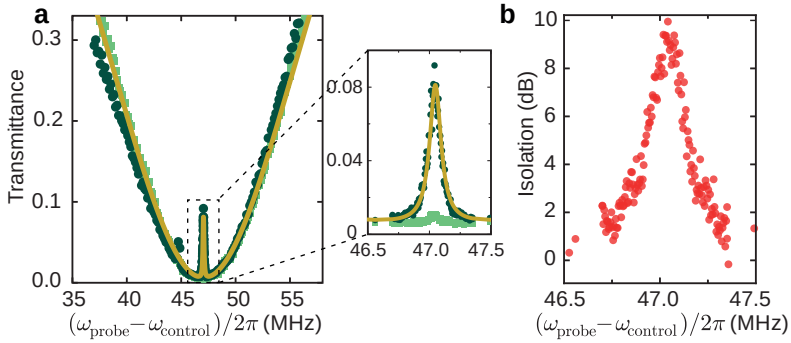

Figure 5.4: Mechanically-induced optical isolation. **a**, Transmittance of the optical probe beam as a function of probe-control detuning with the control frequency (power ∼17 µW) tuned to the red mechanical sideband. When the probe beam co-propagates (dark green circles) with the control beam, an OMIT transmission window is observed, which is absent when the control and probe counter-propagate (light green squares), resulting in nonreciprocal optical transmission. The solid yellow line is a fit of $|s_{21}|^2$ (eq. (4.28)) using independently determined values $(\Omega_{\rm m}, \Gamma_{\rm m})/2\pi \approx (47.04\,{\rm MHz}, 87.7\,{\rm kHz})$, yielding $(\kappa_{1,2}, |g_1|)/2\pi = (28\,{\rm MHz}, 292\,{\rm kHz})$ and $\eta_{1,2} \approx 0.45$. **b**, Resulting isolation, quantified as the ratio of measured probe transmittance in both directions.

results from destructive intracavity interference of anti-Stokes scattering of the control beam from the probe-induced mechanical vibrations with the probe beam itself (see section section 1.5.3), is solely present for co-propagating control and probe (dark green circles). For reversed probe direction the narrow OMIT peak is absent (light green squares). The device thus breaks Lorentz reciprocity and acts as an optical isolator, reaching up to 10 dB of isolation (fig. 5.4b).

To parametrize the strength of the induced transparency peak, it is convenient to introduce the total cooperativity $\mathcal{C}$, which is defined as $\mathcal{C} \equiv \mathcal{C}_1 + \mathcal{C}_2$. Here, $\mathcal{C}_i$ is given by $\mathcal{C}_i = 4|g_i|^2/(\kappa_i \Gamma_{\rm m})$. The cooperativity thus gives information about the strength of the optomechanical coupling with respect to the loss rates of the optical and mechanical resonators. In our isolator experiment the fit in fig. 5.4a gives cooperativity values of $\mathcal{C}_1 = \mathcal{C}_2 \approx 0.14$, such that the total cooperativity $\mathcal{C} = 0.28$. Using this value, we can directly calculate a nonreciprocal transmission bandwidth $\Gamma_{\rm eff}$ that is equal to $\Gamma_{\rm eff} = \Gamma_{\rm m}(1 + \mathcal{C}) = 1.28\Gamma_{\rm m}$ (section 4.6.2), which in this experiment is limited by the cooperativity that we can obtain. For degenerate, critically coupled optical modes with the control field tuned to either mechanical sideband, the maximum contrast ΔT between forward and backward transmittance is

$$\Delta T = |s_{21}|^2 - |s_{12}|^2 = \left(\frac{\mathcal{C}}{\mathcal{C} \pm 1}\right)^2 \tag{5.2}$$

at $(\omega = \pm\Omega_{\rm m}, \bar{\Delta}_{1,2} = \mp\Omega_{\rm m})$, where $\mathcal{C} = 2\mathcal{C}_1 = 2\mathcal{C}_2$. The pronounced increase of

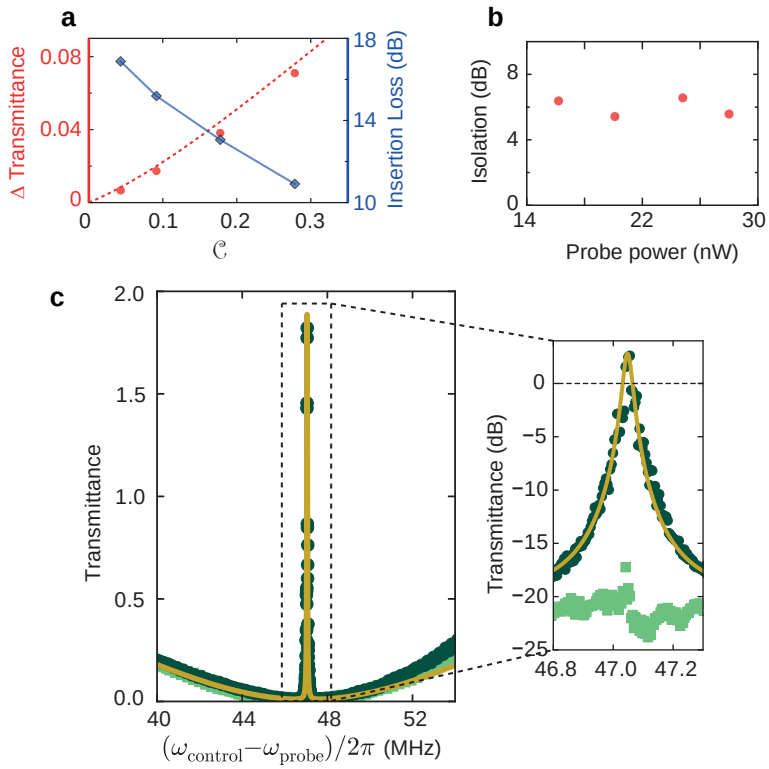

Figure 5.5: Power dependence and nonreciprocal amplification. **a**, Difference between forward/backward transmittance (measured, red circles, and theory ($|s_{21}|^2$-$|s_{12}|^2$, dashed red line) with respect to cooperativity, directly proportional to the control laser power. Together with an increase in contrast, the insertion losses (blue diamonds) decrease with increasing cooperativity. The theory curve is obtained using the average value $\eta_j = 0.453$ as determined from the four measurements at different control powers. **b**, The isolation as a function of probe power sent through the fibre. The physical mechanism behind optical isolation is linear, and thus does not depend on probe power. **c**, When the control beam is tuned to the blue side band of the cavity, it can parametrically amplify the probe beam that co-propagates with it through the fibre (dark green circles). In contrast, the counter-propagating probe beam (light green squares) experiences normal cavity extinction, thus yielding a nonreciprocal amplifier. With amplification of $\sim$ 3dB, the nonreciprocal difference in transmission is approximately 23 dB. The solid yellow line is a fit of $|s_{21}|^2$ (eq. (4.28)) yielding $(\kappa_{1,2}, |g_1|)/2\pi \approx (28\,\mathrm{MHz}, 454\,\mathrm{kHz})$ and $\eta_{1,2} \approx 0.46$.

ΔT with increasing $\mathcal{C}$, and concomitant decrease of insertion loss, are confirmed by varying the optical drive power (fig. 5.5a). The mechanism has strong potential for near-ideal isolation at negligible insertion losses, for example in optimized silica microtoroids, where $\mathcal{C} \approx 500$ was demonstrated [8]. Moreover, as discussed in chapter 4, a higher cooperativity in this side-coupled case strongly enhances the bandwidth, which is ultimately limited by the optical linewidth [14]. Lastly, we note that an important aspect of this mechanism is that the isolation is independent of probe power as demonstrated in fig. 5.5b, differing fundamentally from mechanisms exploiting Kerr or Kerr-like nonlinearities [33, 34] to create asymmetric transmission. In fact, it has recently been proven that such nonlinear systems cannot provide isolation for arbitrary backwards traveling waves [35], severely limiting their possible use.

5.4.2 Noise due to the thermal bath

To validate the omission of thermal fluctuations in the equations of motion describing our experiment (chapter 4), we calculate the number of thermal noise photons exiting our system. In the resolved-sideband regime, for degenerate modes with equal driving and linewidth, the amount of detected photons per second (N_{noise}) that is generated through a coupling between the mechanical resonator and the heat bath reads

$$N_{\mathrm{noise}} \approx \Gamma_{\mathrm{m}} N_{\mathrm{th}} \times \frac{\Gamma_{\mathrm{cool}}}{\Gamma_{\mathrm{cool}} + \Gamma_{\mathrm{m}}} \eta \times \frac{\Delta B}{\Gamma_{\mathrm{cool}} + \Gamma_{\mathrm{m}}}, \tag{5.3}$$

where the thermal population at the mechanical frequency is given by $N_{\mathrm{th}} \approx k_{\mathrm{B}} T / \hbar \Omega_{\mathrm{m}}$, the optomechanical cooling rate is $\Gamma_{\mathrm{cool}} = 4g^2/\kappa$ and the measurement bandwidth (in our experiment the VNA bandwidth) is given by ΔB. From left to right, the terms in this equation can be associated with the number of noise phonons generated in the resonator, the fraction of noise photons leaving through the optical channel, and the fraction of noise photons in the signal bandwidth, respectively. Note that the expression can be rewritten to yield $N_{\mathrm{noise}} = (\mathcal{C} N_{\mathrm{th}} \eta \Delta B)/(\mathcal{C}+1)^2$, from which $N_{\mathrm{noise}} \approx 4 \times 10^8$ is obtained for our system. As a probe power of 15 nW at 1542 nm corresponds to $\approx 1 \times 10^{11}$ photons/s, the thermal noise in our system contributes only marginally (0.4%) to the measured probe signal.

5.4.3 Amplification and non-degeneracy

For blue-detuned control ($\bar{\Delta}_{1,2} = +\Omega_{\mathrm{m}}$), the probe beam experiences parametric amplification if control and probe are co-propagating, while it is fully dissipated when counter-propagating with the pump, thus yielding a nonreciprocal optical amplifier (fig. 5.5c). For this particular microtoroid we obtain approximately 3 dB amplification (for a total cooperativity $\mathcal{C} \approx 0.67$), such that the total contrast in transmittance reaches up to 23 dB. This feature could pose

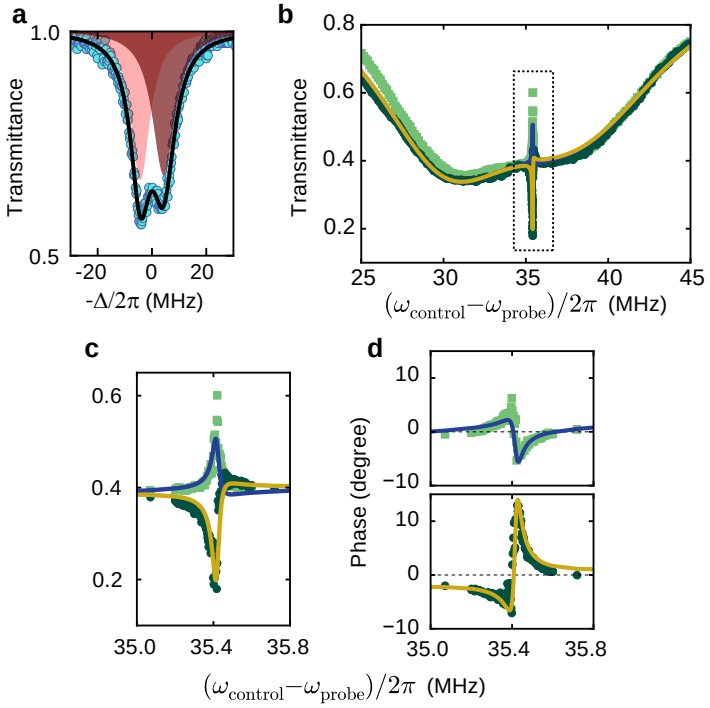

Figure 5.6: Non-degenerate optical modes. **a**, Transmittance of an optical split-mode (splitting ∼8.6 MHz) as a function of laser-cavity detuning, obtained by sweeping the laser frequency and measuring the resulting transmittance using an oscilloscope. The horizontal axis is calibrated using the EOM placed in the control arm (see fig. 5.4a). The black solid line represents a fit of a double Lorentzian lineshape to the blue data points. The red shading is the area under the two fitted Lorentzian lineshapes. **b**, Transmittance of the optical probe beam as a function of control-probe detuning with the control frequency fixed at the blue mechanical side band. When the probe beam co-propagates ($|s_{21}|^2$, dark green circles) with the control beam an optomechanically induced absorption window appears, while the oppositely propagating probe ($|s_{12}|^2$, light green squares) experiences increased transmission. **c**, Zoom of the area depicted by the dotted box in **b**. **d**, Asymmetric phase transmission for the same measurement as **b**. Light green squares correspond to $\arg(s_{12})$, the dark green circles to $\arg(s_{21})$. The solid lines in **b** are fitted simultaneously to $|s_{12}|^2$ (blue line) and $|s_{21}|^2$ (yellow line). The resulting parameters are inserted in s_{12} (blue line) and s_{21} (yellow line) with no other fit parameters than a vertical offset.

interesting signal processing functionality, including nonreciprocal narrowband RF filtering and insertion loss compensation.

Next, we study nonreciprocal transmission for a microtoroid that has two non-degenerate optical modes. As predicted in section 5.2, our experimental results show that strong nonreciprocity can also be obtained without optical degeneracy. Figure 5.6 shows nonreciprocal amplitude and phase transmission with a split optical mode. A probe beam tuned between the even and odd mode frequencies excites both modes with unequal phases. These opposing phases are added to the $a_1 \rightarrow a_2$ and $a_2 \rightarrow a_1$ optomechanical mode conversion processes, respectively, changing the interference condition with the nonresonant (direct) transmission path. As a result, both co- and counter-propagating probe fields now display narrowband features that result from the interaction with the mechanical mode. For a blue-detuned control beam, this yields induced absorption for the co-propagating probe (dark-green circles) and induced transparency for the counter-propagating probe (light green circles) as shown in fig. 5.6b. Note that the induced absorption for the co-propagating beam is related to the relatively low fibre-to-cavity coupling rate ($\eta_{1,2} < 1/2$). It can be turned into gain, as presented in fig. 5.5c, for $\eta_{1,2} > 0.5$ and/or for increased optical control power. Crucially, since for our system the frequency splitting between both modes is small with respect to the optical linewidth, the deviation of the imprinted phase $\Delta\phi$ from optimal is only 0.2% (section 5.2). As such, a control beam incident from one side still ensures $\Delta\phi \approx \pi/2$ and $\mathcal{C}_1 \approx \mathcal{C}_2$, thus fulfilling the requirements for optimal nonreciprocity and maximizing the contrast between forward and backward transmission. In a more general case, optimal conditions may be implemented, for example by supplying control fields with suitable phase and amplitude through both input waveguides. Importantly, the fact that nonreciprocity can be obtained without strict optical degeneracy increases the range of systems that may be employed.

5.5 Conclusion and Outlook

We stress that the demonstrated principles are not limited to the experimental implementation using ring resonators shown here, but can be realized in a wide range of optomechanical platforms [5], such as LC circuits [26–28] and photonic crystal resonators [25] (fig. 5.7a-b). In fact, the high (GHz) frequency of the latter devices has the prospect of enhancing the bandwidth with respect to the relatively narrow range demonstrated here, towards a range commensurate with typical signal modulation rates. While the resonant nature of the demonstrated mechanism is of course a limit to the general application capability, we foresee several applications that could benefit from magnetic-free isolation over a finite bandwidth. These include in particular the protection of on-chip monochromatic laser sources and, with ground-state cooling [6, 7] or in the strong coupling regime [8], low-loss routing of signals carrying quantum information

at negligible added noise, either at optical or microwave frequencies [14, 36].

The specific nonreciprocal functionality is governed by the way these systems are coupled to input/output channels. This, in turn, is directly related to the nonresonant scattering matrix C, as reciprocity of optical modes dictates $CD^* = -D$ [37]. For the scenarios in figure 5.7a, described by a diagonal C matrix, each waveguide couples to a single optical mode, and the system operates as a nonreciprocal phase shifter (gyrator) in absence of other optical loss. Importantly, an on-chip gyrator that is placed in one arm of an integrated Mach-Zehnder interferometer could be used to build an on-chip circulator [38]. In contrast, isolation is most naturally achieved if C is the exchange matrix, meaning a direct path between the two ports is present (fig. 5.7b). We note that nonreciprocal light transmission also occurs outside the resolved sideband regime, although the behaviour there is more complex due to mixing of sidebands at $\pm\omega$ [39].

In conclusion, we demonstrated and quantified nonreciprocal transmission through a compact optomechanical isolator and one-way parametric amplifier, and developed a general theory explaining the mechanism and unifying the description of various implementations of optomechanical nonreciprocity in multimode systems. Our findings identify two general requirements for any optomechanical system to optimally break reciprocity: asymmetric coupling of the optical modes to input/output channels, and a drive phase-difference of $\pi/2$.

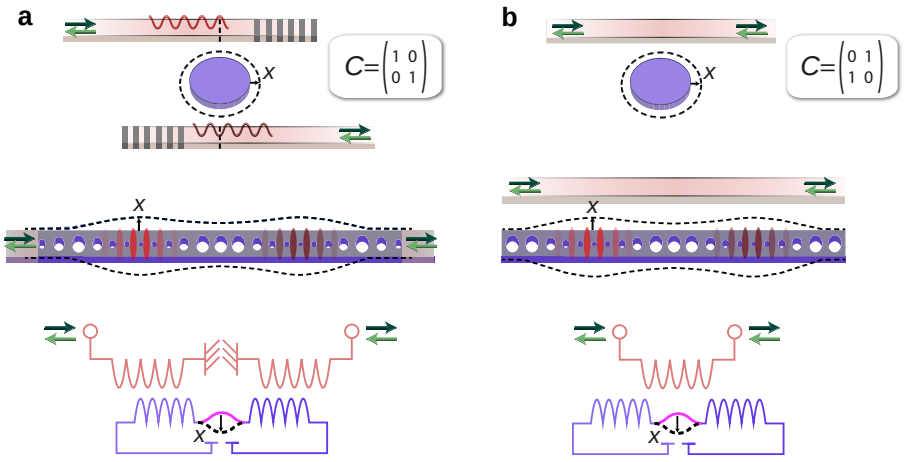

Figure 5.7: General optomechanical nonreciprocity in different systems. **a**, If the optical and mechanical resonators are placed in the direct propagation path, the displayed systems have a diagonal direct scattering matrix C, which builds a non-reciprocal phase shifter. **b**, However, if the optomechanical system provides an extra (nonreciprocal) propagation path in addition to the direct scattering path, the C matrix has off-diagonal elements which can interfere with the nonreciprocal path to yield isolation or amplification. Dark and light green arrows represent wave transmission from opposite system ports.

Since the requirements for optimal nonreciprocity derived here do not rely on the handedness of optical [14, 17] or mechanical [15, 16] modes, our theoretical formalism can be used to realize optomechanical nonreciprocity in systems that do not exhibit circular symmetry (fig. 5.7). Extending the demonstrated principles to more modes or channels would enable a variety of nonreciprocal functionality for both light and sound, including on-chip circulation, gyration [18] and enhanced isolation bandwidth. Finally, these nonreciprocal systems can form the unit cell of optomechanical metamaterials with topologically nontrivial properties, where the nonreciprocal phase takes the role of an effective gauge field to establish new phases for sound and light [20, 21].

References

[1] L. Deák, and T. Fülöp, *Reciprocity in quantum, electromagnetic and other wave scattering*, Ann. Phys. (N. Y). **327**, 1050 (2012).

[2] F. D. M. Haldane, and S. Raghu, *Possible realization of directional optical waveguides in photonic crystals with broken time-reversal symmetry*, Phys. Rev. Lett. **100**, 013904 (2008).

[3] T. Carmon, H. Rokhsari, L. Yang, T. J. Kippenberg, and K. J. Vahala, *Temporal behavior of radiation-pressure-induced vibrations of an optical microcavity phonon mode*, Phys. Rev. Lett. **94**, 223902 (2005).

[4] T. J. Kippenberg, H. Rokhsari, T. Carmon, A. Scherer, and K. J. Vahala, *Analysis of radiation-pressure induced mechanical oscillation of an optical microcavity*, Phys. Rev. Lett. **95**, 033901 (2005).

[5] M. Aspelmeyer, T. J. Kippenberg, and F. Marquardt, *Cavity optomechanics*, Rev. Mod. Phys. **86**, 1391 (2014).

[6] J. D. Teufel, et al., *Sideband cooling of micromechanical motion to the quantum ground state.*, Nature **475**, 359 (2011).

[7] J. Chan, et al., *Laser cooling of a nanomechanical oscillator into its quantum ground state*, Nature **478**, 89 (2011).

[8] E. Verhagen, S. Deléglise, S. Weis, A. Schliesser, and T. J. Kippenberg, *Quantum-coherent coupling of a mechanical oscillator to an optical cavity mode*, Nature **482**, 63 (2012).

[9] F. Massel, et al., *Microwave amplification with nanomechanical resonators*, Nature **480**, 351 (2011).

[10] C. Dong, V. Fiore, M. C. Kuzyk, and H. Wang, *Optomechanical dark mode*, Science **338**, 1609 (2012).

[11] J. T. Hill, A. H. Safavi-Naeini, J. Chan, and O. Painter, *Coherent optical wavelength conversion via cavity optomechanics*, Nat. Commun. **3**, 1196 (2012).

[12] F. Lecocq, J. B. Clark, R. W. Simmonds, J. Aumentado, and J. D. Teufel, *Mechanically mediated microwave frequency conversion in the quantum regime*, Phys. Rev. Lett. **116**, 043601 (2016).

[13] S. Weis, et al., *Optomechanically induced transparency*, Science **330**, 1520 (2010).

[14] M. Hafezi, and P. Rabl, *Optomechanically induced non-reciprocity in microring resonators*, Opt. Express **20**, 7672 (2012).

[15] J. Kim, M. C. Kuzyk, K. Han, H. Wang, and G. Bahl, *Non-reciprocal Brillouin scattering induced transparency*, Nat. Phys. **11**, 275 (2015).

[16] C.-H. Dong, et al., *Brillouin-scattering-induced transparency and non-reciprocal light storage*, Nat. Commun. **6**, 6193 (2015).

[17] Z. Shen, et al., *Experimental realization of optomechanically induced non-reciprocity*, Nat. Photonics **10**, 657 (2016).

[18] S. J. M. Habraken, K. Stannigel, M. D. Lukin, P. Zoller, and P. Rabl, *Continuous mode cooling and phonon routers for phononic quantum networks*, New J. Phys. **14**, 115004 (2012).

[19] X.-W. Xu, and Y. Li, *Optical nonreciprocity and optomechanical circulator in three-mode optomechanical systems*, Phys. Rev. A **91**, 053854 (2015).

[20] V. Peano, C. Brendel, M. Schmidt, and F. Marquardt, *Topological phases of sound and light*, Phys. Rev. X **5**, 031011 (2015).

[21] M. Schmidt, S. Kessler, V. Peano, O. Painter, and F. Marquardt, *Optomechanical creation of magnetic fields for photons on a lattice*, Optica **2**, 635 (2015).

[22] D. K. Armani, T. J. Kippenberg, S. M. Spillane, and K. J. Vahala, *Ultra-high-Q toroid microcavity on a chip*, Nature **421**, 925 (2003).

[23] A. Schliesser, R. Rivière, G. Anetsberger, O. Arcizet, and T. J. Kippenberg, *Resolved-sideband cooling of a micromechanical oscillator*, Nat. Phys. **4**, 415 (2008).

[24] Z. Yu, and S. Fan, *Complete optical isolation created by indirect interband photonic transitions*, Nat. Photonics **3**, 91 (2009).

[25] K. Fang, et al., *Generalized non-reciprocity in an optomechanical circuit via synthetic magnetism and reservoir engineering*, Nat. Phys. **13**, 465 (2017).

[26] G. A. Peterson, et al., *Demonstration of efficient nonreciprocity in a microwave optomechanical circuit*, Phys. Rev. X **7**, 031001 (2017).

[27] N. R. Bernier, et al., *Nonreciprocal reconfigurable microwave optomechanical circuit*, Nat. Commun. **8**, 604 (2017).

[28] S. Barzanjeh, et al., *Mechanical on-chip microwave circulator*, arXiv 1706.00376 (2017).

[29] D. L. Sounas, C. Caloz, and A. Alù, *Giant non-reciprocity at the subwavelength scale using angular momentum-biased metamaterials*, Nat. Commun. **4**, 2407 (2013).

[30] N. A. Estep, D. L. Sounas, J. Soric, and A. Alù, *Magnetic-free non-reciprocity and isolation based on parametrically modulated coupled-resonator loops*, Nat. Phys. **10**, 923 (2014).

[31] D. L. Sounas, and A. Alù, *Angular-momentum-biased nanorings to realize magnetic-free integrated optical isolation*, ACS Photonics **1**, 198 (2014).

[32] E. D. Black, *An introduction to Pound–Drever–Hall laser frequency stabilization*, Am. J. Phys. **69**, 79 (2001).

[33] S. Manipatruni, J. T. Robinson, and M. Lipson, *Optical nonreciprocity in optomechanical structures*, Phys. Rev. Lett. **102**, 213903 (2009).

[34] L. Fan, et al., *An all-silicon passive optical diode*, Science **335**, 447 (2012).

[35] Y. Shi, Z. Yu, and S. Fan, *Limitations of nonlinear optical isolators due to dynamic reciprocity*, Nat. Photonics **9**, 388 (2015).

[36] A. Metelmann, and A. A. Clerk, *Nonreciprocal photon transmission and amplification via reservoir engineering*, Phys. Rev. X **5**, 021025 (2015).

[37] W. Suh, Z. Wang, and S. Fan, *Temporal coupled-mode theory and the presence of non-orthogonal modes in lossless multimode cavities*, IEEE J. Quantum Electron. **40**, 1511 (2004).

[38] C. L. Hogan, *The ferromagnetic Faraday effect at microwave frequencies and its applications: The microwave gyrator*, Bell Syst. Tech. J. **31**, 1 (1952).

[39] M.-A. Miri, F. Ruesink, E. Verhagen, and A. Alù, *Optical nonreciprocity based on optomechanical coupling*, Phys. Rev. Appl. **7**, 064014 (2017).

Chapter 6

Demonstrating Mechanically-Induced Optical Circulation

In this chapter, we demonstrate mechanically-induced optical circulation in a 4-port device. The experimental system utilizes two tapered fibres that are simultaneously coupled to a high-Q microtoroid ring resonator to build a 4-port optical system. Employing the interaction with the mechanical radial breathing mode, we show that this system breaks Lorentz reciprocity in all four ports to yield a compact optical circulator. Besides providing the required symmetry breaking, the optomechanical interaction also suppresses back-reflections and unwanted cross-coupling. Moreover, using a blue-detuned control field and the resulting optical gain we obtain per-channel isolation ratios of $\sim$10 dB at a few dB insertion loss. We present a theory that describes the demonstrated results and provides handles for improving the device characteristics.

6.1 Introduction

In the previous two chapters we discussed how an optomechanical resonator can break Lorentz reciprocity without the use of external magnetic fields. To utilize this and build a working isolator, the system was interrogated via *two* input and output ports only. In order to obtain the required isolation properties – and not violate energy conservation and the second law of thermodynamics – this requires excess energy to be dissipated [1, 2]. In other words, it means that photons originally present in the system leave the closed environment and are left undetected.

In many ways, this description of an optical isolator is analogous to a simple 3-port microwave *circulator* with a matched load placed in one of its ports; the addition of (perfect) loss provides the required dissipation, resulting in a microwave *isolator*. The original circulator is simply obtained back by removal of the load. Consequently, this sparks the question if a similar approach is viable for an optical system, *i.e.,* to remove the dissipative reservoir from the isolator and replace it with an optical waveguide (transmission line). If it is possible to detect and supply a field from this transformed 'dissipation' channel, while simultaneously interfacing it with a nonreciprocal optomechanical system, this could supply a suitable base for the creation of a compact optical circulator. Such a photon router, which would operate in absence of external magnetic fields, could provide useful functionality for light-based information systems. Very recently, optical circulation based on cold atoms using magneto-optic induced Zeeman splitting was demonstrated [3]. Another experimental route is provided by the versatile platform of optomechanics [4], and initial results on mechanically-induced microwave circulation utilizing a frequency-conversion method have been reported recently [5].

In this chapter, we show a fibre-integrated prototype of a 4-port *optical* circulator that is based on optomechanical interactions. The experimental system revolves around a high-Q toroidal ring resonator that is simultaneously coupled to two tapered fibres, where the coupling to either fibre (ideally) overwhelms the intrinsic optical losses in the system. In other words, the additional fibre replaces the dissipative bath with two fibre-mediated loss channels that allow detection of escaping photons. Moreover, it permits access to the resonator yielding a complete 4-port device. In the absence of a coherent optomechanical interaction between the optical modes and mechanical radial breathing mode of the ring resonator, such a system is analogous to a reciprocal add-drop filter. However, as we derive and demonstrate, it is the presence of a strong control beam placed on the red or blue motional sideband of the cavity that breaks Lorentz reciprocity in the system, allowing its operation as a circulator.

Before discussing experimental details and results, the theory that describes the optomechanical circulator is presented. This theory builds upon the previous two chapters, and interfaces coupled-mode theory [6, 7] with the optomechanical equations of motion [4]. We then demonstrate how this

theory accurately predicts a reciprocal add-drop filter (in the absence of optomechanical interactions) and that the optomechanical interaction results in an asymmetric scattering matrix. Finally we present experimental results for all 16 (4×4) scattering parameters, which are well described by our theoretical model. We achieve a maximum isolation ratio of approximately 2 dB in all channels when our control beam is tuned to the red motional sideband. Moreover, we emphasize the suppression of unwanted reflections and cross-coupling in this scenario, which largely results from the nonreciprocal optomechanical interaction. In addition, we present results with the control beam tuned to the blue sideband, where we obtain higher isolation ratios ($> 10\,\mathrm{dB}$) at relatively small insertion losses.

6.2 Theory of optomechanical circulation

The scattering matrix of an ideal 4-port circulator is given by

$$S = \begin{pmatrix} 0 & 0 & 0 & 1 \\ 1 & 0 & 0 & 0 \\ 0 & 1 & 0 & 0 \\ 0 & 0 & 1 & 0 \end{pmatrix}, \tag{6.1}$$

where S connects the outgoing fields $\mathbf{s}^-$ to incoming fields $\mathbf{s}^+$ via $\mathbf{s}^- = S\mathbf{s}^+$. For a 4-port circulator, these vectors are explicitly written as $\mathbf{s}^{-(+)} = (s_1^{-(+)}, s_2^{-(+)}, s_3^{-(+)}, s_4^{-(+)})^{\mathrm{T}}$, where the subscripts signal the port number j through which the fields exit or enter the system (fig. 6.1). Note that in the

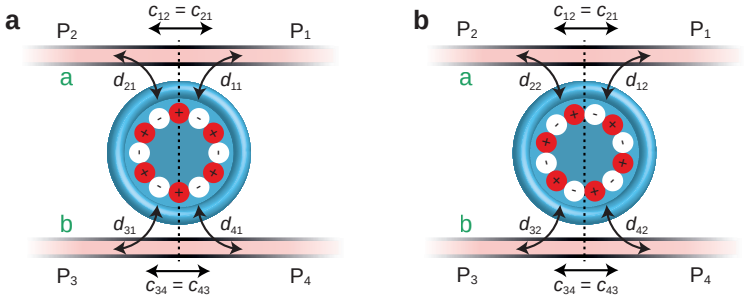

Figure 6.1: Ring resonator modes. a/b, Definition of the mode-to-port coupling elements d_{ji} for the even (**a**) and odd (**b**) superposition of clockwise and counterclockwise propagating modes inside the ring resonator. At the symmetry point indicated by the dashed line, the even and odd mode are $\pi/2$ out of phase, *i.e.,* the phase difference between the (+) and (−) signs is π. As a result, the D matrix elements d_{22} and d_{12} for the odd mode (**b**) are π out of phase: $d_{22} = -d_{12}$, while for the even mode (**a**) these are equivalent. In addition, the non-zero elements of the direct scattering matrix C are given. The green letters 'a' and 'b' indicate the relevant waveguides. P_j indicate the entrance and exit ports.

ideal S-matrix given in eq. (6.1), all light entering port 1 is routed to port 2, and likewise from 2→3, 3→4 and 4→1. In stark contrast, the reverse pathways are completely blocked, as signalled by the zeros on positions s_{12}, s_{23}, s_{34} and s_{41}, respectively. In addition, reflections (*e.g.,* s_{11}) and cross-couplings (*e.g.,* s_{13}) in this ideal scenario are all zero.

A theoretical model of our geometry should yield expressions that describe the complete S-matrix. To achieve this, a similar formalism to that discussed in chapter 4 is used. For convenience, the most import results are briefly reiterated. Considering an optomechanical system that consists of two optical modes coupled to one mechanical mode, the 4×4 S matrix reads

$$S = C + \mathrm{i}D(M + \omega I)^{-1}D^{\mathrm{T}} \tag{6.2}$$

$$= C + \mathrm{i}D \begin{pmatrix} \Sigma_{\mathrm{o}_1} \mp |g_1|^2/\Sigma_{\mathrm{m}}^{\pm} & \mp(g_1 g_2^*)/\Sigma_{\mathrm{m}}^{\pm} \\ \mp(g_1^* g_2)/\Sigma_{\mathrm{m}}^{\pm} & \Sigma_{\mathrm{o}_2} \mp |g_2|^2/\Sigma_{\mathrm{m}}^{\pm} \end{pmatrix}^{-1} D^{\mathrm{T}}. \tag{6.3}$$

Here, the upper(lower) signs refer to a control beam red(blue) detuned with respect to the cavity mode, and the inverse susceptibilities are defined as

$$\Sigma_{\mathrm{m}}^{\pm} \equiv \omega \mp \Omega_{\mathrm{m}} + \mathrm{i}\frac{\Gamma_{\mathrm{m}}}{2}; \quad \Sigma_{\mathrm{o}_{1,2}} \equiv \omega + \bar{\Delta}_{1,2} + \mathrm{i}\frac{\kappa_{1,2}}{2}. \tag{6.4}$$

Again, the detunings $\bar{\Delta}_{1,2}$ are the detuning of the control beam with respect to the two optical cavity modes, and ω is the detuning of the probe with respect to the control frequency. Moreover, the enhanced optomechanical (complex) coupling rates are given by $g_{1,2}$. In contrast to the previous chapters, the loss rate κ_i of each optical mode i is now defined as $\kappa_i \equiv \kappa_{0,i} + \kappa_{\mathrm{a},i} + \kappa_{\mathrm{b},i}$, where $\kappa_{0,i}$ refers to the intrinsic optical loss rate of the mode. Similarly $\kappa_{\mathrm{a},i}$ and $\kappa_{\mathrm{b},i}$ are associated with exchange losses to waveguides a and b (fig. 6.1).

As a consequence of the system's geometry with four optical ports, the C and D matrices required to complete eq. (6.3) are adapted to the four-port configuration. The optomechanical resonator discussed here is side-coupled to both waveguides, such that the direct scattering matrix C reads

$$C = \begin{pmatrix} 0 & 1 & 0 & 0 \\ 1 & 0 & 0 & 0 \\ 0 & 0 & 0 & 1 \\ 0 & 0 & 1 & 0 \end{pmatrix}. \tag{6.5}$$

Using the even and odd mode terminology (superpositions of the clockwise and counter-clockwise propagating modes), the D matrix is obtained as

$$D = \begin{pmatrix} d_{11} & d_{12} \\ d_{11} & -d_{12} \\ d_{31} & d_{32} \\ d_{31} & -d_{32} \end{pmatrix}, \tag{6.6}$$

where the mode symmetry shown in fig. 6.1 is used. Together with the relation $D^\dagger D = K_\mathrm{e}$, where K_e reads

$$K_\mathrm{e} = \begin{pmatrix} \kappa_{\mathrm{a},1} + \kappa_{\mathrm{b},1} & 0 \\ 0 & \kappa_{\mathrm{a},2} + \kappa_{\mathrm{b},2} \end{pmatrix}, \tag{6.7}$$

and $CD^* = -D$ [7, 8], this yields the explicit D matrix

$$D = \frac{1}{\sqrt{2}} \begin{pmatrix} \mathrm{i}\sqrt{\kappa_{\mathrm{a},1}} & -\sqrt{\kappa_{\mathrm{a},2}} \\ \mathrm{i}\sqrt{\kappa_{\mathrm{a},1}} & \sqrt{\kappa_{\mathrm{a},2}} \\ \mathrm{i}\sqrt{\kappa_{\mathrm{b},1}} & -\sqrt{\kappa_{\mathrm{b},2}} \\ \mathrm{i}\sqrt{\kappa_{\mathrm{b},1}} & \sqrt{\kappa_{\mathrm{b},2}} \end{pmatrix} \tag{6.8}$$

expressed in terms of fibre-to-cavity exchange losses. Inserting eqs. (6.5) and (6.8) in eq. (6.3) and performing the required algebra results in complete expressions for all 16 s-parameters. To display readable results we introduce the exchange efficiencies η, for example $\eta_{\mathrm{a},1} = \kappa_{\mathrm{a},1}/\kappa_1$, and assume $\eta_{\mathrm{a},1} = \eta_{\mathrm{a},2} = \eta_\mathrm{a}$ and $\eta_{\mathrm{b},1} = \eta_{\mathrm{b},2} = \eta_\mathrm{b}$. After the required manipulations we subsequently obtain

$$s_{21} = 1 - \mathrm{i}\frac{\eta_\mathrm{a} A_1^\pm + \eta_\mathrm{a} A_2^\pm \pm 2\eta_\mathrm{a}\sqrt{\mathcal{C}_1\mathcal{C}_2}\sin(\Delta\phi)}{(\delta_1+\mathrm{i})(\delta_2+\mathrm{i})(\delta_\pm+\mathrm{i}) \mp [(\delta_2+\mathrm{i})\mathcal{C}_1 + (\delta_1+\mathrm{i})\mathcal{C}_2]}, \tag{6.9}$$

$$s_{41} = -\mathrm{i}\frac{\sqrt{\eta_\mathrm{a}\eta_\mathrm{b}} A_1^\pm + \sqrt{\eta_\mathrm{a}\eta_\mathrm{b}} A_2^\pm \pm 2\sqrt{\eta_\mathrm{a}\eta_\mathrm{b}}\sqrt{\mathcal{C}_1\mathcal{C}_2}\sin(\Delta\phi)}{(\delta_1+\mathrm{i})(\delta_2+\mathrm{i})(\delta_\pm+\mathrm{i}) \mp [(\delta_2+\mathrm{i})\mathcal{C}_1 + (\delta_1+\mathrm{i})\mathcal{C}_2]}, \tag{6.10}$$

which are the direct and "add-drop" scattering coefficients for probe excitation from port 1, respectively. Here, the following definitions for the cooperativities ($\mathcal{C}_i$), normalized detunings (δ) and drive phase difference ($\Delta\phi$) are used;

$$\mathcal{C}_i \equiv \frac{4|g_i|^2}{\kappa_i \Gamma_\mathrm{m}}, \quad \delta_\pm \equiv \frac{\omega \mp \Omega_\mathrm{m}}{\Gamma_\mathrm{m}/2}, \quad \delta_i \equiv \frac{\omega + \bar{\Delta}_i}{\kappa_i/2}, \quad \Delta\phi = \arg(g_2) - \arg(g_1) \tag{6.11}$$

and $A_i^\pm$ is given by

$$A_i^\pm = (\delta_i + \mathrm{i})(\delta_\pm + \mathrm{i}) \mp \mathcal{C}_i. \tag{6.12}$$

Note that coefficient s_{41} describes light entering from waveguide 'a' and exiting from 'b'. Equation (6.10) thus naturally includes the coupling efficiencies to both waveguides. This is in contrast to eq. (6.9), which only depends on η_a and is similar to eq. (4.28) derived in chapter 4. To conclude, we note that the 'opposite' scattering coefficients s_{12} and s_{14} are simply obtained by changing the $\pm$ sign placed in front of the last term of the numerator in eqs. (6.9) and (6.10) to $\mp$.

6.2.1 Circulator design considerations

To investigate the resulting scattering coefficients in more detail, fig. 6.2 shows plots of $|s_{21}|^2$, teal solid line ($|s_{12}|^2$, black dashed line) and $|s_{41}|^2$, brown

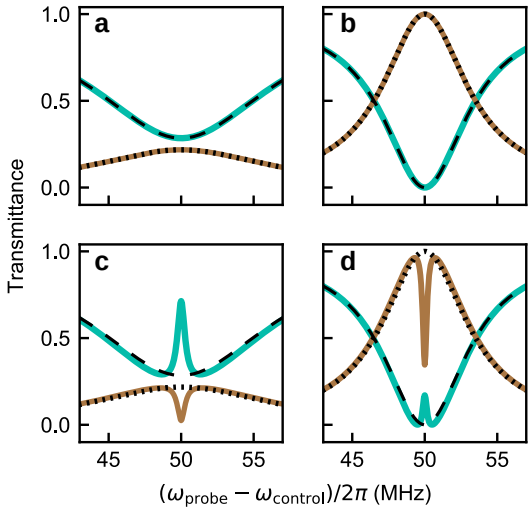

Figure 6.2: Add-Drop filter with and without optomechanical interaction. **a-d,** Plotted are $|s_{21}|^2(|s_{12}|^2)$, teal solid line(black dashed line), and $|s_{41}|^2(|s_{14}|)^2$, brown solid line(black dotted line) for two degenerate optical modes as a function of probe-control detuning. Here, $\omega_{control}$ is incident on P_1 (such that $\Delta\phi = \pi/2$) and detuned to the red motional sideband of the cavity mode. **a/b,** In the absence of optomechanical interaction ($\mathcal{C} = 0$), the system operates as a reciprocal add-drop filter. **a,** For $\kappa_a = \kappa_b = \kappa/4$, intrinsic cavity losses prohibit optimal transport of light from waveguide 'a' to 'b' (and vice-versa). **b,** Ideal add-drop behaviour is obtained when the intrinsic losses of both optical modes are negligible with respect to the exchange losses ($\kappa_a = \kappa_b = \kappa/2$). In this scenario, all light is exchanged between both waveguides, such that the device operates without insertion loss. **c/d,** Similar to **a/b**, respectively, with $\mathcal{C}_{1,2} = 1(\mathcal{C}_{1,2} = 0.35)$ for **c(d)**. The optomechanical interaction creates a nonreciprocal add-drop response when the probe-control detuning matches the chosen mechanical resonance frequency $\Omega_m = 50\,\mathrm{MHz}$. Importantly, the nonreciprocal OMIT window manifests itself in both the direct and add-drop pathways.

solid line ($|s_{14}|^2$, black dotted line) as a function of probe-control detuning ($\bar{\Delta}_{1,2} = -\Omega_m$) for two degenerate optical modes. As expected, the absence of optomechanical coupling (fig. 6.2a/b, $\mathcal{C}_i = 0$) yields line shapes that are equivalent to that of a reciprocal add-drop filter. Typical for such a filter is the complete conversion of light from one waveguide to another (fig. 6.2b), signalled by $|s_{41}|^2 = |s_{14}|^2 = 1$ and $|s_{21}|^2 = |s_{12}|^2 = 0$, when intrinsic losses are absent and $\eta_a = \eta_b$. In such a scenario both waveguides act as each other's (perfect) loss channel, inhibiting direct transmission while instead transferring all light to the 'other' waveguide.

In contrast, fig. 6.2c/d clearly indicate that the presence of optomechanical coupling breaks Lorentz reciprocity for all channels in the add-drop filter. Thus not only in the direct path ($|s_{21}|^2$ versus $|s_{12}|^2$), where a nonreciprocal

response is obtained over the optomechanically induced transparency window (OMIT), a direct result of destructive intracavity interference between anti-Stokes scattered control light with the probe beam itself. But also in the add-drop path ($|s_{14}|^2$ versus $|s_{41}|^2$), where it is the exact same OMIT window that enables unidirectional transmittance thus breaking reciprocity. Considering the attainable isolation, for port 1 and 2 defined as $|s_{12}|^2/|s_{21}|^2$, it is clear that a larger OMIT peak (obtained via a high cooperativity $\mathcal{C}$) maximizes the observed isolation in both the direct and add-drop circulator channels (fig. 6.3). Moreover, while an increased cooperativity also reduces insertion losses for the direct transmission channels, insertion losses for the add-drop channel are reduced by elimination of the intrinsic cavity losses. In an experiment, one typically aims to removes these intrinsic losses by strongly overcoupling the waveguides such that $\{\eta_\mathrm{a}, \eta_\mathrm{b}\} \to 1$.

We stress that the expressions for $s_{21}(s_{32})$ and $s_{43}(s_{14})$ in a four-port geometry are exactly equivalent*, and that the same is true for their reverse pathways. Intuitively this is easy to understand considering the symmetry in the system. Probe signals from for example port 1 and 3 interact in exactly the same way with the intracavity control field. Moreover, this means that for a red-detuned control beam incident on either port 1 or 3, an equally strong induced transparency window opens up for probe fields entering through both these ports. As such, an experiment that utilizes the side-coupled geometry requires only one control beam to achieve circulation. This provides a significant advantage over other optomechanical implementations that realize circulation using frequency-conversion [5], or where Lorentz reciprocity is broken using a so-called end-fire geometry [9–11]. These systems require a multitude of carefully (phase-)tuned control frequencies, increasing the overall experimental

*assuming $\eta_{\mathrm{a,i}} = \eta_{\mathrm{b,i}} = \eta_i$.

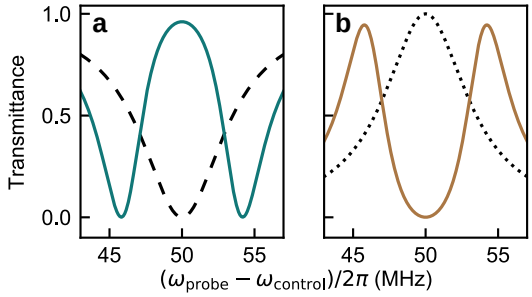

Figure 6.3: Isolation and bandwidth at high cooperativity. a/b, For $\mathcal{C}_{1,2} = 25$ and in absence of intrinsic optical losses, the device exhibits near perfect isolation at negligible insertion loss. In addition, the elevated cooperativity widens the OMIT peak and thus the resulting nonreciprocal bandwidth. **a,** $|s_{21}|^2$, teal solid line ($|s_{12}|^2$, black dashed line) and **b,** $|s_{41}|^2$, brown solid line ($|s_{14}|^2$, black dotted line).

complexity. Moreover, connecting back to the discussion in chapter 4, the nonreciprocal bandwidth in these systems is limited to twice the intrinsic mechanical linewidth.

Summarizing that an optomechanical 4-port circulator relies on 1) an induced transparency window and 2) ideal unidirectional add-drop functionality, we can stipulate design principles for an ideal optomechanical circulator: An experiment should ideally be conducted with 1) an as high cooperativity as possible, as this strongly increases both the isolation ratio and the nonreciprocal bandwidth, and 2) fibre-resonator losses should dominate the intrinsic loss rate of the optical cavity ($\{\kappa_\mathrm{a}, \kappa_\mathrm{b}\} \gg \kappa_0$) to facilitate efficient light conversion between both waveguides.

6.3 Experimental setup

In our experiment we aim for an add-drop scheme that consists of two tapered fibres that are both evanescently coupled to a single microtoroid resonator (fig. 6.4c). As the tapered fibres' waist diameters are about 1 micron near their thinnest parts, they are naturally well separated in the region close to the microtoroid. However, at the end-facets of the tapered regions the total fibre diameter equals approximately 125 µm, significantly larger than the diameter (≈40 µm) of typical microtoroids (fig. 6.4b) used in our experiment. To nonetheless allow both fibres to approach the toroid, we use the following procedure. First, we make a short tapered fibre that is glued onto an aluminium holder and placed into the setup (fig. 6.4a). Next, a second (longer) tapered fibre that is still clamped in its original holder, used for pulling the fibre, is also positioned in the setup. After placing this second fibre, two single-axis translation stages carrying two posts are placed on its holder. Subsequent gentle movement of the translation stages allows both posts to press the tapered fibre forwards, leading to small pole-induced bending of the fibre (fig. 6.4a). Optimization of the exact position of the poles with respect to the fibre is required to minimize losses ($\sim 5\%$) of the fibre to the poles. After verifying that it is possible to simultaneously couple both fibres to the toroid *without* experiencing a decrease in transmittance, we are all set for the optomechanical circulator experiment.

A detailed schematic describing optical and electronic network of this experiment is given in fig. 6.5a. It revolves around a high-Q microtoroid ($\omega_\mathrm{c}/2\pi = 197\,\mathrm{THz}$, $\kappa_0/2\pi = 8.34\,\mathrm{MHz}$, $\Omega_\mathrm{m}/2\pi = 50.11\,\mathrm{MHz}$, $\Gamma_\mathrm{m}/2\pi = 61.17\,\mathrm{kHz}$) and the two tapered fibres, which are all placed inside a vacuum chamber operated at approximately $3 \times 10^{-6}\,\mathrm{mbar}$. After placing the tapered fibres in the vacuum chamber, fibre-feedthroughs allow for the splicing of these fibres to the existing optical measurement network. We note that the intrinsic mechanical frequency and linewidth are retrieved from a fit to the power spectrum shown in fig. 6.6. This spectrum is obtained using a spectrum analyzer and is measured at low

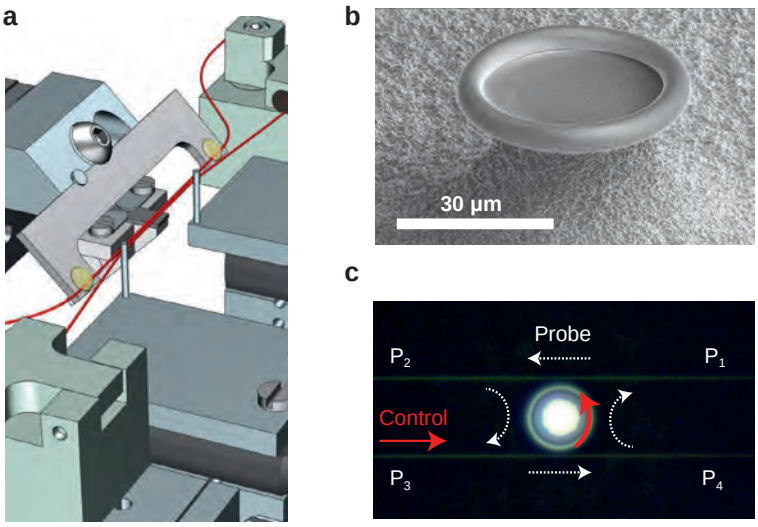

Figure 6.4: Coupling two fibres to a toroid. a, Drawing of the evanescent coupling setup. A short tapered fibre is glued onto an aluminium holder and placed in the setup. The second (longer) fibre is pressed forwards by two poles placed on small single-axis translation stages. The resulting bending of the fibre prevents the thicker end parts of both fibres to touch, and allows one to bring both fibres within close distance to the toroid. Drawing by Iliya Cerjak. **b,** Scanning Electron Microscope image of a silica microtoroid. **c,** Microscope image of two tapered fibres brought into close proximity of the studied microtoroid. The red solid arrow indicates the fixed launch direction of the control field. White dashed arrows indicate the propagation paths for a perfect 4-port circulator for a red-detuned control beam. P_j: ports of the circulator.

optical power to prevent optical spring effects.

The optical control and probe fields that are launched into the fibre system are derived from the same tunable external-cavity diode laser (New-Focus TLB-6728). Importantly, the electronic output at frequency Ω of the Vector Network Analyzer (VNA, R&S ZNB8) together with the Double-Parallel Mach-Zehnder Interferometer (DPMZI, Thorlabs LN86S-FC), operated in single-sideband carrier suppressed mode, allows for precise control over the detuning between optical control and probe fields. Depending on the voltages given to the DPMZI drive, we can either select the upper ($\omega_{\mathrm{control}} + \Omega$) or lower ($\omega_{\mathrm{control}} - \Omega$) frequency sideband (see appendix A).

Characterization of the full 4×4 scattering matrix of the optomechanical circulator requires 16 independent measurements. To minimize possible experimental drift during these subsequent measurements, our experimental scheme relies on four computer-controlled commercial switches; three optical switches (SWx, Thorlabs OSW12-1310E) and one radio frequency switch (RFSW, Mini-circuits USB-1SP4T-A18). Using the optical switches we choose in which of the

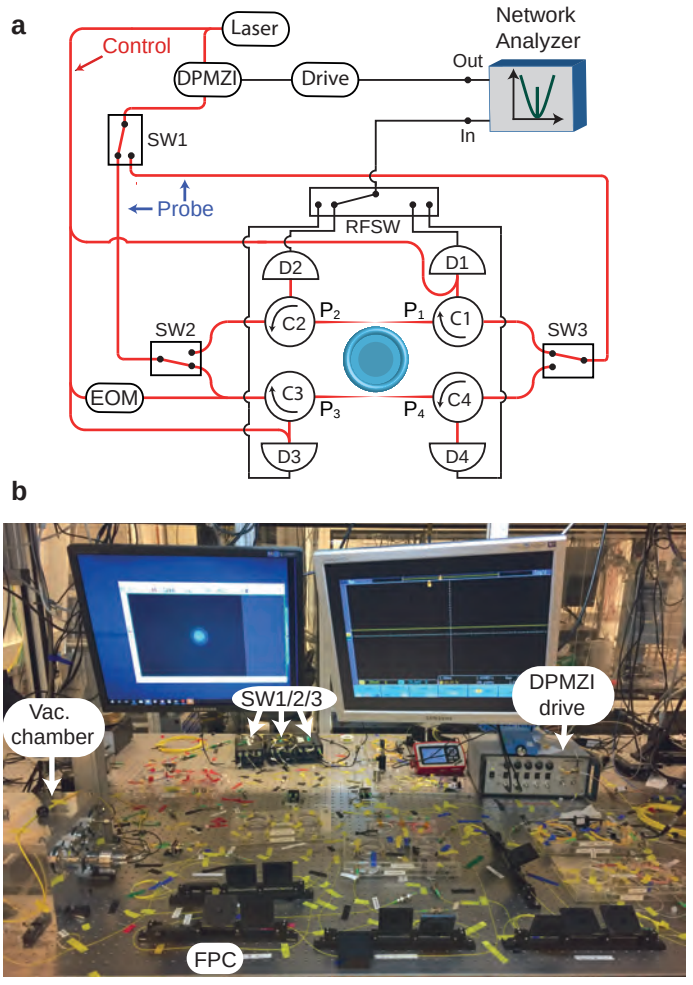

Figure 6.5: Experimental setup. **a,** Schematic of the experimental setup. Abbreviations; D: Detector, C: Circulator, SW: Optical Switch, RFSW: Radio Frequency Switch, EOM: Electro-Optic Modulator, DPMZI: Dual-Parallel Mach-Zehnder Interferometer. Not shown are the fibre polarization controllers (FPCs) placed directly after the outputs of SW2, SW3 and the EOM. More details are given in the main text. **b,** Photo of the optical table hosting the experiment. The left computer screen shows a live camera image of a microtoroid placed in the setup.

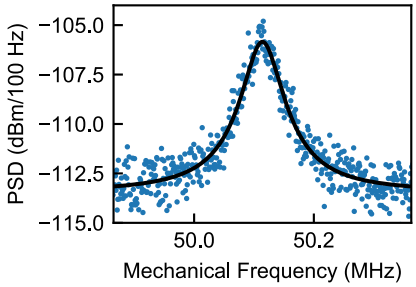

Figure 6.6: Characterizing the mechanical mode. Power spectral density (PSD) of the radial breathing mode in this study. The black line is a fit using a Lorentzian lineshape, allowing the retrieval of the intrinsic mechanical resonance frequency and linewidth.

four input ports (P_j) we launch our probe field. With four fibre polarization controllers (FPCs) placed directly after optical switches 2 and 3 we ensure that the polarization of the incoming probe fields is matched to that of the cavity mode. The polarization of the control field is separately regulated with a fifth FPC placed directly after the Electro-Optic Modulator (EOM). For clarity these FPCs are not drawn in fig. 6.5a. They are, however, visible in the foreground of fig. 6.5b. The EOM is used in a modified Pound-Drever-Hall locking scheme [12], the details of which are discussed in section 5.3. Crucial for understanding the experiment is the notion that the control field is *always* present and launched into port 3 (fig. 6.4c and fig. 6.5a), independent of the propagation direction of the probe field or measured s-parameter. As predicted by our theory, this single control field allows us to break reciprocity in all four transmission channels.

In our experiment, the typical probe powers ($< 10\,\mathrm{nW}$) are much smaller than the power in the control beam ($\approx 60\,\mu\mathrm{W}$), such that direct detection of the probe transmissivities is impossible. We instead employ a heterodyne detection scheme using the VNA. This scheme effectively measures a signal that is proportional to the beat of the control and probe fields. Due to the launch direction of the control field (via port 3) and symmetry in the system, the required control field is naturally available at detectors D2 and D4. To facilitate heterodyne detection at detectors D1 and D3, part of the control beam is split off and subsequently recombined with the transmitted probe field prior to detection.

6.3.1 Calibration and fitting

When characterizing the properties of the optomechanical circulator under test, one would like to isolate the device performance from losses experienced in the auxiliary fibre network. Ideally, this would be achieved by directly measuring

the fields just before – and slightly after – the optomechanical resonator. In practice, unfortunately, light propagates through lossy tapered fibres, circulators and splitters to finally end up at a non-ideal detector. In the previous chapter, with only one fibre coupled to the microtoroid, all aforementioned losses and the contribution of the control beam are divided out by virtue of a calibration measurement that is obtained by slightly detuning the optical probe frequency from the cavity frequency. Although this is a viable procedure for the direct channels, *i.e.,* when measuring s_{12}, s_{21}, s_{34} or s_{43}, this does not provide a satisfactory solution for the calibration of S-matrix elements associated with device reflection (*e.g.,* s_{11}), cross-coupling (*e.g.*, s_{13}) and add-drop functionality (*e.g.*, s_{14}). After all, one is only able to measure these s-parameters when operating on resonance with the cavity.

To provide calibrated and reliable S-matrix elements, the following experimental protocol is followed: First, careful characterization of all (lossy) elements between the microtoroid and detectors is performed. As may be expected, this includes all detector responses and losses associated with the circulators and tapered fibres. Next, both fibres are gently moved towards the microtoroid until the desired coupling strength is obtained. This includes optimization of all four FPCs. Note that the latter step involves continuous spectroscopy over a frequency region around ω_c, and is performed at elevated probe power levels ($\sim$1 µW) to allow direct measurements of all detector output voltages on an oscilloscope. These voltages are obtained by splitting the detector output lines (omitted in fig. 6.5) just before the RFSW. For the direct channels it is then possible to use the measured off-resonance voltages to normalize the on-resonance cavity response. Analogous to the procedure in the previous chapter, this directly yields the on-resonance transmission. Moreover, considering for example port 1$\rightarrow$ port 2, the non-resonant voltage on D2, together with the response of the detector and losses of the circulator and tapered fibre, allows to calculate back the actual power P_1^{in} that entered via port 1. Using the on-resonance voltages that are recorded by detectors D1/D3/D4 (obtained via fitting a Lorentzian lineshape) and compensating with the appropriate losses we can then 1) determine the power exiting ports 1/2/4 and 2) calculate the reflection/cross-coupling/drop efficiencies. This procedure is repeated before and after the measurement to detect possible drifts. In addition, it should be reiterated after changing any of the fibre-toroid distances or modifying the polarization of one of the four incoming probe beams. In our two-colour experiment, raw VNA response data is converted into a y-axis displaying transmittance with the help of these previously determined transmittance efficiencies. This post-processing involves the removal of a small portion of raw VNA spectroscopic data surrounding the mechanical peak. Next, Lorentzian lineshapes are fitted to this cropped (and squared) VNA data, of which the fitted maxima are used to normalize the reflection, cross-coupling and add-drop data points. For the direct channels, normalization is performed with respect to the minimum of the fitted line. All curves are then multiplied

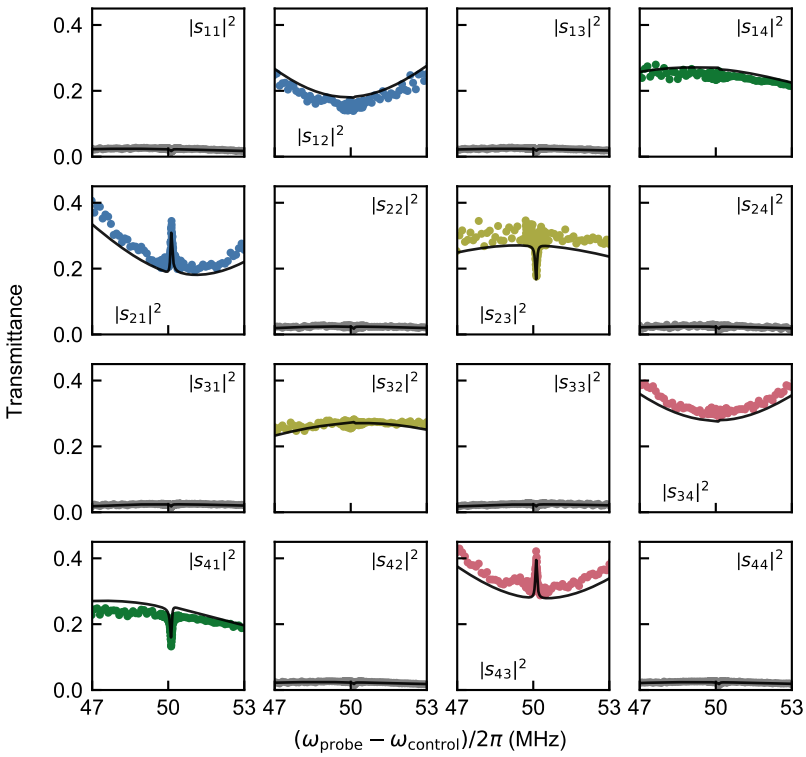

Figure 6.7: Demonstration of circulation. Visual inspection of the 4×4 $|S|^2$ matrix clearly shows that our optomechanical resonator operates as a circulator; Lorentz reciprocity is broken in all four circulator channels when the probe frequency is offset to the control frequency by approximately 50 MHz (Ω_{m}). To ease the readability of the figure, corresponding matrix pairs are coloured similarly (blue: $\{|s_{12}|^2, |s_{21}|^2\}$, yellow: $\{|s_{23}|^2, |s_{32}|^2\}$, red: $\{|s_{34}|^2, |s_{43}|^2\}$, green: $\{|s_{41}|^2, |s_{14}|^2\}$). Matrix elements associated with cross-coupling and reflection are coloured in grey. The black line resembles a global fit to the experimental data, fitting all 16 s-parameters simultaneously. To capture small experimental drifts, only the detunings $\bar{\Delta}_{1,2}$ are allowed to vary among different parameters. From this fit, we obtain $\mathcal{C}_{1,2} = 0.15$ and a frequency splitting between the optical modes of 2.8 MHz. This splitting is required to explain the resonant reflection and cross-coupling.

with their respective transmittance efficiencies to yield experimental data as, for example, displayed in fig. 6.7. The grey lines shown in this figure are the result of a global fit, that fits our theoretical model to all 16 parameters simultaneously. During fitting, $\Omega_\mathrm{m}, \Gamma_\mathrm{m}$ and κ_0 are held fixed, as they are obtained from independent spectroscopic measurements of thermal noise and cavity transmission. To account for experimental drift during data acquisition, the only parameters that are allowed to vary between the different s-parameters are the control detunings $\bar{\Delta}_{1,2}$. Note that the presence of frequency splitting between the two optical modes is reflected in $\bar{\Delta}_1 \neq \bar{\Delta}_2$.

6.4 Measurement results

6.4.1 Red-detuned control frequency

Figure 6.7 shows the resulting transmittance data for all 16 elements in the scattering matrix, obtained as a function of probe-control detuning, with the control beam fixed to the red motional sideband ($\bar{\Delta}_{1,2} \approx -\Omega_\mathrm{m}$) and incident from port 3. Equal colouring is applied for opposite scattering elements (*i.e.* $s_{12} \leftrightarrow s_{21}$), and reflections and cross-coupling are coloured in grey. Visual inspection of the results reveals that our device operates as a true circulator; the $|S|^2$ matrix is asymmetric at probe frequencies offset by approximately 50 MHz (Ω_m) from the control frequency. For example, the direct channel $|s_{21}|^2$ exhibits a narrow mechanically-induced OMIT peak that is absent in $|s_{12}|^2$. This is a direct consequence of the optomechanical interaction breaking Lorentz reciprocity. Moreover, also the cavity-mediated fibre-to-fibre (add-drop) transmittance is nonreciprocal. As an example, $|s_{41}|^2$ experiences a reduced mechanically-induced transmittance at optimal detuning, whereas $|s_{14}|^2$ displays a transmittance profile that lacks this feature. Instead, $|s_{14}|^2$ is only governed by the optical susceptibilities of both optical modes. We can thus conclude that in both the direct channels and the add-drop channels Lorentz-reciprocity is broken. It is noteworthy that our experimental data is well-described by our theoretical model. This can be seen from the black lines in fig. 6.7, which are the result of the global fit to all 16 s-parameters using the theoretical model outlined in section 6.2.

Before going into detail about the exact numbers that characterize the circulator, we note that the cross-coupling and reflectance in this device are negligible. For a large part this results from the use of two (nearly) degenerate even and odd modes. As a result, an incoming probe beam drives these modes in (near-perfect) quadrature, resulting in an effective intracavity field (at the probe frequency) closely resembling a single propagating whispering-gallery-mode (WGM) with the same handedness as the incoming probe field. Accordingly, the lack of field in the oppositely travelling WGM mode strongly suppresses unwanted resonant reflections and cross-coupling over the full band-

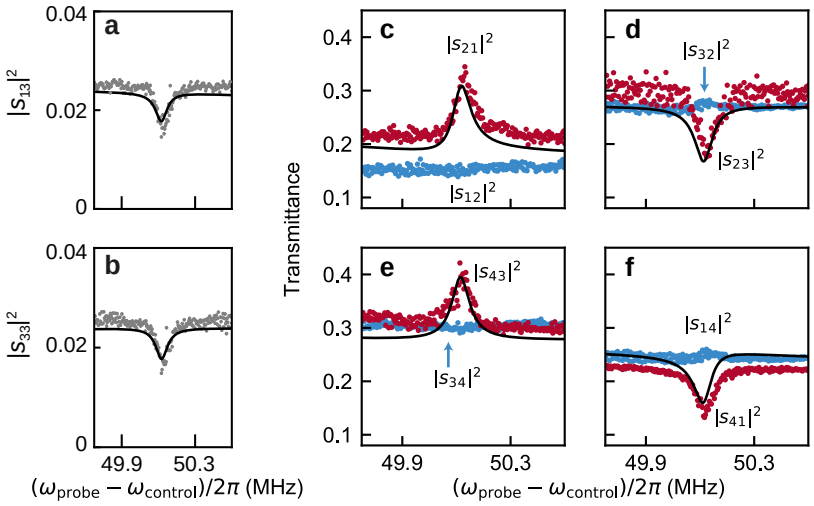

Figure 6.8: Comparison of scattering channels. **a**/**b**, The optomechanical interaction suppresses both unwanted cross-coupling ($|s_{13}|^2$, **a**) and reflectance ($|s_{33}|^2$, **b**), essentially turning a non-ideal add-drop filter into a more perfect device. We stress that the optomechanically induced suppression appears in all reflection and cross-coupling channels. **c-f**, For a probe-control detuning equal to Ω_{m}, all four S-matrix pairs show nonreciprocal transmittance over a bandwidth given by the effective mechanical linewidth $\Gamma_{\text{m}}(\mathcal{C}+1)$. The off-resonant background mismatch, which is especially prominent in **c** is most likely the result of calibration errors. The minimum isolation that is obtained for all four channels, for example calculated as $|s_{43}|^2/|s_{34}|^2$, is approximately 1.5 dB. The black lines in all panels are the result of the global fit performed on the dataset shown in fig. 6.7.

width of the optical cavity modes. Nevertheless, small reflections on the order of 2% do appear. These indicate that a small fraction of the total intracavity field propagate opposite to the incoming probe field, a direct consequence of mode-splitting in the microcavity. This frequency splitting is retrieved from the global fit to our data and is approximately 2.8 MHz. At first sight, this splitting seems to deteriorate the properties of the optomechanical circulator. Surprisingly, however, the optomechanical interaction between control and probe beam counteracts these non-idealities near the nonreciprocal frequency band (fig. 6.8a/b) for *all* s-parameters involving reflections and cross-couplings. For higher cooperativities these effects are further suppressed, resulting in ideal (zero) S-matrix elements for these channels.

To quantify the isolation in each circulator channel, *e.g.* $1 \leftrightarrow 2$ and $2 \leftrightarrow 3$, we directly compare the corresponding matrix pairs in fig. 6.8. This figure shows a zoom of the data in fig. 6.7, and shows the critical dependence on the optomechanical interaction that 1) creates an induced transparency window, and 2) carves out a dip in the add-drop transmittance spectrum, leading to a

noncreciprocal add-drop response of the system. The performance of the device is characterized by dividing the transmittance in opposite paths. For the red-detuned scenario, this gives isolation ratios of around 1.5 dB, with < 6 dB insertion loss over all channels. These numbers are mainly limited by the cooperativity that we can achieve, and consequently how high(low) the induced transparency peak is in the direct(add-drop) channel. Moreover, mechanical instabilities in the setup prevent us from strongly overcoupling the tapered fibres. This deteriorates the fibre-to-fibre transmission that we can achieve, as light is lost via intrinsic optical losses (κ_0), increasing the insertion losses in the add-drop channels. In addition, the sub-ideal fibre coupling also means that we can not fully suppress unwanted transmission in the direct channels by 'critical coupling' both fibres to each other, which further reduces the isolation contrast.

6.4.2 Blue-detuned control frequency

In our experiment with ω_{control} tuned to the red motional sideband, we are limited by the control power that we can use due to heating of the silica microtoroid, shifting the cavity resonance towards ω_{control} and destabilizing the system. To overcome this limitation and explore higher control powers, we perform experiments with a blue-detuned control frequency. The results are presented in fig. 6.9. In fig. 6.9a we plot the transmittance for opposite matrix pairs for incident control powers of 216 µW. Here, the coloured data points are associated with scattering matrix entries that we want to be high (signalling high transmittance). The opposite paths (which ideally are 0) are shown in grey. One should realize that the experiment now relies on optomechanically induced absorption (OMIA), instead of induced transparency, to break reciprocity. This means that the working direction of the circulator is opposite to that for the red-detuned case. As such, $|s_{21}|^2$ exhibits a peak in fig. 6.8c, while experiencing a dip in fig. 6.9a, for example. Another difference between both datasets is the stronger presence of two mechanically mediated peaks in *each* panel in fig. 6.9a. For example, both $|s_{21}|^2$ and $|s_{12}|^2$ couple to the mechanical mode, displaying an induced transparency and absorption signal, respectively. This is a consequence of the frequency splitting between both optical modes that was previously discussed in section 5.2. Although this splitting is also present in the red-detuned scenario, it is the higher control power (higher $\mathcal{C}$) that reveals this behaviour.

To visualize the total device performance, we plot the on-resonance transmittance for all 16 s-parameters in fig. 6.9b on a real transmittance axis. Observation of this plot directly shows an asymmetry in the 4×4 scattering matrix. High transmittances are obtained for $|s_{12}|^2$, $|s_{23}|^2$, $|s_{34}|^2$ and $|s_{41}|^2$, whereas their opposite elements (coloured similarly), as well as reflectance and cross-couplings (coloured in grey), are close to 0. From this data we calculate the isolation and insertion loss for each channel (fig. 6.9c/d). It is

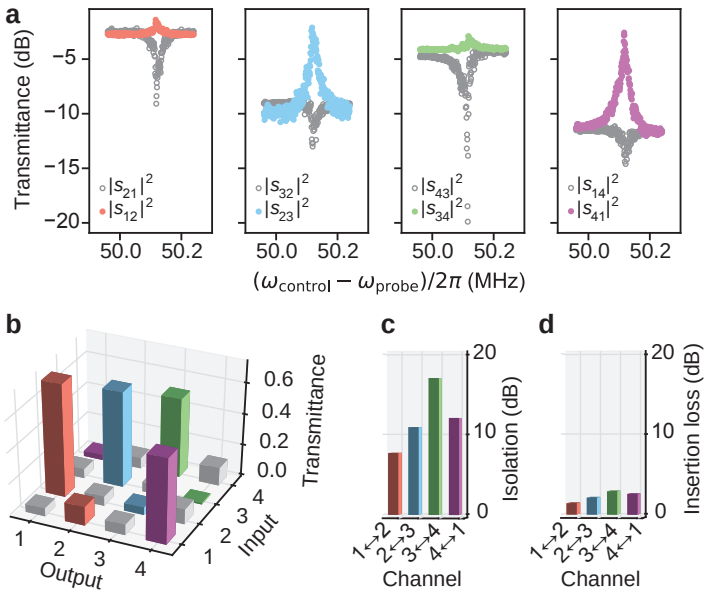

Figure 6.9: Circulation with a blue-detuned control frequency. **a**, Probe-transmittance (logarithmic scale) for the opposite matrix pairs that are used to calculate the per channel isolation. Coloured filled data points indicated wanted transmission channels, while open grey points are associated with (ideally) blocked S-matrix elements. **b**, 3-D representation of the on resonance ($\omega = -\Omega_m$) transmittance (real-scale) for all 16 elements of the S-matrix, which shows a clear asymmetry and thus proves the breaking of Lorentz reciprocity in the system. **c**/**d**, Per channel isolation (**c**) and insertion losses (**d**). The isolation is obtained by dividing the transmittances of corresponding matrix pairs, while the insertion loss in simply calculated as (1-Transmittance) for $\omega = -\Omega_m$.

clear that the enhanced control power clearly increases the attainable isolation (fig. 6.9c), and reduces the insertion losses (fig. 6.9d), thus improving the circulator performance with respect to the red-detuned scenario discussed in section 6.4.1.

6.4.3 Discussion

Considering this enhancement of isolation and reduction of insertion loss, at first sight, a blue-detuned control field seems to have only benefits. Several important drawbacks do exist, however. First, in contrast to the red-detuned case, reflections and cross-coupling are amplified, instead of suppressed. The fact that these unwanted signals are low in fig. 6.9b is primarily the result of low initial reflections, *i.e.* the reflections solely induced by the optical modes. As such, control-beam-enhanced reflections and cross-coupling remain low in the parameter regime considered here. For high powers and higher intrinsic optical

frequency splitting, however, enhanced reflection and cross-coupling severely hinder the device performance. Secondly, a blue-detuned control frequency provides gain to the optomechanical system. Whereas a red-detuned control beam *damps* the mechanical resonator, a blue-detuned control field *drives* the mechanical resonator. This has as a direct consequence that the noncreciprocal bandwidth, which is widened for a red-detuned control, narrows for a blue-detuned control field. In the blue-detuned case, the effective nonreciprocal bandwidth Γ_{eff} is thus given by $\Gamma_{\text{eff}} = \Gamma_{\text{m}}(1 - \mathcal{C})$. As the cooperativity $\mathcal{C}$ also determines the observed gain, this presents us with a form of the well-known and undesirable gain-bandwidth trade off. Lastly, we note that an ideal device adds as little noise (photons) as possible. Considering that any system using gain represents an amplifier, and thus adds a certain minimum of noise [13], any sensitive application would preferably not use a blue-detuned control field, but instead use the red-detuned scenario. Note, however, that even in the latter scenario one has to deal with thermal fluctuations that enter via the mechanical bath and generate noise photons. To prevent work around this thermal effect and achieve ideal circulatory behaviour, it is required to cool the optomechanical system to the ground state [14, 15].

6.5 Conclusion

In this chapter we demonstrated a working 4-port optomechanical circulator, of which the operating principle is well-described by extension of the theoretical formalism developed in this thesis on optomechanically induced nonreciprocity. Measurements on all 16 s-parameters showed that we obtained an asymmetric scattering (transmittance) matrix with isolation in all four channels. We stress the beneficial optomechanical side-effect, when operating on the red motional sideband, that leads to suppression of stray reflection and cross-coupling. This interaction improves non-ideal add-drop filters, significantly easing strict fabrication conditions that are otherwise imposed on the system. Moreover, using a the blue-detuned control frequency we obtained $\sim$10 dB of isolation over all four channels, at negligible insertion loss and with low reflections. Primarily from an academic point of view, it would be is interesting to see if the system and theory studied here can be generalized to an N port circulator. From a practical perspective, this would be a low footprint directional roundabout that could be used in signal processing, complementing frequently used add-drop filters. On a final note, we emphasize that the theory and experimental results presented in this chapter are not reserved for optomechanical ring resonators as such, but could also be implemented in optomechanical crystals [10] or LC-circuits [5, 9, 11].

References

[1] A. Metelmann, and A. A. Clerk, *Nonreciprocal photon transmission and amplification via reservoir engineering*, Phys. Rev. X **5**, 021025 (2015).

[2] M.-A. Miri, F. Ruesink, E. Verhagen, and A. Alù, *Optical nonreciprocity based on optomechanical coupling*, Phys. Rev. Appl. **7**, 064014 (2017).

[3] M. Scheucher, A. Hilico, E. Will, J. Volz, and A. Rauschenbeutel, *Quantum optical circulator controlled by a single chirally coupled atom*, Science **354**, 1577 (2016).

[4] M. Aspelmeyer, T. J. Kippenberg, and F. Marquardt, *Cavity optomechanics*, Rev. Mod. Phys. **86**, 1391 (2014).

[5] S. Barzanjeh, et al., *Mechanical on-chip microwave circulator*, arXiv 1706.00376 (2017).

[6] H. A. Haus, *Waves and fields in optoelectronics* (Prentice-Hall, 1984).

[7] W. Suh, Z. Wang, and S. Fan, *Temporal coupled-mode theory and the presence of non-orthogonal modes in lossless multimode cavities*, IEEE J. Quantum Electron. **40**, 1511 (2004).

[8] C. Manolatou, et al., *Coupling of modes analysis of resonant channel add-drop filters*, IEEE J. Quantum Electron. **35**, 1322 (1999).

[9] N. R. Bernier, et al., *Nonreciprocal reconfigurable microwave optomechanical circuit*, Nat. Commun. **8**, 604 (2017).

[10] K. Fang, et al., *Generalized non-reciprocity in an optomechanical circuit via synthetic magnetism and reservoir engineering*, Nat. Phys. **13**, 465 (2017).

[11] G. A. Peterson, et al., *Demonstration of efficient nonreciprocity in a microwave optomechanical circuit*, Phys. Rev. X **7**, 031001 (2017).

[12] E. D. Black, *An introduction to Pound–Drever–Hall laser frequency stabilization*, Am. J. Phys. **69**, 79 (2001).

[13] A. A. Clerk, M. H. Devoret, S. M. Girvin, F. Marquardt, and R. J. Schoelkopf, *Introduction to quantum noise, measurement, and amplification*, Rev. Mod. Phys. **82**, 1155 (2010).

[14] J. D. Teufel, et al., *Sideband cooling of micromechanical motion to the quantum ground state.*, Nature **475**, 359 (2011).

[15] J. Chan, et al., *Laser cooling of a nanomechanical oscillator into its quantum ground state*, Nature **478**, 89 (2011).

Appendix A

Double-Parallel Mach-Zehnder Interferometer

In the experiments performed in chapters 5 and 6, we use an optical probe frequency ω_{probe} that is slightly detuned from the control frequency ω_{control} by a supplied RF frequency Ω. To achieve this, we employ a commercial (Thorlabs LN86S-FC) Double-Parallel Mach-Zehnder Interferometer (DPMZI) that is operated in single-sideband carrier-suppressed (SSB-CS) mode. A simple scheme is shown in fig. A.1. The supplied RF frequency is split in two lines, that experience approximately $\pi/2$ degree phase shift among each other (3 dB hybrid coupler (HC)), and phase-modulates two LiNb crystals to generate sidebands spaced at Ω. DC voltages applied to the same crystals ensure that the remaining carrier field (oscillating at ω_{control}) experiences a π phase shift in arm 1a(2a), such that it destructively interferes with the unaltered path 1b(2b). Note that the remaining sidebands in arms 1a and 2a oscillate $\pi/2$ out of phase due to the phase difference in supplied RF frequency. As a result, a

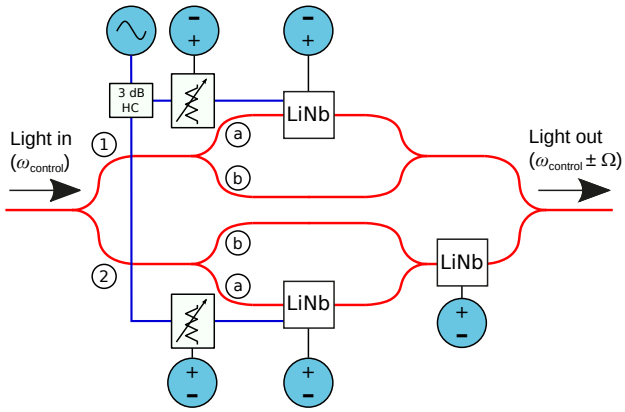

Figure A.1: Dual-Parallel Mach-Zehnder Interferometer. 3 dB HC: A 3 dB hybrid coupler that divides the incoming RF frequency and gives one of the outputs a $\pi/2$ phase shift with respect to the other. LiNb: Lithium Niobate crystals that are used to bias the optical field.

voltage bias on the third LiNb placed in arm 2, imprinting a $\pm\pi/2$ phase shift, can preferentially select either the upper or lower frequency sideband, achieving SSB-CS operation. The variable voltage attenuators are present to correct for non-ideal power splitting in the 3 dB hybrid coupler. For user-friendly operation of this device, we constructed an integrated control box, displayed in fig. A.2, that allows manual control over all five bias-voltages controlling the attenuators and DC voltages sent to the LiNb crystals. In addition, we implemented BNC connections that facilitate external (remote) control. We note that the hybrid coupler generally has ideal properties over only a limited frequency range. To compensate for non-$\pi/2$ phase shifts at the preferred operating frequency, we added an external analogue phase shifter located outside the casing (fig. A.2).

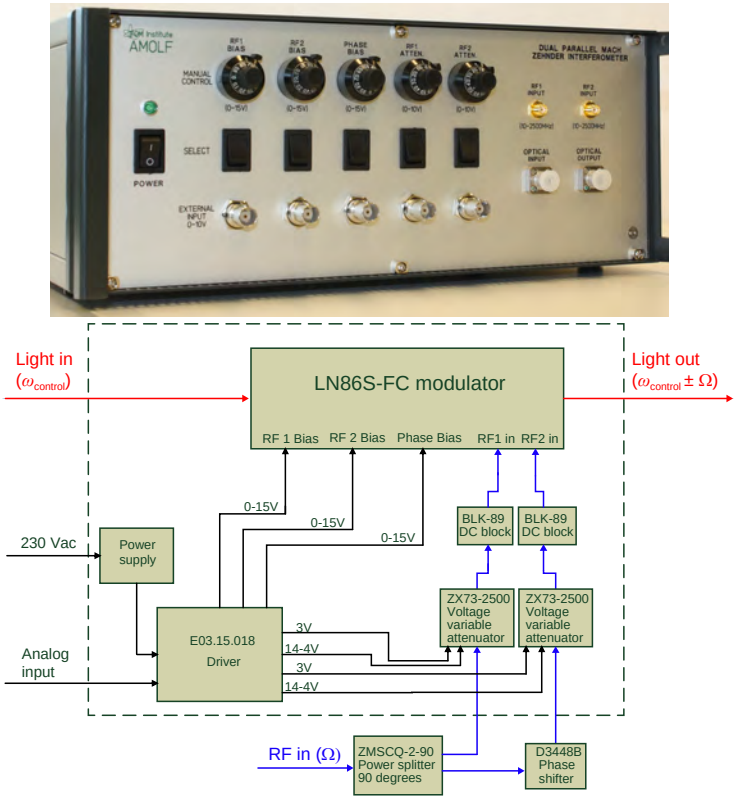

Figure A.2: Home-built casing and control scheme for the DPMZI. Top: Casing for the DPMZI and most of its control components. Bottom: The components enclosed by the dashed line are located inside the casing. The strongly frequency dependent hybrid-coupler, together with an analogue phase-shifter, are located outside the box for ease of access. Electronic circuit design and implementation: Ronald Buijs.

Appendix B

Connection between Coupled-Mode Theory and Cavity QED

In this appendix we investigate the connection between Coupled Mode Theory (CMT) — well-established in the optics and engineering literature [1] — and the quantum optics input/output formalism that is widely used in CQED [2–4], and also in many quantum optomechanics descriptions [5, 6]. In the following, we show how both formalisms are mathematically related, and how it is possible to transform fields and matrices to move from one picture to the other. This transformation involves a redefinition of the input (or output) fields.

In a CQED approach, the input/output relation is conventionally written as

$$\mathbf{s}^- = \tilde{\mathbf{s}}^+ + D\,\mathbf{a}, \tag{B.1}$$

where for a two mode system

$$\mathbf{s}^- = \begin{pmatrix} s_1^- \\ s_2^- \end{pmatrix} \quad \tilde{\mathbf{s}}^+ = \begin{pmatrix} \tilde{s}_1^+ \\ \tilde{s}_2^+ \end{pmatrix} \quad \text{and} \quad \mathbf{a} = \begin{pmatrix} a_1 \\ a_2 \end{pmatrix} \tag{B.2}$$

denote the output, input and intracavity field operators, respectively. This is for example detailed in [3], section 5.3. Note that in eq. (B.1) an explicit choice for the phase relation between input and output fields is made (sometimes taken with an extra minus sign [4], with similar result): In the absence of the cavity the output and input are related by the identity operator. Instead, in coupled-mode theory, a specific choice of this phase is avoided by introducing the C matrix operator such that

$$\mathbf{s}^- = C\,\mathbf{s}^+ + D\,\mathbf{a}, \tag{B.3}$$

which is equivalent to eq. (4.2). Note that the relation $\tilde{\mathbf{s}}^+ = C\mathbf{s}^+$ thus allows to transform outputs between the two formalisms. Next, we apply this transformation to eq. (4.1), which is reiterated here as

$$\frac{\mathrm{d}\mathbf{a}}{\mathrm{d}t} = \mathrm{i}\mathcal{M}\mathbf{a} + D^{\mathrm{T}}\,\mathbf{s}^+. \tag{B.4}$$

Inserting the relation $CD^* = -D$ (obtained from time-reversal symmetry in [1]) in eq. (B.4) we obtain

$$\begin{aligned}\frac{\mathrm{d}\mathbf{a}}{\mathrm{d}t} =& \mathrm{i}\mathcal{M}\,\mathbf{a} - (CD^*)^{\mathrm{T}}\,\mathbf{s}^+ \\ =& \mathrm{i}\mathcal{M}\,\mathbf{a} - D^\dagger C\,\mathbf{s}^+ \\ =& \mathrm{i}\mathcal{M}\,\mathbf{a} - D^\dagger\,\tilde{\mathbf{s}}^+. \end{aligned} \tag{B.5}$$

Here, eq. (B.5) is equivalent to the expression often used in CQED. We thus conclude that both formalisms differ only in the sense that CQED explicitly chooses a convention for the port description, fixing the phase of the incoming waves, while CMT does not.

The CMT formalism has the benefit that it allows to associate s_j^+ and s_j^- with incoming and outgoing waves in the same physical port. Considering the CQED approach (eq. (B.1)) and a simple waveguide, s_1^+ and s_1^- necessarily describe waves in different physical ports. To study nonreciprocity, it is more insightful to have these waves in the same port, as nonreciprocity is then always related to a difference of the off-diagonal elements of the scattering matrix, regardless of system choice.

References

[1] W. Suh, Z. Wang, and S. Fan, *Temporal coupled-mode theory and the presence of non-orthogonal modes in lossless multimode cavities*, IEEE J. Quantum Electron. **40**, 1511 (2004).

[2] M. J. Collett, and C. W. Gardiner, *Squeezing of intracavity and traveling-wave light fields produced in parametric amplification*, Phys. Rev. A **30**, 1386 (1984).

[3] C. Gardiner, and P. Zoller, *Quantum noise: a handbook of Markovian and non-Markovian quantum stochastic methods with applications to quantum optics* (Springer Science & Business Media, 2004), 3rd ed.

[4] D. F. Walls, and G. J. Milburn, *Quantum Optics* (Springer Berlin Heidelberg, Berlin, Heidelberg, 2008), 2nd ed.

[5] A. A. Clerk, M. H. Devoret, S. M. Girvin, F. Marquardt, and R. J. Schoelkopf, *Introduction to quantum noise, measurement, and amplification*, Rev. Mod. Phys. **82**, 1155 (2010).

[6] M. Aspelmeyer, T. J. Kippenberg, and F. Marquardt, *Cavity optomechanics*, Rev. Mod. Phys. **86**, 1391 (2014).

Epilogue

Summary

Manipulating light with ring resonators coupled to antennas and mechanical motion

The ability for humans to control light is frequently exploited in basic research environments and has enabled numerous light-based technologies. From a technological perspective, adding to conventional applications such as microscopy and lighting, light can be used for the transport of classical and (sensitive) quantum information. This is related to the low presence of (thermal) noise sources at optical frequencies, which allows faithful transfer of information even down to the single quantum level. However, to have light act as a useful information carrier it is also required to control the emission rate of photons by emitters and have the ability to manipulate and shape the flow of photons. Importantly, the wavelength at optical frequencies, together with a desire for small-footprint devices, sets the natural length scale for systems that can efficiently facilitate such functionality to nano- and microphotonic structures. In this thesis, we explore resonant micro- and nanophotonic structures that have the potential to enhance light-matter interactions and direct the flow of light. In particular, this work investigates the ability to tailor the optical response of a system that involves high quality-factor ring resonators. This is achieved by resonantly coupling the ring resonator's optical modes to either plasmonic nanoantennas, or to a *mechanical* mode of the structure itself. We show that in both of these coupled systems, controlled interactions between resonant modes of different nature can give an unusual optical response that can be used to manipulate the flow of light.

In the first part of this thesis we study the interaction between a ring resonator and plasmonic nanoantennas, and experimentally investigate the optical response of the resulting hybrid cavity-antenna system. We start in chapter 2 with investigations on a resonant mode of a microtoroid ring resonator and study how it changes when it is subject to a perturbation by an array of nanoantennas placed in its near field. In contrast to the widely accepted notion that the mode perturbation, in terms of a cavity frequency shift, can be directly related to the resonant polarizability of the introduced perturbation, we show that when radiation losses emerging from both the cavity and antenna can interfere, the resultant frequency shifts are pronouncedly altered. As discussed, this interference is a form of radiative mode coupling that results in cavity frequency shifts that are opposite to what would be expected based on the antenna polarizability alone. In addition to Finite Element Method simulations that confirm our results, we present an analytical model explaining the effect.

In chapter 3 the same antenna-cavity system is interrogated, but now by observing the linear response of the nanoantenna array. It was theoretically predicted before that the presence of a high-Q cavity could lead to a modification of the antenna polarizability and thus its linear response. This is

a result of interfering (scattering) fields at the position of the antenna array and is known as backaction. In this chapter we thus measure a modification of the polarizability of the array due to cavity-mediated backaction. In our experiment we isolate the backaction effect on the antennas using a carefully designed setup that allows for both real-space and Fourier-space filtering. Using the diffractive properties of an array, we show that it is possible to control the backaction strength by modifying the incident wave vector. This changes the overlap between the radiation profile of the array and the high-Q cavity mode and thus allows for a tunable cavity-backaction on the array.

In the second part of this thesis we discuss and demonstrate how a multimode optomechanical system, where multiple optical modes are coupled to mechanical motion via radiation pressure, can be used to break Lorentz reciprocity for light. This is interesting from an information processing perspective, as platforms that allow the breaking of Lorentz reciprocity give access to nonreciprocal elements, such as isolators and circulators, which can be used to manipulate and shape the flow of light in integrated circuits. The discussion on nonreciprocal light transmission is started in chapter 4, with theoretical investigations on an optomechanical system that involves two optical modes coupled to a joint mechanical degree of freedom. A suitable laser drive biases the optomechanical couplings, resulting in nonreciprocal mode transfer in the system, and thus acts as an effective magnetic field for light. Two distinct implementations are discussed, which employ either the optical or mechanical bath to remove light in the unwanted propagation direction, with different implications on bandwidth and power of operation.

In chapter 5 we put the theory formulated in chapter 4 to test in an experimental system that revolves around an optomechanical toroidal ring resonator. Owing to its symmetry, this ring resonator supports two optical modes that are both coupled to a mechanical radial-breathing-mode. Using the nonreciprocal optical mode-conversion process explained in chapter 4 we achieve nonreciprocal amplitude and phase transmission. Both isolation (of approximately 10 dB) and unidirectional amplification are demonstrated. In addition, we present results that show the persistence of the nonreciprocal effect for nondegenerate optical modes.

Finally, in chapter 6 we employ the aforementioned nonreciprocal optomechanical interaction to demonstrate an on-chip four-port circulator, extending the geometry that is studied in chapter 5 with two extra input and output ports. This technically challenging system is realized by simultaneously coupling two tapered optical fibres to a single toroidal ring resonator. With a tailored measurement scheme we perform measurements on all 16 scattering parameters that describe the four-port circulator. We investigate two different schemes, with the control laser tuned to the red and blue motional sideband of the cavity mode, and obtain around 10 dB of isolation in all circulator channels at a minimum of insertion losses.

Samenvatting

Het manipuleren van licht met ringvormige trilholtes gekoppeld aan antennes en mechanische beweging

Vanwege verschillende unieke eigenschappen wordt licht veelvuldig gebruikt in zowel fundamenteel onderzoek als in praktische toepassingen. Vanuit technologisch perspectief, naast conventionele toepassing zoals het gebruik van licht in microscopen of simpelweg het verlichten van ruimtes, kan licht ook gebruikt worden voor het transport van informatie. Dit heeft te maken met de lage aanwezigheid van storingsbronnen (ruis) die de gegevensoverdracht kunnen beïnvloeden of verstoren. Met name voor kwantuminformatie die is gecodeerd in een enkel lichtdeeltje is dit minimaliseren van ruis van groot belang. Voordat licht echter in een praktische toepassing gebruikt kan worden dient er aan een aantal randvoorwaarden te worden voldaan: men moet 1) kunnen controleren wanneer er licht wordt uitgezonden en 2) waar het uitgezonden licht zich naartoe beweegt. Controle over licht wordt vaak bereikt door de materie (omgeving) waarin lichtbronnen zich bevinden op een bepaalde manier te structureren. Vanwege de golflengte van licht ($\approx$1 µm) zijn structuren die de eigenschappen van licht kunnen manipuleren typisch nanometers tot micrometers groot. In deze dissertatie onderzoeken we resonante micro- en nanofotonische structuren, structuren die sterk interacteren met licht, die gebruikt kunnen worden voor de manipulatie van licht. In het bijzonder onderzoeken we de mogelijkheid tot het controleren van de optische respons van systemen die bestaan uit ringvormige trilholtes (*ring resonatoren*) met hoge kwaliteitsfactor. Dit doen wij door de optische eigenmodi van de ring te koppelen aan ofwel gouden plasmon nanoantennes, of aan een *mechanische* resonantie van de ringstructuur zelf. In deze dissertatie laten we zien dat het controleren van de koppeling tussen de ring en antennes of beweging kan leiden tot een ongebruikelijke optische respons, die gebruikt kan worden voor het manipuleren van de propagatie(richting) van licht.

In het eerste deel van dit proefschrift bestuderen we de interactie tussen een trilholte en plasmon nanoantennes, en onderzoeken de optische respons van het hybride trilholte-antenne systeem. We beginnen in hoofdstuk 2 met het onderzoeken van een resonante eigenmodus van een microtoroïde, een donutvormige ring resonator van glas, en bekijken hoe deze eigenmodus verandert wanneer deze geperturbeerd wordt door een tweedimensionaal rooster van nanoantennes geplaatst in het nabije veld van de ring. In tegenstelling tot de wijdverbreide notie dat de perturbatie, in termen van de frequentieverschuiving van de optische resonantie, direct gerelateerd kan worden aan de resonante polariseerbaarheid van de geïntroduceerde perturbatie, laten wij zien dat wanneer radiatieverliezen vanuit de trilholte en antennes kunnen interfereren de uiteindelijke frequentieverschuiving sterk kan verschillen van de voorspelde waardes. Zoals we

bediscussiëren is dit interferentie-effect een vorm van stralingskoppeling die ervoor zorgt dat de uiteindelijke frequentieverandering tegengesteld is aan een verwachting die alleen gebaseerd op de polariseerbaarheid van de nanoantennes. Onze resultaten worden bevestigd door een eindige-elementenmethode berekening. Daarnaast presenteren we een analytisch model dat het effect verklaard.

In hoofdstuk 3 meten en bestuderen we de lineaire respons van het nanoantenne rooster in het bijzijn en in de afwezigheid van de trilholte. Het is voorspeld dat de aanwezigheid van zo'n hoge kwaliteitsfactor trilholte kan leiden tot een modificatie van de polariseerbaarheid van de antennes, en dus van de lineaire respons. Dit is het resultaat van interfererende velden (middels verstrooiing) op de positie van het antennerooster en staat bekend als *terugkoppeling*. In dit hoofdstuk meten we dus de verandering in polariseerbaarheid van het antennerooster door trilholte geïnduceerde terugkoppeling. We isoleren dit effect in ons experiment met behulp van een specifiek ontworpen optische opstelling die gebruikt maakt van filtering in zowel het reële vlak als het Fourier domein. Gebruikmakend van de diffractieve eigenschappen van het rooster laten we vervolgens zien dat het mogelijk is om de sterkte van de terugkoppeling te controleren via het veranderen van de inkomende golfvector van het gebruikte licht. Dit verandert de overlap tussen het stralingsprofiel van het antennerooster en dat van de trilholte, en daaraan gerelateerd dus ook de sterkte van het terugkoppelingseffect.

In het tweede gedeelte van dit proefschrift bekijken en demonstreren we hoe een optomechanisch systeem, waar meerdere optische eigenmodi gekoppeld zijn aan mechanische beweging via stralingsdruk, gebruikt kan worden om Lorentz reciprociteit voor licht te breken. Dit breken van reciprociteit is interessant vanuit een informatieverwerkingsperspectief, omdat systemen die Lorentz reciprociteit breken gebruikt kunnen worden om niet-reciproke elementen zoals isolatoren en circulatoren te bouwen. Zulke elementen (kunnen) worden gebruikt voor het manipuleren en regelen van de propagatierichting van licht in geïntegreerde circuits. De discussie aangaande niet-reciproke lichttransmissie wordt gestart in hoofdstuk 4 met een theoretische studie naar optomechanische systemen bestaande uit twee optische resonanties gekoppeld aan een gedeelde mechanische vibratie. Een geschikte laser breekt de symmetrie in het optomechanische systeem, resulterend in niet-reciproke lichtoverdracht in het systeem, wat gezien kan worden als een effectief magnetisch veld voor licht. Twee significant verschillende implementaties worden behandeld, waarbij ofwel het optische ofwel het mechanische reservoir wordt gebruikt om licht in de ongewenste propagatierichting in te dissiperen, die beide een verschillende bandbreedte hebben en ander eisen stellen aan de benodigde stralingsdruk.

In hoofdstuk 5 onderzoeken we de validiteit van de in hoofdstuk 4 ontwikkelde theorie in een experimenteel systeem dat draait om een optomechanische microtoroïde: een ringvormige trilholte. Vanwege de symmetrie in de structuur ondersteunt de ring twee optische resonanties die beide gekoppeld zijn aan dezelfde mechanische vibratie. Met behulp van de niet-reciproke optomechanisch-

geïnduceerde lichtoverdracht, uitgediept in hoofdstuk 4, demonstreren we niet-reciproke amplitude- en fasetransmissie. We bereiken zowel isolatie (van ongeveer 10 dB) als unidirectionele amplificatie van licht. Daarnaast presenteren we resultaten die laten zien dat het niet-reciproke effect behouden blijft voor niet-ontaarde optische resonanties, d.w.z. resonanties van verschillende energie.

Als laatste gebruiken we in hoofdstuk 6 de hiervoor genoemde niet-reciproke optomechanische interactie om een circulator met vier in- en uitgangen te maken. Om dit te bereiken bereiden we de geometrie die in hoofdstuk 5 is bestudeerd uit met twee extra in- en uitgangskanalen. Dit technisch ingewikkelde systeem is gerealiseerd door twee versmalde optische glasvezelkabels tegelijkertijd aan de microtoroïde te koppelen. Met een speciaal meetsysteem doen we metingen aan alle 16 elementen van de verstrooiingsmatrix die samen de circulator beschrijven. Het systeem is onderzocht in twee verschillende situaties: met een controle laser die frequentieverschoven is naar ofwel de rode danwel de blauwe mechanische zijband van de trilholte. Onder specifieke condities bereiken we ongeveer 10 dB aan isolatie in alle kanalen van de circulator, waarbij de signalen een minimum aan verlies ervaren.

List of publications

Related to this thesis

- F. Ruesink, H. M. Doeleman, R. Hendrikx, A. F. Koenderink, and E. Verhagen, *Perturbing open cavities: anomalous resonance frequency shifts in a hybrid cavity-nanoantenna system.*
  Phys. Rev. Lett. **115**, 203904 (2015) (**Chapter 2**)
- F. Ruesink*, H. M. Doeleman*, E. Verhagen, A. F. Koenderink, *Observing antenna depolarization due to cavity-induced backaction.*
  In preparation (**Chapter 3**)
- M.-A. Miri, F. Ruesink, E. Verhagen, and A. Alù, *Optical nonreciprocity based on optomechanical coupling.*
  Phys. Rev. Applied, **7**, 064014 (2017) (**Chapter 4**)
- F. Ruesink, M.-A. Miri, A. Alù, and E. Verhagen, *Nonreciprocity and magnetic-free isolation based on optomechanical interactions.*
  Nat. Commun. **7**, 13662 (2016) (**Chapter 4 & 5**)
- F. Ruesink*, J. P. Mathew*, M.-A. Miri, A. Alù, and E. Verhagen, *Optical circulation in a multimode optomechanical resonator.*
  Submitted, preprint at arXiv:1708.07792 (**Chapter 6**)

Other

- T. H. van der Loop*, F. Ruesink*, S. Amirjalayer, H. J. Sanders, W. J. Buma, and S. Woutersen, *Unraveling the mechanism of a reversible photoactivated molecular proton crane.*
  J. Phys. Chem. B **118**, 12965-12971 (2014)

* These authors contributed equally

Acknowledgements

After four years of research I can safely argue that good technical support, a stimulating environment and a capable promotor are key ingredients for the successful completion of a PhD. Luckily AMOLF provides these elements, and the results presented in this thesis would not have been possible without the contribution from – and interaction with – many of my colleagues.

As a member of the newly started 'Photonic Forces' group, I had the opportunity to learn essential scientific skills directly from my promotor. Ewold, I really appreciate the dedication and enthusiasm with which you teach and discuss practical and theoretical essentials. Nowadays I realize that it is a luxury to have an advisor with whom you can frequently discuss and share all sorts of problems that you face when doing research. Thank you for the inspiring discussions, taking the risk of hiring a chemist, and all the time and effort you put into my education.

My time at AMOLF started and ended with projects on hybrid cavity-antenna systems. In these projects I closely collaborated with Femius, Hugo and Ruud. Femius, thank you for acting as my second promotor, the critical reading of this manuscript and for transferring your enthusiasm about Green's functions. Hugo and Ruud, thank you for laying the groundwork of the tapered fibre setup that is used throughout this thesis. Hugo, we did some very nice experiments that needed plenty of time to digest and shared some very frustrating coding experiences. Luckily we are now finally starting to benefit from these efforts. Thank you for the nice and pleasant collaboration!

Rick, you started as the first PhD student in the group and just finished your thesis yourself. Thank you for all the work you put into the organization of a nice lab, writing shared python code and all your critical comments during group meetings. I am pretty sure that I will never use a rainbow colour scale ever again ;-).

For the second part of this thesis I worked together with Andrea and Ali: thank you for all your input on the nonreciprocity project. The Amsterdam-Austin video calls were a pleasure, and the discussions we had resulted in very nice collaborative work. It was a great experience to work together with such excellent theoreticians. John, thank you for joining the nonreciprocity team over the past year. It was nice to work with you in- and outside the lab. Surprisingly even the demolishing and fabrication of tapered fibres was more joyful with you around.

Although PhD research can be frustrating, there were very few days in which I did not like my job. This largely relates to the friendly colleagues I worked with. Big thanks to all current group members and former MSc students of the Photonic Forces group for the lunches, coffee breaks and intense (group meeting) discussions we shared over the past years. Juha, Giada, Lars, Randy and Robin, thank you for making the group and AMOLF a more lively place.

Nikhil, although we never worked on a shared project, as my office mate you have been an integral part of my AMOLF life. Thank you for all the shared frustrations and your support during the final weeks of writing. Due to your great eye for style I often misused you for feedback on my figures, thank you for all the comments you provided!

The experimental results would not have been possible without excellent support by the AMOLF technical staff. In particular Jan Bonne, thank you for all your practical help inside the lab. Ronald, thanks with your help in the design of the electronic control box controlling the DPMZI and any question I had regarding electronics. Luc, thank you for your help with developing 'phofo suite' and translating unreadable snippets of code. I would also like to thank all the members of the design department, Iliya in particular, and mechanical workshop for all their help in the design and construction of various elements in my setup. In addition, none of the experimental chapters would have existed without the use of the cleanroom. Big hugs to all of AMOLF's cleanroom staff, Hans, Dimitry, Bob, Andries and Johan for keeping things running smoothly and helping me out with the fabrication of toroids. Wiebe and Rutger, thank you for always providing quick ICT support!

Membership of the Photonic Forces group provides access to a weekly journal club, co-organised with the Resonant Nanophotonics group. It was great to discuss papers and decide on what is – and what is not – a proper way of writing, presenting data or drawing conclusions. In addition I would like to acknowledge all group leaders of the participating groups of the nanophotonics colloquium for maintaining a stimulating environment to discuss scientific results. Furthermore, I benefited from discussion and nice chats with (amongst others) Kobus, Clara, Felipe, Cocoa, Kevin, Christiaan, Annemarie, Isabelle, Ruslan, Sander, Sebastian, Eric, Parisa, Rutger, Mark, Ruben, Jorik, Benjamin, Nick, Boris, Dolfine, Lorenzo and Filippo. All of you made AMOLF a much nicer and more productive place to work.

Graag bedank ik natuurlijk ook mijn vrienden voor alle momenten van ontspanning die de afgelopen vier jaar een stuk aangenamer maakten. Arthur en Ids, hartstikke leuk dat jullie m'n paranimfen willen zijn!

Raïsa, bedankt voor alle liefde, steun en begrip tijdens de eindfase van dit proces, en nogmaals excuus voor alle gemiste avonden en weekenden van de afgelopen tijd...

Als laatste wil ik graag mijn ouders bedanken voor de belangrijke en vaak onzichtbare bijdrage die zij hebben geleverd: jullie zijn onmisbaar geweest bij het bereiken van dit resultaat!

Author information

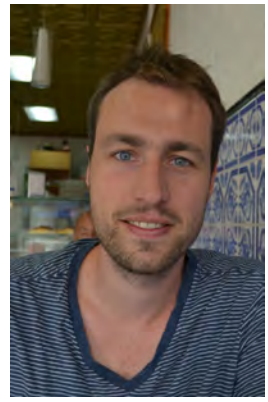

Freek Ruesink was born on the 27th of June (1988) in Amsterdam. In 2010 he obtained a BSc degree in Liberal Arts and Sciences (major in Chemistry) from the University of Amsterdam (UvA). He finished this degree with a project on hyperpolarized signals in nuclear magnetic resonance spectra, typically used for the characterization of catalytic hydrogenation reactions, performed at the University of York (UK). Next, he continued with a Master's degree in Physical Chemistry and graduated in 2013 from the UvA with a research project on ultrafast time-resolved infrared spectroscopy, performed in the group of professor Sander Woutersen. In this project he studied the reaction dynamics of intramolecular proton transfer in an UV-activated photo-acid. Freek, a percussion player himself, took a one-year sabbatical during his Master's to serve as a full-time board member of the Dutch National Student Orchestra. After finishing his Master's, he started as a PhD researcher in the newly started Photonic Forces research group at AMOLF under the supervision of professor Ewold Verhagen. The results of his PhD work are presented in this thesis.